

University of Nevada, Reno

**Design and Characterization of Scanning Probe Microscopy Platform
with Active Electro-Thermal Microcantilever
for Multifunctional Applications**

A thesis submitted in partial fulfillment of the
requirements for the degree of Master of Science in
Mechanical Engineering

by

Robert O. Riddle

Dr. Kam K. Leang/Thesis Advisor

August 2011



THE GRADUATE SCHOOL

We recommend that the thesis
prepared under our supervision by

ROBERT OREN RIDDLE

entitled

**Design and Characterization of Scanning Probe Microscopy Platform with Active
Electro-Thermal Microcantilever for Multifunctional Applications**

be accepted in partial fulfillment of the
requirements for the degree of

MASTER OF SCIENCE

Kam K. Leang, Ph. D., Advisor

Emil J. Geiger, Ph. D., Committee Member

Xiaoshan Zhu, Ph. D., Graduate School Representative

Marsha H. Read, Ph. D., Dean, Graduate School

August, 2011

Abstract

The goal of this thesis is create a scanning probe microscopy (SPM) platform for multifunctional probe-based applications, such as interrogation, manipulation, and fabrication of objects and matter at the micro to nano-scale. The SPM platform uses a newly designed and fabricated electro-thermo-mechanical (ETM) cantilever with a microgripper at its distal end designed for automated pickup and release of tool tips. This unique platform will help address the critical issues of throughput, repeatability, scalability, and limited functionality of probe-based applications including multi-process nanofabrication. The design, fabrication, and characterization of the custom-made atomic force microscopy (AFM) system, a type of SPM, and the ETM microgripper for multifunctional probe-based applications are presented. The finite element method is used to design the first two vibration modes of the ETM microgripper to align with traditional AFM cantilevers. An electro-thermo-mechanical model is used to predict the response of the ETM microgripper. The custom-made AFM system and ETM microgripper are characterized, where experimental results demonstrate the imaging capabilities of the AFM system and the microgripper's ability for controlled grasping of micro-sized objects. Specifically, the AFM system resonances at 768 Hz, 535 Hz, and 35 kHz in the x , y , and z axis, respectively. The microgripper can open $6.4 \mu\text{m}$ with 10 volts input, and the measured first mechanical resonance is 36.8 kHz. Performance and design challenges are also discussed. The results and outcomes of this thesis lay the foundation for future work in multifunctional probe-based applications which include handheld replicators for nano rapid prototyping of nanoelectronics and NEMS, printing and nanomachining of unique hybrid organic and inorganic material, 3-D nanofabrication and assembly, and complete desktop nanofactories.

Acknowledgments

First and foremost, I would like to thank my advisor, Kam, for his guidance, patience, and support throughout this entire process. Also, I thank Dr. Geiger and Dr. Zhu for their support while serving on my thesis committee.

I gratefully acknowledge the research support of the National Science Foundation NanoManufacturing Program, Grant CMMI #0910570. I am also want to acknowledge the teaching experiences I gained from the University of Nevada, Reno.

I thank Bijoyraj Sahu and Dr. Curtis Taylor at the University of Florida for their assistance on this collaborative project.

I also want to thank my lab mates Yingfeng Shan, Brian Kenton, Maxwell Fleming, and Joel Hubbard for their insightful discussions and technical assistance.

I thank Al Dey at Natel Engineering Company Inc. in Carson City, NV for his assistance in the wire bonding process and Dr. Gunnar Newquist for his assistance in wire etching.

Finally, I would like to thank my family for their unconditional love and support.

Dedication

In memory of my father, Robert Lee Riddle.

August 1, 1943 – November 28, 2006

Contents

1	Thesis Goal, Objectives, and Contribution	1
1.1	Overview	4
1.2	Motivation and Contribution	5
1.3	Methodology	7
1.3.1	Why Electro-Thermal-Mechanical (ETM) Actuation?	7
1.3.2	ETM Multifunctional Probe Design	8
1.3.3	Multifunctional Probe Characterization	9
1.3.4	Custom AFM Design for Multifunctional Probe	10
1.3.5	AFM Platform Testing	11
1.4	Summary of Completed Work	11
1.5	Organization	13
2	Background	14
2.1	Scanning Probe Microscopy	14
2.1.1	Scanning Tunneling Microscopy	15
2.1.2	Atomic Force Microscopy	16
2.1.3	Nanofabrication	29
2.2	ETM Actuators	31
2.3	Summary	34

3	AFM Design, Fabrication, and Characterization	36
3.1	Mechanical Design	39
3.1.1	AFM Approach Mechanism	41
3.1.2	AFM Scanner Mechanism	44
3.1.3	AFM Probe Displacement Measurement System	45
3.1.4	AFM Probe Holder	51
3.2	Electrical Design	52
3.2.1	Power Circuitry	52
3.2.2	Photodetector and Gain Circuitry	54
3.3	Control and Data Acquisition System	57
3.3.1	Controller Design and Implementation	57
3.3.2	Data Acquisition System	60
3.4	Fabricated Design	61
3.5	AFM Characterization	68
3.5.1	AFM Operation Validation	72
4	Multifunctional Probe Design, Model, and Fabrication	78
4.1	Electro-Thermo-Mechanical Modeling	80
4.2	Dynamic Modeling	88
4.3	Design Tradeoffs	93
4.4	Fabrication	94
4.4.1	Fabrication Challenges	101
5	ETM Actuator Characterization	102
5.1	Dynamic Response	102
5.2	Electrical Characterization	105
5.3	Displacement Characterization	113

5.4 Application	115
6 Discussion	120
7 Conclusions and Future Work	124
A MATLAB ETM Model Code	137
B Microcontroller Code	139

List of Figures

1.1	An example SPM, the atomic force microscope: (a) scan-by-sample system and (b) scan-by-probe system.	2
1.2	Multifunctional scanning probe-based automated platform concept.	3
2.1	Scanning tunneling microscopy concept illustration.	15
2.2	Atomic force microscopy concept illustration.	17
2.3	Commonly used AFM detection systems for cantilever deflection measurements: (a) STM, (b) laser beam deflection, (c) optical interferometry, and (d) capacitance.	18
2.4	Two scanning methods: (a) scan by probe and (b) scan by sample.	19
2.5	Concept illustration of AFM optics.	20
2.6	Block diagram of a scan by probe AFM system.	21
2.7	Three common AFM imaging modes: (a) contact mode, (b) noncontact mode, and (c) dynamic mode.	23
2.8	Nanosurf's easyScan commercial AFM system [1]. The photo shown here is borrowed from the citation.	26
2.9	Two most common AFM probe layout configurations: (a) bottom view of triangular probe, (b) alternative view of triangular, (c) bottom view of cantilever probe, and (d) alternative view of cantilever probe	28

2.10	Scanning electron microscopy image of a typical atomic force microscopy probe with tip [2]. The photo shown here is borrowed from the citation.	29
2.11	ETM actuation and displacement concept with applications: (a) actuation displacement, (b) resistive heating concept, (c) force multiplication application, and (d) AFM multifunctional probe application.	32
2.12	ETM actuators: (a) [3] and (b) [4] are composed only of silicon and utilizes varying cross-sectional areas for actuation, while (c) [5] and (d) [6] are composed of silicon and SU8 where the material property mismatch is exploited for actuation. The photos shown here are borrowed from the citations.	33
3.1	Block diagram of the custom AFM system's major components: (a) simplified functional block diagram and (b) complete AFM signal block diagram.	37
3.2	Reverse engineering a commercial AFM system into its various components: (a) video system, (b) AFM base, (c) scanning head, and (d) scanning head cover.	39
3.3	The (a) block diagram of stepper motor's implementation and contribution to vertical displacement along with the arrangement of components attached to top of AFM base platform: (b) stepper motor orientation and (c) laser trajectory.	42
3.4	Top view of AFM base platform with stepper motor placement measurements at the following locations: (a) motor 1, (b) motor 2, (c) motor 3, and (d) center.	43
3.5	Coordinate system for nanopositioner with piezoactuator orientations.	45
3.6	The (a) laser's trajectory and the (b) layout of mirror holder and AFM optics.	48

3.7	Mirror holder FEA frequency response analysis depicting the first mode shape at 19.2 kHz.	49
3.8	Quadrant photodetector sensor illustration of: (a) sensor configuration, (b) equivalent circuit representation, and (c) actual photodetector. . .	50
3.9	AFM probe holder with inclination angle identified (θ).	51
3.10	Power supply for AFM circuits and voltage references	53
3.11	Circuit schematic of quadrant photodetector circuit where 1, 2, 3, and 4 represent the output from each quadrant of the photodetector. . . .	55
3.12	Quadrant photodetector sensor circuit that performs the following procedures: (a) converts current signal to voltage signal, (b) buffers the voltage signals, and (c) adds and subtracts voltage signals for AFM probe displacement data.	56
3.13	ATxmega128A1 microcontroller: (a) component labeling and (b) pin assignments.	60
3.14	Overview of completed custom AFM system.	62
3.15	LabVIEW AFM program: AFM imaging screen.	63
3.16	LabVIEW AFM program: stepper motor control with (a) automatic approach and withdraw, (b) manual movement, and (c) stepper motor settings.	64
3.17	LabVIEW AFM program: (a) AFM imaging settings and (b) photodetector alignment screen.	65
3.18	Flow chart for AFM program operation part 1 of 2.	66
3.19	Flow chart for AFM program operation part 2 of 2.	67
3.20	Nanopositioner frequency responses for (a) x -axis (actuation) to x -axis (sensing), (b) x -axis to y -axis, (c) y -axis to x -axis, and (d) y -axis to y -axis.	69

3.21	Time response of cross coupling from (a) x -axis to y -axis and (b) y -axis to x -axis	70
3.22	Block diagram of the modeled system.	71
3.23	The z -axis experimental frequency response compared with model. . .	72
3.24	PSD sensor output and piezo input voltage for a 256×256 pixel image at a 1-Hz line rate scan with no controller or z -axis input. Two-dimensional plots are presented in (a), while a three dimensional PSD sensor plot is presented in (b, left) and a rotated side view PSD sensor plot is presented in (b, right).	73
3.25	PSD sensor output and piezo input voltage for a 256×256 pixel image at a 1-Hz line rate scan with the following controller gains: $K_p = 1 \times 10^{-6}$ and $K_i = 1 \times 10^{-11}$. Two-dimensional plots are presented in (a), while a three dimensional piezo amplifier input voltage plot is presented in (b, left) and a rotated side view piezo amplifier input voltage plot is presented in (b, right)	74
3.26	PSD sensor output and piezo input voltage for a 256×256 pixel image at a 1-Hz line rate scan with the following controller gains: $K_p = 2 \times 10^{-2}$ and $K_i = 1 \times 10^{-5}$. Two-dimensional plots are presented in (a), while a three dimensional PSD sensor and piezo amplifier input voltage plots are presented in (b, left) and (c, left), respectively and PSD sensor and piezo amplifier input voltage plots are rotated side views are presented in (b, right) and (c, right), respectively.	75
3.27	Flow chart for atomic force microscope setup.	77
4.1	Multifunctional probe implementation into atomic force microscopy system with scanning application.	78

4.2	Interchangeable tip concept of the multifunctional probe application for the following tasks: (a) discarding worn or fouled tip, (b) grasping a new tip, and (c) releasing tip from tip holder begin specialized tip operations.	79
4.3	Multifunctional probe modeling parameters: (a) multifunctional probe dimensions, (b) model simplification, (c) model coordinate system, and (d) heat flow within the probe.	81
4.4	Temperature distribution along the multifunctional probe.	86
4.5	Multifunctional probe displacement along its length: (a) displacement plots and (b) corresponding geometric layout of the plots.	87
4.6	Deflected cantilever with variable assignments for dynamic model. . .	89
4.7	Mode shapes and modal frequencies from FEA for non-simplified multifunctional probe.	93
4.8	Personal protection for University of Florida clean room facility: (a) general protective clothing and (b) wet chemical (acid) protection clothing.	94
4.9	Fabrication process for multifunctional probe.	96
4.10	Fabrication photos for photolithography process (mask): (a) and (b) Al sputter coating, (c) and (d) Photoresist spin coating, and (e) and (f) mask transfer.	97
4.11	Fabrication photos for photolithography process (etching): (a) and (b) photoresist layer is developed and (c) and (d) aluminum layer is etched.	98
4.12	Fabrication photos for: (a)-(c) deep reactive ion etching and (d)-(f) dicing	100

4.13	Scanning electron microscopy images of fabricated multifunctional probes with the following views: (a) overview of released probe with support structure, (b) zoomed in on probe gripper end, (c) angled view 1, and (d) angled view 2.	101
5.1	Dynamic response data for: (a) AFM stage using a laser vibrometer (G1) and multifunctional probe using the AFM's photodetector (G3) and (b) the calculated multifunctional probe response.	103
5.2	Multifunctional probe power and current measuring circuit.	106
5.3	Gold wire bonds from multifunctional probe chip out to circuit.	107
5.4	Multifunctional probe mean current flow throughout and standard deviation from 1 to 13 V input voltages during: (a) and (b) 1 st actuation, (c) and (d) 5 th actuation, and (e) and (f) 10 th actuation. Tests are performed with a 1-Hz square wave.	108
5.5	Current time response data for the following input voltages: (a) and (b) 1 V, (c) and (d) 3 V, (e) and (f) 5 V, (g) and (h) 7 V, (i) and (j) 9 V, and (k) and (l) 10 V. Tests are performed with a 1 Hz square wave.	110
5.6	Time response current data with standard deviation bars plotted for the following input voltages: (a) 1 V, (b) 3 V, (c) 5 V, (d) 7 V, (e) 9 V, and (f) 10 V. Tests are performed with a 1-Hz square wave.	111
5.7	Time response resistance changes for the multifunctional probe for: (a) 1 V input, (b) 5 V input, and (c) 10 V input.	112
5.8	Multifunctional probe actuation under various driving voltages: (a) 5 V, (b) 10 V, and (c) 13 V.	113
5.9	Plot of probe actuation displacements under various input voltages: (a) measured data and (b) 'linear' operating range with linear fit.	114

5.10	Experimental setup for demonstrating the multifunctional probe's gripping ability.	116
5.11	Demonstration of wire gripping ability at various angles: (a) back angled side view, (b) side view, (c) front angled side view, and (d) zoomed in side view.	117
5.12	Demonstration of probe's pick and place capability with time progression from top to bottom of: (a) probe's grasping capability and (b) probe's translation and releasing capability.	119

List of Tables

1.1	Comparison of probe-based technologies and proposed active cantilever.	7
2.1	Specifications for Noliac SCMAP07 actuators used in the custom AFM scanner.	24
3.1	Summary of AFM optical system components.	51
4.1	Calculated lateral displacement at the distal end of multifunctional probe.	88
4.2	Eigenvalues for a clamped - free cantilever beam.	92
4.3	Calculated modal frequencies for an equivalent beam model of the multifunctional probe with a constant cross-sectional area throughout. . .	92

Chapter 1

Thesis Goal, Objectives, and Contribution

The goal of this thesis is create a scanning probe microscopy platform for multi-functional probe-based interrogation, manipulation, and fabrication of objects and matter at the micro to nano-scale. A newly designed and fabricated electro-thermo-mechanical (ETM) cantilever with a microgripper at its distal end is designed for automated pickup and release of tool tips. This unique platform will help address the critical issues of throughput, repeatability, scalability, and limited functionality of probe-based applications including multi-process nanofabrication. It is pointed out that in traditional atomic force microscopy (AFM), a type of scanning probe microscopy (SPM), the probe tool is an integrated (monolithic) microcantilever with a sharp tip at its distal end. In AFM, a stage is used to position a small SPM probe relative to a specimen for nano-scale imaging, surface modification and interrogation. Unlike a traditional optical microscope which uses light for imaging, in SPM an image is formed by raster scanning a small (typically micron-size) probe over a sample surface and then plotting the probe's interaction as a function of its position. For example, consider the basic scan-by-sample and scan-by-probe AFMs shown in Fig. 1.1. When the probe tip is raster scanned over a sample's surface, tip-to-sample interaction causes the cantilever to deflect vertically with respect to the sample topography. The deflection is then measured and used to construct an image of the sample

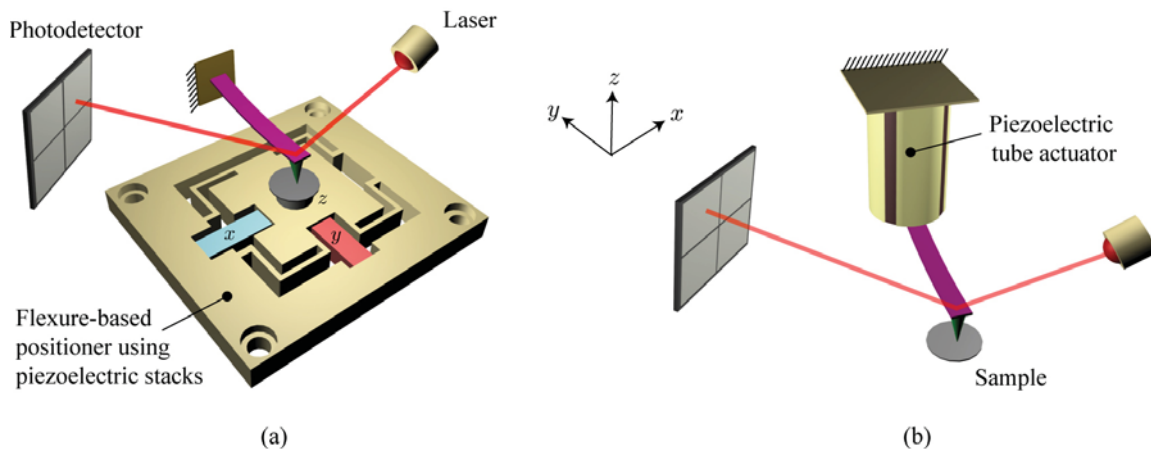


Figure 1.1: An example SPM, the atomic force microscope: (a) scan-by-sample system and (b) scan-by-probe system.

surface. In this case, the AFM essentially ‘feels’ the surface with a tiny, finger-like cantilever. In a vacuum an AFM’s resolution is on the order of 0.01 nm. With such high resolution, an AFM can generate topographical images of atoms, as well as to control, manipulate, and alter the properties of matter at the nano-scale.

During routine operations when the tool tip is damaged or contaminated, replacement of the probe tool is needed which requires replacement, re-alignment, and calibration of a new cantilever probe tool and opto-electronics. The process of replacing the probe tool can be time consuming and is a limiting factor in high throughput SPM applications. However, in order to enable practical SPM applications, it will be critical to address the issues of throughput, tip wear effects, chemical cross contamination, and scalability all of which act to decrease the quality, reliability, and efficiency of probe-based fabrication. To address these critical issues, a multifunctional AFM platform is created which consists of an active ETM cantilever with an automated ability to interchange probe tips, for example, from sharp pyramidal tips with various sizes and materials to chemically functionalized tips for biological printing to nanowire tips for high resolution metrology to dynamic tips that can be used for machining, nanomanipulation, or material modification; without the need for

an operator to physically remove/replace the cantilever as in traditional SPM. This novel design models macroscale computer numerical control (CNC) manufacturing in which CNC machines are fully automated allowing for rapid tool changes without operator interruption. A concept illustration is presented in Fig. 1.2, which shows the envisioned fabrication work space and the ETM active microcantilever (gripper) and modular tool tips. Located at the distal end of the active cantilever is an electrically activated MEMS-based microgripper, which is designed to automatically load/unload tips from an array of modular probe tips (tools). The proposed technology is scalable: arrays of these active cantilevers and modular tips could be used and interchanged for nano-scale rapid prototyping or nanofabrication. The proposed ETM cantilever is specifically designed for AFM applications and the objectives to achieve the goal are to:

1. Design and fabricate an active electro-thermo-mechanical cantilever with the ability for automated tool tip change;
2. Characterize the performance of the ETM cantilever; and
3. Create a versatile AFM platform to enable the capabilities of the ETM cantilever.

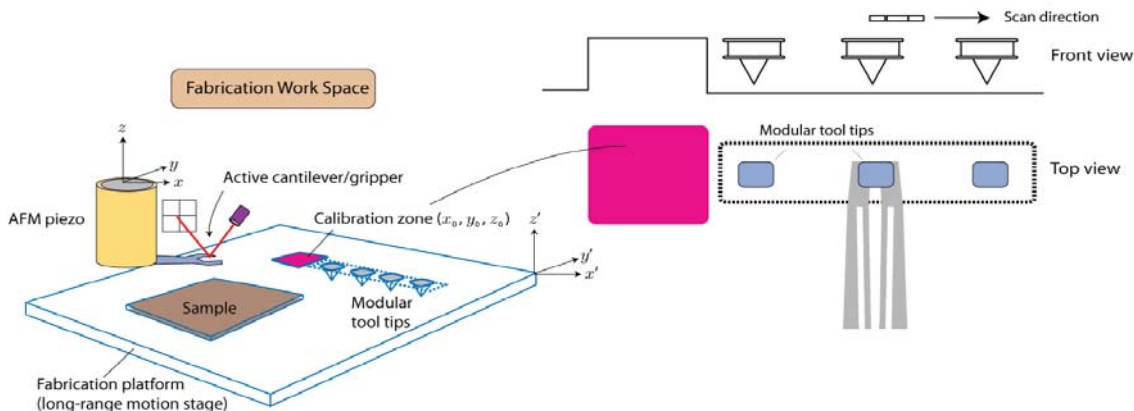


Figure 1.2: Multifunctional scanning probe-based automated platform concept.

The results and outcomes of this thesis lay the foundation for future work in multi-functional probe-based applications which include handheld replicators for nano rapid prototyping of nanoelectronics and NEMS, printing and nanomachining of unique hybrid organic and inorganic material, 3-D nanofabrication and assembly, and complete desktop nanofactories. More specifically, the AFM platform with the active ETM cantilever can be used for nanoparticle manipulation [7], surface modification (scratching) [8,9], indentation [9], and nanomachining [10], as well as processes where different tips are required to complete a process. The main contributions of this research are the design, characterization, and demonstration of the capabilities of the ETM cantilever for pick and place operations to facilitate a streamline tool tip change procedure without the need for additional time consuming tasks.

1.1 Overview

AFM has seen significant advances in control [11–13], optics design [14–17], tip resolution [18,19], and applications [20–24]. Despite these recent advances, the traditional microcantilever with an integrated fixed tip at the distal end offers limited functionality and when damaged or contaminated, is time consuming to replace. Most commercially available AFM probes have only a single AFM tip mounted to a large base platform (*i.e.*, Budget Sensors’ AFM probe model ContAL-G). While some manufacturers place multiple tips on a single AFM probe base, limitations still exist due to the fixed structure of the tip.

Another issue with traditional AFM probes is the calibration requirement of each individual AFM probe. Due to inherit fabrication variances in AFM probe fabrication, each individual AFM probe can have significant geometric variances that can greatly impact its performance. For example, Budget Sensors’ ContAL-G AFM probe is a typical AFM probe that has the following dimensions: $450\ \mu\text{m} \pm 10\ \mu\text{m}$ for length,

$50\ \mu\text{m} \pm 5\ \mu\text{m}$ for width, and $2\ \mu\text{m} \pm 1\ \mu\text{m}$ for thickness. With such varying geometries, individual cantilever calibration is a must for any force sensitive application. This particular commercially available AFM probe has a specified force constant that varies an order of magnitude (according to the manufacturer's specifications). By utilizing a single active microgripper with the ability for quick tool-tip changes, an automated process can be implemented to enhance throughput and performance similar to traditional macro-scale CNC machines. The proposed active SPM probe leads to a more robust multifunctional system that can perform several separate procedures with customized tips to increase current traditional AFM based imaging and fabrication throughput.

1.2 Motivation and Contribution

The scanning probe microscope, in particular the AFM, is the workhorse of emerging science and technology at the nano-scale. By maneuvering a cantilever tip relative to a sample, the AFM can be used to image [25], manipulate [26], and fabricate [27] features down to the sub-nanometer level. The AFM can not only study inorganic samples, but also investigate organic specimens, for example biological cells and molecules [28] and DNA [29]. Likewise, the AFM has proven its usefulness in many fields of science and technology, yet the system has several drawbacks which hinders its use for practical nanofabrication applications.

One such limitation that has been pointed out is the inefficient retooling process, where the tool tip is manually changed. The process for a trained individual can take several minutes to complete. Furthermore, inconsistencies between cantilevers even within the same production batch leads to required individual AFM probe calibrations for performance critical applications (*i.e.*, force sensitive, resonant dependant,...etc). This is a cumbersome process when trying to implement a multi-step, multi-probe

process. Existing AFM systems that use a single probe for one, maybe two and at most three applications provide limited functionality. For example, contact mode tips can be used for imaging, scratching, and/or indentation [30]. While a single tip can be used for multiple applications, the optimal solution is to use a different tip for a different process. Fabrication processes that require a large number of steps may require a library of AFM probe tips/tools. By changing probe tips for different operations, throughput of the fabrication process will be greatly reduced as well as repeatability and quality of the fabricated structure. The process of manually changing probe tools is cumbersome, inefficient, and presents opportunities for damaging the AFM probe.

As the interest in developing large arrays of nanostructures and nanodevices increase, the need for multifunctional, highly repeatable probes will become more important. For example, these structures will need highly specialized probes to create, measure, and investigate their properties. Several groups have already recognized the need for highly functional probes. For example, Xi's group created an active AFM probe that changes its rigidity through different control strategies for imaging and manipulation modes [31]. In addition, multiple AFM probes have been proposed on a single chip in order to increase throughput as well as expand its functionality. This concept was recently demonstrated by Liu's group [32], as well as by others for parallel AFM imaging [33, 34], dip-pen nanolithography [35], and high-density data storage [36]. Although multiple probes (more than one on a single carrier substrate) can broaden the application of AFM, other challenges still remain. For example, each probe must be carefully calibrated to ensure optimal performance, which may involve individually actuating a probe such that the appropriate tip-to-sample interaction is achieved for proper operation. Also, chemically fouled, worn out, or damaged tips will need to be replaced. This replacement is wasteful if only a single tip on an array

needs to be replaced, but the whole array needs replacing due to the single carrier substrate for all of the probes. The replacement process require an operator to manually change and recalibrate the AFM probes, just like the replacement process for single AFM probes. This changing/replacing/replenishing process can be time consuming and as the number of steps and processes increase to fabricate a feature, the quality, reliability, and repeatability decrease dramatically due to repeated manual swapping of probes.

The contribution of this work presents a significant benefit for AFM-based applications. This thesis demonstrates that a thermal microgripper can be used for object manipulation, while still maintaining traditional AFM probe dynamics. Table 1.1 compares the benefits of the proposed active ETM microgripper SPM probe to conventional probes. A custom-designed AFM platform is designed which uses the active electro-thermal microcantilever for multifunctional applications.

Table 1.1: Comparison of probe-based technologies and proposed active cantilever.

Probe Technology	Throughput	Functionality	Cost	Scalability
Single probe [37–41]	Low	Low	Low	High
Multi probe [32, 33, 36, 42]	Medium	High	Low	High
Proposed ETM probe	High	High	Low	High

1.3 Methodology

1.3.1 Why Electro-Thermal-Mechanical (ETM) Actuation?

ETM actuation is selected for its low power requirements, moderate actuation displacement, and sensing capabilities. Other actuation methods are available for the gripping mechanism of the multifunctional probe, yet specific drawbacks apprehend their implementation. Gripper designs have been proposed in the past and in general the following are the available motion mechanisms: (1) electrostatic actuation [43], (2)

thermal actuation [44,45], (3) piezoelectric actuation, (4) magnetic actuation, and (5) shape memory alloy actuation [46]. Piezoelectric actuators are rather limited for use as microgrippers due to their low percent strain (approximately 0.1%). Shape memory alloy-based microactuators has been developed that produces over 5% strain [46]. However, shape memory alloy materials are difficult to fabricate into custom geometries at the micron-scale because of their fabrication process that involves sputtering and careful stoichiometry control. Micron-sized electrostatic actuators have been developed to manipulate objects, such as nanowire [47]. However, large electric fields (as large as 100 V) are required for large motion and the large fields can induce unwanted electrostatic forces with nearby objects. One alternative to avoid this is to use thermal-based actuators [48]. For example, a thermal actuator was developed that requires 75 mW of power to expand by 35 μm [49]. Thermal actuators have many advantages and is chosen as the motion mechanism for creating an active cantilever for several reasons. First, they can provide a significant amount of force for gripping and holding the tool tip. Second, the fabrication process to create a micron-size thermal gripper is well established and straightforward [48]. Lastly, the thermal behavior of the gripper can be exploited to create a sensor to detect the location of modular tips for loading/unloading. Compared to the other gripping mechanisms presented in this section, ETM actuation is chosen to be the best selection for the multifunctional probe's gripping mechanism in terms of power consumption and sensing capabilities.

1.3.2 ETM Multifunctional Probe Design

The ETM actuator is designed to align with traditional AFM cantilevers while providing a means for grasping modular AFM probe tips. In the design of the ETM probe, the overall length dimension is to be restricted within standard AFM contact mode probe lengths, which can be as long as 450 μm . After preliminary analysis, the

small base cross-sectional area coupled with the larger cross-sectional area tip leads to unfavorable dynamic response simulation results. To solve this issue, the probe's base cross-sectional area is increased and the tip cross-sectional area is decreased, but this leads to a substantial decrease in actuation displacement. An iterative process is employed to determine the trade-offs between cross-sectional area distribution and actuation displacement. The final result is a unique tapered design with a large base cross-sectional area that tapers to a smaller tip cross-sectional area. This design provides over 3 μm of individual actuator displacement (measurements from dual actuator testing resulting in 6.4 μm displacement), while maintaining a dynamic response similar to a traditional AFM probe with a first modal frequency in the tens of kHz.

1.3.3 Multifunctional Probe Characterization

The actuator characterization process includes the following measurements: optical microscope steady state displacement measurements, time constant for steady state actuation, actuation repeatability quantification, and dynamic response results. Displacement, actuation time constant, and repeatability tests are all conducted using custom circuitry to power the multifunctional probe, while monitoring the electrical current flowing through the probe. Dynamic response plots are gathered by utilizing the z -axis piezoelectric actuator of the custom designed AFM to provide an excitation signal into the base of the multifunctional probe, while recording the photodetector sensor output throughout a frequency range sweep (up to 100 kHz) using a Stanford Research Dynamic Signal Analyzer and a high-bandwidth power amplifier centered, which centers around a Power Amp Design PAD129 power op-amp [50]. Lastly, object manipulation is demonstrated using the custom AFM, custom manual translation object holder, and multifunctional probe.

1.3.4 Custom AFM Design for Multifunctional Probe

A custom AFM is designed for testing and evaluating the multifunctional probe and also provides a basis for future work. The custom designed AFM offers flexibility compared to a commercial AFM system which cannot be easily adapted to work with the newly designed multifunctional probe. Also, research grade AFM systems with the required system flexibility typically costs on the order of \$100,000 and greater. It is pointed out that lower cost systems are available but have reduced performance and system flexibility compared to their higher cost counterparts and are limited by their scan range, scan speed, and overall system robustness. For example, the easyScan AFM requires cantilevers with alignment groves due to its fixed optical system, so custom applications are not feasible because system modification is required. For these reasons, a custom AFM is required to provide the flexibility needed for initial multifunctional probe characterization and testing. It will also be used as a prototype for a future desktop nanofabrication system.

The mechanical design for the AFM incorporates a two axis nanopositioner [50] with custom probe holder and actuator for precise x , y , and z control. The z -axis probe holder is mounted onto the x, y translation stage for a three axis probe positioning system. The control system for the AFM incorporates an Atmel ATxmega128A1 microcontroller for z -axis control. Other custom system components include: photodetector circuitry, three independent stepper motors for the AFM's approach mechanism, LabVIEW software for AFM control and data acquisition, TREK piezoelectric amplifiers (models: PZD700 and 603), custom interface circuitry between the AFM, and microcontroller.

1.3.5 AFM Platform Testing

The AFM platform is characterized to determine system performance capabilities and system limitations. Validating the AFM is performed using a commercially available calibration sample (Nanosurf No. BT01015 with $10\ \mu\text{m}$ x, y periodicity and 98 nm z depth) with commercial contact mode AFM probe (BudgetSensors' ContAL-G). A proportional-integral (PI) z -axis controller is implemented into the system using a microcontroller (ATxmega128A1) for constant height and constant force operation modes. Lastly, AFM imaging results are presented to verify proper system operation.

1.4 Summary of Completed Work

The expected outcome of this work is to have a completed custom-made AFM system with an active microcantilever that has the ability to perform autonomous tip tool changes. This section summarizes the completed work presented in this thesis.

First, a versatile scan-by-probe AFM platform is designed. The scan by probe design is chosen since it imposes no limitations on sample size or mass. This design also allows one to integrate a high-speed nanopositioner for high-bandwidth applications such as video-rate AFM. The AFM utilizes an optical displacement measurement system to measure the AFM probe's displacement. Stepper motors provide the approach mechanism and a microcontroller allows for closed-loop control of the z -axis. A custom LabVIEW program is created to control the AFM system. All sensors, circuits, and physical parts are highly adjustable and can be modified or replaced if needed. Experimental frequency response data and models for the x , y , and z axis are presented for future work.

Second, the multifunctional ETM-based probe is designed such that each actuator arm is within typical AFM probe dimensions. The dynamic response of the probe

has the first two mode shapes of a traditional cantilever beam, with the first modal frequency in the same range as an AFM probe (tens of kHz). The actuator utilizes a resistive heating effect to provide 2 μm of displacement with 5 V DC input. A frequency response is conducted to verify that design does have a traditional cantilever beam first mode shape with a first modal frequency in the tens of kHz. Electrical response plots are also obtained by actuating the probe under constant voltage and recording the current flow through the probe.

Lastly, the AFM-based nanofabrication system is integrated with the multifunctional ETM-probe to demonstrate the pick and place capability of the system. The ETM-probe is used to grab and release a small-diameter wire to demonstrate the pick and place capability.

Remaining tasks that need be completed for a fully autonomous multi-process nanofabrication system include: modular tool tip design and fabrication, investigating thermal sensing capability of multifunctional probe, and modifying AFM software for fabrication and autonomous operation. The modular tool tip design needs to incorporate different tool designs, so that multiple fabrication processes can be demonstrated. A challenging aspect of the design and fabrication of the tool tips is that the tips are most likely supported using tabs made out of silicon. The array of tips will have to be strong enough to survive the fabrication process, yet weak enough to be removed by the multifunctional probe (also made out of silicon) without damaging the probe. The multifunctional probe also needs to be investigated for its thermal sensing capability. Modifications to the design may be needed to incorporate an enhanced thermally sensitive area of the probe for thermal sensing. This may involve fabricating a thermal sensing structure beside the probe or integrating the sensor area into the probe and having separate driving and sensing current flow paths. Lastly, when the above tasks are completed, the custom AFM program can be modified to

implement the sensing and automatic tool changes into the current program's code.

1.5 Organization

The remainder of this thesis is organized as follows. In Chapter 2, scanning probe microscopy is introduced. AFM probes, piezoelectric actuators, and AFM imaging modes are covered in this chapter. Chapter 3 provides the details of the custom-made AFM system, including characterization and validation of system operation. Next in Chapter 4, the multifunctional probe's design and ETM model are presented. The model estimates the deflection of the gripper for DC input voltages. Also included in this chapter is the fabrication process, which is followed by the characterization process and experimental results. A detailed discussion of the results is presented in Chapter 6. Lastly, concluding remarks and future work are presented in Chapter 7.

Chapter 2

Background

This chapter provides background information on scanning probe microscopy, particularly the AFM, and electro-thermo-mechanical (ETM) actuators with emphasis on silicon-based actuators. The background section will serve as an introduction to those unfamiliar with either of the topics presented and well as give insight into some of the challenges that exist for the design and implementation of these devices. Lastly, a summary of the most important points with their implications on the design of both the custom AFM and ETM multifunctional probe is presented.

2.1 Scanning Probe Microscopy

Scanning probe microscopy can be described as a system that measures a surface's topology by using a sharp tip that is moved (scanned) relative to a sample's surface. The surface's topological characteristics are measured by a sharp tip or probe either by its physical or electrical interaction with the surface. The SPM is separated into two distinct categories: scanning tunneling microscopy (STM) and atomic force microscopy (AFM).

2.1.1 Scanning Tunneling Microscopy

The STM is the first SPM instrument and was introduced by Binnig et. al. in 1982 [51]. The STM utilizes an electrical conducting probe tip that is scanned across a conductive surface within close proximity (approximately 1 nm) using a constant tip-to-sample tunneling current. The constant tunneling current is maintained by moving the probe relative to the sample surface (scan by probe concept, see Fig. 2.4 for other scan types) by changing the input voltage to the piezoelectric drive actuators. The piezoelectric drive actuators move the tip in the vertical axis to maintain a constant tip height above a sample. A depiction of the vertical axis movement during scanning is shown in Fig. 2.1 where the z -direction is the vertical axis.

Figure 2.1 shows a conductive probe being scanned over the surface along the solid black line trajectory. The probe tip voltage potential relative to the sample surface is denoted by V_t . Typical tip operating voltages range from 10 mV to 1 V, while tunneling current varies from 0.2 nA to 10 nA. The corresponding tip height,

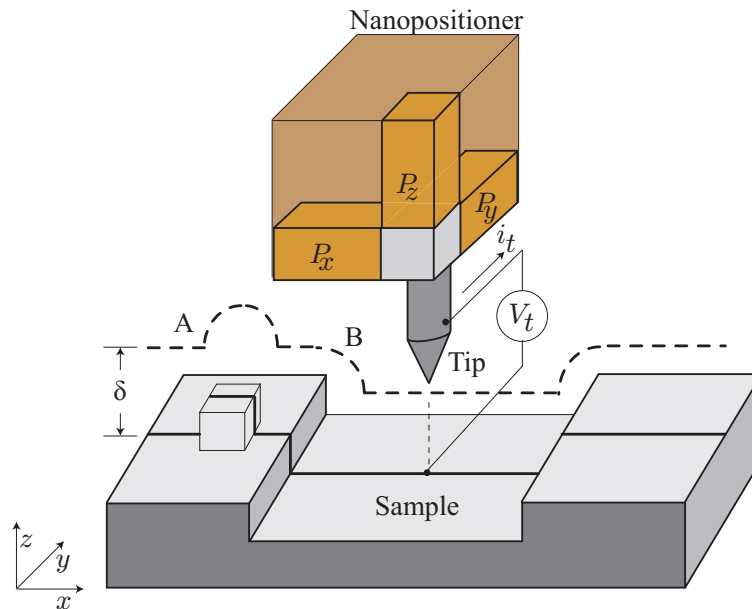


Figure 2.1: Scanning tunneling microscopy concept illustration.

δ , is shown as a dashed line. The piezoactuator drive voltages are denoted by P_x , P_y , and P_z for the x -axis, y -axis, and z -axis, respectively. While the tip is being scanned over the surface, the vertical motion of the piezoactuator controlled by P_z is modulated to adjust the height of the tip, so that constant tunneling current, i_t , is maintained throughout the scan from left to right. This mode of scanning is called constant-current mode. By monitoring the input voltages to the piezo-drive, surface topology measurements can be obtained, which are used to produce a topographic image of the sample's surface. Typical tip height, δ , during scanning is approximately 1 nm, which results in vertical resolution of about 0.1 nm. High vertical resolution is attributed to the tunneling current and how it varies exponentially as the tip height is changed. Lateral resolution depends on tip's curvature radius. Tips are typically tungsten wire with a tip radius in the range of 0.1 nm to 10 μm . A drawback of this imaging method is that STM imaging requires a conductive sample surface to facilitate the current flow from the STM tip to the sample. Nonconductive surfaces have to be coated with a thin layer of conductive material in order to be imaged. If the sample is not conductive and coating the sample is not possible, STM is not a viable option for imaging, so an alternative method is required (atomic force microscopy).

2.1.2 Atomic Force Microscopy

In 1986, Binnig et al. introduced atomic force microscopy, which allows imaging of non-conducting samples [52]. A schematic of the initial concept is shown in Fig. 2.2, which utilizes an STM that measures a cantilever beam's deflection as it is scanned across a sample.

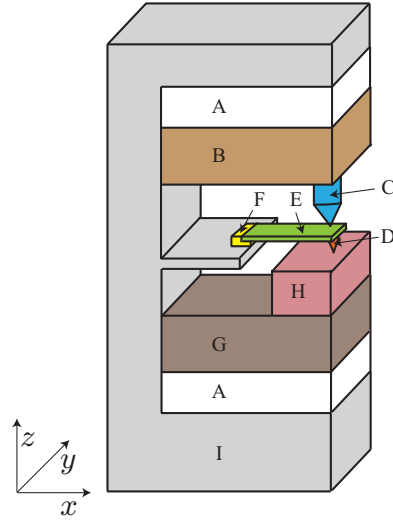


Figure 2.2: Atomic force microscopy concept illustration.

The figure shows a cantilever beam (E) with a sharp tip (D) in contact with an AFM sample (H). The cantilever beam is attached to a modulating piezoelectric actuator (F) that drives the cantilever beam at its resonant frequency. The sample is mounted to a three axis piezoelectric feedback scanner (G) that moves the sample relative to the fixed probe. The backside of the cantilever beam is conductive and is used as the sample surface for the STM tip (C). The STM tip also has its own z -axis control system (B). Both the AFM and STM feedback system as well the cantilever modulating piezo are all mounted to a single aluminum support structure (I). The AFM and STM feedback systems have spacers (A) to dampen the high frequency mechanical vibrations from outside the system (I) and within (B,F,G).

Other commonly used methods to measure the cantilever deflection are presented in Fig. 2.3. The STM method is the same as the method used by Binnig et. al. discussed above. The laser beam deflection method utilizes a laser beam reflected off of a AFM probe and into a position sensitive detector, which measures the probe's displacement as it is scanned across a sample's surface. The laser beam deflection method is used in the custom AFM design and will be discussed in more detail later

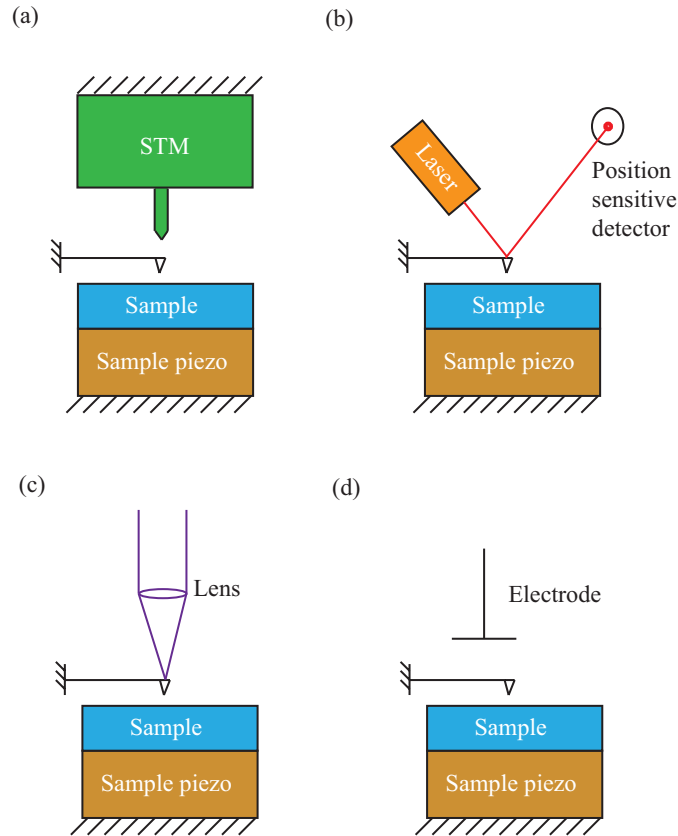


Figure 2.3: Commonly used AFM detection systems for cantilever deflection measurements: (a) STM, (b) laser beam deflection, (c) optical interferometry, and (d) capacitance.

in this section. Optical interferometry uses the a lens to focus the light source onto the cantilever beam and the reflected light is then directed back into the optical fiber, where light intensity and phase can be analyzed for displacement measurements. The capacitance method measures the changes in capacitance between an electrode above the AFM cantilever and the cantilever itself, so as the cantilever deflects its capacitance will change with the change in displacement. Optical interferometry and capacitance methods will not be discussed in detail for this document and are only presented here for completeness.

Figure 2.4 presents the two general AFM scanner-sample configurations. The first configuration is shown in Fig. 2.4(a), where the AFM probe is attached to a

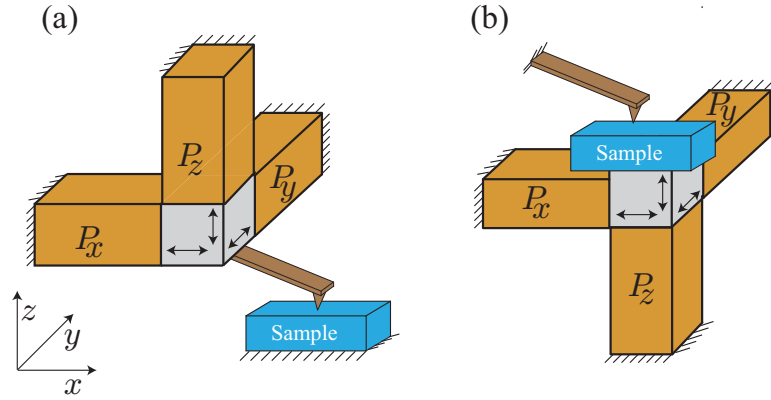


Figure 2.4: Two scanning methods: (a) scan by probe and (b) scan by sample.

translation stage (gray block) which is moved by the three piezoelectric actuators for example (P_x , P_y , and P_z) while the sample remains stationary. This method is called scan by probe because the probe is being scanned across a stationary sample surface. In contrast, scan by sample is shown in Fig. 2.4(b), where the sample is translated using the three piezoelectric elements (P_x , P_y , and P_z) while the AFM probe remains stationary. The scan by probe method allows for a wider range of samples since the only moving part is the probe, which allows the user to place the AFM onto almost any surface. On the other hand because the probe is moving throughout the scan, the AFM system is slightly more complicated since the displacement measurement system should move with the probe to ensure proper measurements. For example in the laser beam deflection method, the laser beam should stay on the same probe location to ensure accurate deflection measurements and a moving probe relative to a stationary beam will not result in such a scenario. Scan by sample allows for a simpler design since all scanning motion is performed by the sample and this allows for a fixed optical system and less moving parts; however, the sample's size is restricted to the provided sample tray. As well as sample size, sample mass is limited since increasing the sample's mass will affect the AFM scanner's dynamic response. For the custom AFM design, a scan by probe design is implement to accommodate a wide range of

samples. Using this approach, future applications could utilize both a scan by probe and a scan by sample mechanism.

In 1988, an optical sensing approach to detect probe deflection is first introduced and became widely adopted in today's commercial AFMs [53]. The Meyer and Amer sensing approach utilizes a reflected laser beam that is reflected off of the backside of an AFM probe and terminates at a position sensitive detector. The position sensitive detector (PSD) measures the deflection of the probe's cantilever beam by tracking the displacement of a laser beam spot on the detector's surface. This sensing concept is shown in Fig. 2.5.

The figure shows a probe that resembles a cantilevered beam with a mirror-like surface attached to its backside that reflects a laser beam. While the cantilever beam is scanned across the sample surface, the cantilever deflects due to changes in surface topography resulting in changes in the laser beam's trajectory and leading to displacement of the laser beam spot on the position sensitive detector. Nanosurf's easyScan AFM utilizes this same concept by using a fixed-mounted quadrant photodetector as the position sensing detector, reflective coated cantilever probes, and fixed laser. The quadrant photodetector provides more information than solely topo-

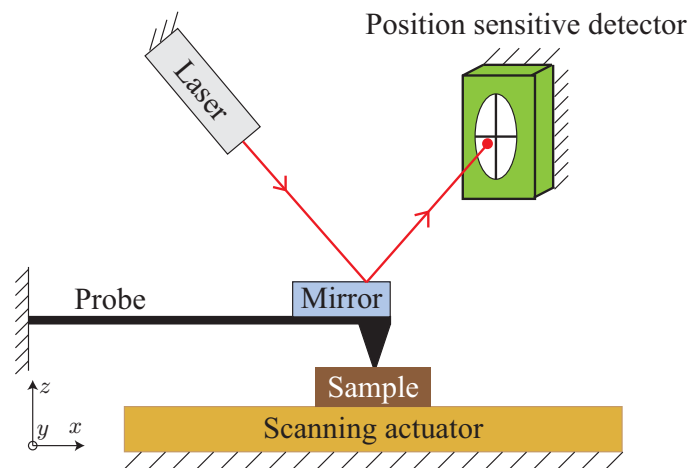


Figure 2.5: Concept illustration of AFM optics.

logical (z -axis displacements). Frictional forces can be measured by recording y -axis displacements, which are seen as cantilever tilting or twisting [54]. A quadrant photodetector is integrated into our AFM system to provide future capabilities to our system.

Using the laser deflection method, requires that the laser spot on the back of the cantilever maintain a constant position on the cantilever. This can be accomplished by using a focusing lens that moves with the cantilever, while the cantilever transverses during scanning. Scan range is improved and beam trajectory shifting is decreased by reducing non parallel incident rays to the focusing lens [17]. A typical scan by probe AFM block diagram using this laser deflection method is shown in Fig. 2.6.

The AFM scanner provides the x , y , and z translation of the AFM cantilever and tip. The cantilever's response to the sample's surface topography is recorded using an optical deflection sensor (laser and photodetector). The deflection signal is relayed to the z -axis feedback controller, which provides control of the AFM's imaging mode by

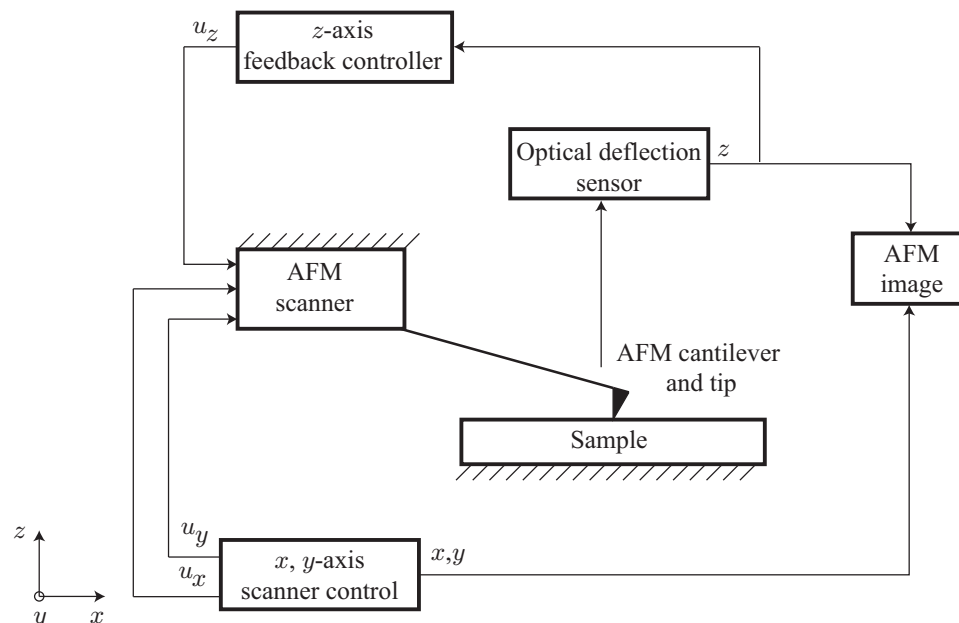


Figure 2.6: Block diagram of a scan by probe AFM system.

adjusting the z input (u_z) to the AFM scanner. For example, in constant force mode the AFM scanner moves the cantilever to match the surface topography in order to maintain a constant deflection signal. The x and y scanner control provides scanning trajectory inputs (u_x, u_y) to the AFM scanner. Data from the x , y , and z axes are compiled together to create an AFM image.

Imaging Modes

AFM imaging can be divided in two broad categories of contact/noncontact mode and dynamic/tapping mode. Contact and noncontact mode involve scanning a static cantilever over the surface to gather sample topographic information. In contact mode, a constant sample to probe force is maintained throughout the imaging process. This results in no cantilever displacement during the imaging process as shown in Fig. 2.7(a). The actuators for the cantilever (scan by probe) or sample (scan by sample) compensate for topographic changes in the sample's surface by changing the height of the cantilever or sample, respectively. The input signals to the actuators provide the image data for the sample. On the other hand, noncontact mode does not compensate for topographic changes in the samples surface and results in cantilever deflection changes as the sample is imaged. The changing deflection signal provides imaging data for this method as shown in Fig. 2.7(b). Dynamic AFM imaging involves exciting the imaging cantilever near its first resonant frequency, while scanning it across a sample's surface. Phase, amplitude, and frequency information can be extracted from the data for imaging as shown in Fig. 2.7(c).

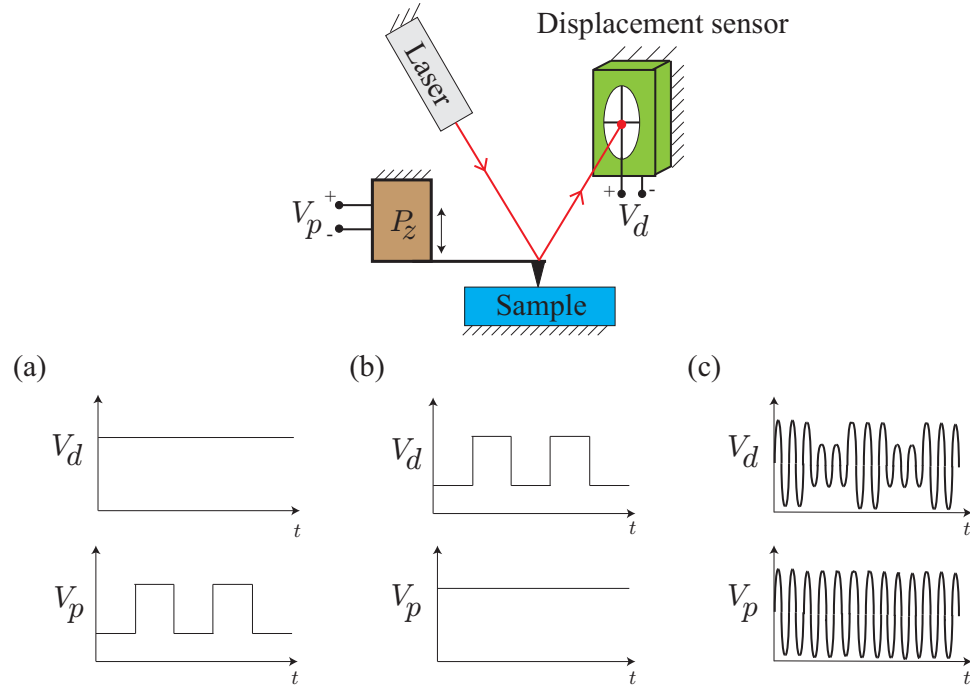


Figure 2.7: Three common AFM imaging modes: (a) contact mode, (b) noncontact mode, and (c) dynamic mode.

Piezoelectric Actuators

The AFM actuators used in the custom AFM utilize the piezoelectric effect for actuation. Piezoelectric actuators can also be physically strained or stress to generate a voltage. Charles Augustine de Coulomb first observed this phenomenon, but did not introduce the idea as piezoelectricity. Abbé Rene Just Haüy and Antoine César Becquerel first attempted experimentation with this phenomenon, but it was unsuccessful. Later Pierre and Jacques Curie proved that electricity can be produced by applying pressure on inclined faced hemihedral crystals. The most common piezoelectric material used in piezoactuators is lead zirconate-titanate ($\text{Pb}[\text{ZrO}_3, \text{TiO}_3]$, PZT). In its most basic form, a single block actuator contains a piezoceramic material between two electrodes. The greater the distance between the electrode, the higher the actuator's capacitance along with higher actuation power requirements. To solve this

problem, plate-stacked actuators use several smaller block actuators that are stacked on top of each other and wired in parallel; however increased manufacturing costs and tensile load limitations are present. Other actuator options include ring-stack, sectored tube, and bimorph piezoactuators. Piezoelectric tube scanners are a popular choice for x , y , and z scanner translations in AFMs. There following reasons are advantages for using a tube scanner for AFM scanning: a single, multi-sectored, piezoelectric tube provides x , y , and z translations, it greatly reduces system complexity by reducing the need for additional translational mechanisms and supports, helps reduce scanning head mass by reducing the number of parts attached to the scanner, and allows for laser beam steering by mounting a focusing lens at the end of the tube. Some downfalls of using a tube scanner includes: strong cross-coupling effects since all three axes of the actuator are physically constrained together, tube scanners are usually thin and very fragile, and the length of tube will be far greater than a stack piezo actuator for similar displacement. This causes the scanner’s moving mass to be distributed further away from the constrained end resulting in a larger moment at the probe end and introducing unwanted dynamics to the scanner.

The piezoelectric actuators utilized in the custom AFM design (nanopositioning stage) are Noliac SCMAP07 stack piezoelectric actuators in 8 mm and 12 mm length configurations. Further specifications are found in Table 2.1. Measured capacitance values are 501 nF, 493 nF, and 302 nF for the x , y , and z capacitances, respectively.

Table 2.1: Specifications for Noliac SCMAP07 actuators used in the custom AFM scanner.

Stage axis	Width (mm)	Thickness (mm)	Length (mm)	Actuation (μm)	Capacitance (nF)
x	5	5	12	14.7	480
y	5	5	12	14.7	480
z	5	5	8	14.7	280

Commercial and Custom AFMs

This section provides information on custom and commercial AFMs to provide a quick look at how the various components of an AFM have been modified for improved operation. AFMs has been central to various research application areas as well as education applications [55,56]. Custom built AFMs have been noted to utilize various novel techniques and components, such as rapid prototyping the AFM housing [57], using 12-electrode piezoelectric tube scanner [58], having a battery powered AFM [59], and incorporating a self-aligning cantilever positioning system using a DVD pickup head [60]. This demonstrates how the wide variety of researches have adapted AFMs in various ways to meet their own specific needs.

An area of interest in the custom AFM's design is how to adapt a traditional AFM design to incorporate a two axis serial-kinematic nanopositioner [50] as the sole actuation platform for AFM probe translation. The nanopositioner is chosen for its low cross-coupling effects in open loop control and low frequency dynamics. One issue that is addressed in the custom AFM is the optical system beam trajectory, which in our case has significant geometric constraints. Several system optical system designs have been used in the past, such as stationary optical systems, translating lenses and mirrors, movable photodetectors, and some AFMs that move the entire optical system while scanning. For example, a mirror [14] or lens [15,16] has been used to redirect the laser beam during scanning operation by attaching it to the scanning mechanism, so that the beam spot maintains a fixed position on the cantilever. This allows an increase in the scan range of the AFM, while reducing image artifact caused by uneven laser deflection and light scattering. Our design implements a scanning laser focusing lens to maintain a fixed laser point on the cantilever while scanning. This method has been shown experimentally to increase the scanning range over a fixed laser optical system [17]. A commercially available AFM is shown in Fig. 2.8.



Figure 2.8: Nanosurf’s easyScan commercial AFM system [1]. The photo shown here is borrowed from the citation.

The easyScan AFM package shown in Fig. 2.8 consists of a control box, scanning head, and sample platform. In Fig. 2.8, the control box is the large rectangular black box in the background. This control box contains the electronics and power for the AFM’s sensors, digital video cameras, laser, scanner actuators, and camera LED light. It also provides USB connection to the PC for control using Nanosurf’s AFM software. In addition, the control box allows external control and various output signal monitoring via a signal box. The scanning head is connected to the scanning head using a cable that transmits power to the AFM scanner as well as data to the control box. The scanning head rests on top of the sample platform. A silver disk which sits on top of the sample platform and acts as the sample tray for the substrates that are to be imaged.

AFM Probes

AFM probes are the only consumable of AFM imaging, yet have the greatest impact on image quality. Since the first introduction of AFM probe, two geometric configurations have become prominent in AFM probe layout. The first configuration is a triangular layout that is hollow in the middle resulting in two angle beams intersecting at the distal end with a tip attached at the intersection as shown in Fig. 2.9(a)

and 2.9(b). The triangular layout results in a stiffer AFM probe compared to the cantilever beam due to the two separate beams that compound their individual stiffness. However due to the angled beam's geometry and increased cross-sectional area interface between the probe and the base substrate, the lateral stiffness is greater than the cantilever beam. A high lateral stiffness is desirable because out of plane motion is not recorded in traditional contact mode AFM imaging. Triangular probe dimensions usually vary between $115\ \mu\text{m}$ and $193\ \mu\text{m}$ for length, while thickness is around $0.6\ \mu\text{m}$ with a tip radius range from $20\ \text{nm}$ to $50\ \text{nm}$. Triangular probes are commonly composed of silicon nitride, which are less expensive than other materials, but are very durable and well suited to many imaging environments [61]. On the other hand, the stiffer triangular AFM probes are not well suited for low force applications, where a softer AFM probe is desired such as the cantilever beam probe (*i.e.*, constant height contact mode imaging).

The cantilever beam probe is a probe that has a cantilever beam with a tip attached on the distal end as seen in Fig. 2.9(c) and 2.9(d).

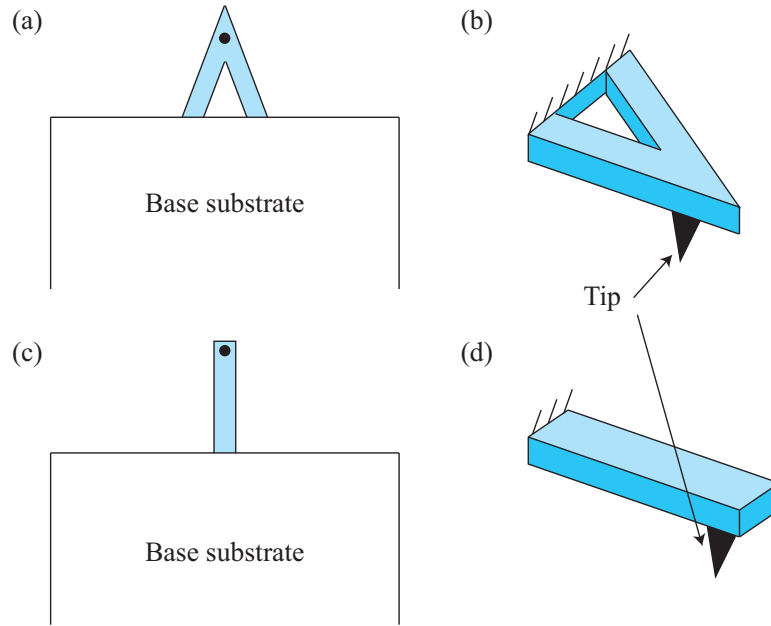


Figure 2.9: Two most common AFM probe layout configurations: (a) bottom view of triangular probe, (b) alternative view of triangular, (c) bottom view of cantilever probe, and (d) alternative view of cantilever probe

Cantilever beam probe dimensions vary according to their application. A soft contact mode probe is approximately $450 \mu\text{m}$ [length(l)] \times $50 \mu\text{m}$ [width(w)] \times $2 \mu\text{m}$ [thickness(t)] and a stiff dynamic (tapping) mode probe is approximately $125 \mu\text{m}$ [l] \times $30 \mu\text{m}$ [w] \times $4 \mu\text{m}$ [t]. In contrast to the triangular probes, the cantilever beam probes are made from single crystal silicon, which results in sharper tips with a tip radius under 10 nm [62]. This allows for imaging of smaller features since the tip radius is the limiting factor in image resolution. The base substrate for these probes are substantially larger than both the cantilever beam and tip (approximately 4 mm [l] \times 2 mm [w] \times 0.3 mm [t]). The cantilever probes have a rectangular cross-sectional area throughout, which allow for a traditional cantilever beam analysis. Furthermore, the significantly large base substrate effectively fixes the base of the cantilever while allowing the distal end with the tip be free. This justifies the clamped-free boundary condition in the cantilever beam analysis, which will be used later in Section 4.2.

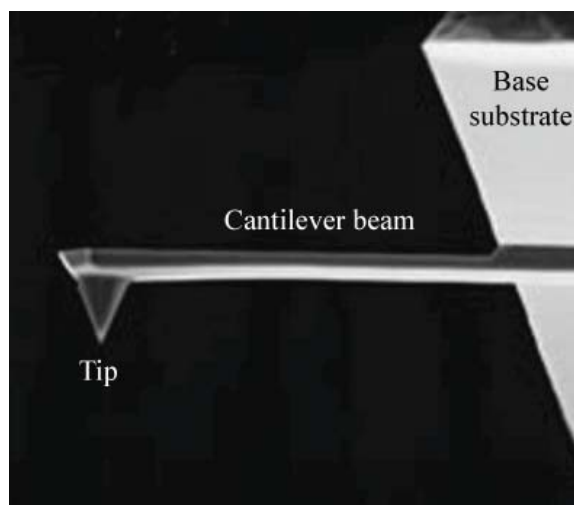


Figure 2.10: Scanning electron microscopy image of a typical atomic force microscopy probe with tip [2]. The photo shown here is borrowed from the citation.

A scanning electron microscope image of a typical AFM cantilever probe and tip is shown in Fig. 2.10.

2.1.3 Nanofabrication

AFM-based nanofabrication techniques are used to manipulate nanoparticles, perform direct mechanical surface modification, create lithography masks, chemically modify the sample surface, and perform dip-pen nanolithography (DPN). The AFM tip is used to manipulate nanoparticles by using two different methods. First by turning off feedback control system for the AFM probe, the probe applies a high load onto the nanoparticle residing on the surface of the sample, which results in displacing the nanoparticle. An alternative to turning off the probe's feedback controller is to adjust the tip to sample force setpoint during the probe's approach to the surface, such that when the probe makes contact with the particle, the particle is displaced [63–68]. It has also been noted that performing an AFM scan at a high setpoint can also displace the nanoparticles [69–71].

Direct surface modification or force lithography is accomplished using a stiff AFM probe and applying a 1000 to 1500 nN load on a soft sample. It is shown that the AFM probe creates surface wearing features on soft materials [72–77]. On hard surfaces, patterns are fabricated on a sacrificial layer using the AFM probe and then selective etching followed by removal of the sacrificial layer [78–85]. Applying force lithography on self-assembled monolayers (SAMs) results in a technique called nanografting, where molecules are coated in a solution [86]. Nanopen reader and writer operates on the same principal as nanografting, but instead of operating in a solution, this method can operate in air by coating the tip [87]. Nanografting and nanopen reader and writer create nanostructures out of biomolecules [88–93].

Another application area is presented by Mirkin et al. [39], where the AFM probe tip is coated with a thin film of a chemical. The coated AFM tip acts as a pen and the chemical is deposited onto a surface. This method is called dip-pen nanolithography (DPN) and can be combined with wet chemical etching to fabricate three-dimensional multilayered nanostructures [94,95]. The above methods have also been implemented into an automated system integration approach, namely computer-aided design.

Computer-aided design (CAD) is widely adopted throughout various disciplines for its intuitive interface and powerful design capabilities. Fabrication models are stored in a convenient file format that can be converted for various applications, such as generating g-code for computer numeric control (CNC) processes. Recently, design software and techniques have been moved from the macroscale to the nanoscale resulting in several applications that range from assembly of nanostructures [96] to formation of silicon oxide patterns for nanolithography [97]. CAD’s graphical user interface appeals to many areas, in particular the nanolithography community, where several applications to nanofabrication processes are found. Another powerful quality of CAD is in the data output file itself. The output file can be readily converted to a

script file and loaded onto a commercial AFM for patterning [98]. Furthermore, the data has been shown to be advantageous as an interface language for an AFM, where distance measurements are made using a priori knowledge [99]. Other work includes creating a custom CAD interface to implement designed models onto a commercial AFM; however, this approach utilizes expensive, proprietary hardware [100].

The above examples show how individual tips can be used for various applications, but after one process is completed the current tip needs to be switched out for another. This tip interchanging process can be time consuming for a multi-process fabrication procedure and this issue of throughput is addressed in this work.

2.2 ETM Actuators

Thermal actuators allow for a relatively small actuator footprint ($240 \mu\text{m} \times 12 \mu\text{m} \times 2 \mu\text{m}$) while still being able to achieve deflections around $50 \mu\text{m}$ using input voltages close to integrated circuits [101]. This is a great benefit for applications where electrically sensitive devices (*i.e.*, AFMs) are utilized. The thermal actuator in its simplest design is composed of a single homogenous material throughout that produces an actuation deflection due to an varying thermal expansions within the actuator using an electrical input. Current flows through the thermal actuator by following a path, where the cross-sectional area changes throughout the arm as is shown in Fig. 2.11(b). One section of the arm has a smaller cross-sectional area than the other arm. The smaller cross-sectional arm is called the hot arm and the larger cross-sectional area arm is called the cold arm. The hot arm heats up to a greater degree than the cold arm by the joule heating effect, which then leads to a greater thermal expansion in the hot arm. The thermal expansion mismatch between the hot and cold arm provides an actuation motion from the hot arm towards to cold arm as is depicted in Fig. 2.11(a) and this deflection is notated as δ .

The thermal actuator's small size and single material composition make it attractive for micro assembly applications, such as in [102]. Narrow tips have been grown on the actuator arm by focusing an electron beam at the end of the actuator [103] to create a smaller gripper mechanism. Other variations on the single actuator arm have been utilized in different actuator arrangements, such as connecting them serially as in [104] utilizing various connection techniques and orientations. A simple single serial connection between two actuators is shown in Fig. 2.11(c). Other groups have these serially connected multiple actuator arms integrated into a single larger actuator [3, 18, 105], so that the same force and displacement amplification can be accomplished as with the serially connected actuators. In other cases, all of the thermal arms are not actuated, but used rather as a resistive feedback sensor by utilizing a wheatstone bridge [106]. Furthermore, some groups have utilized topology

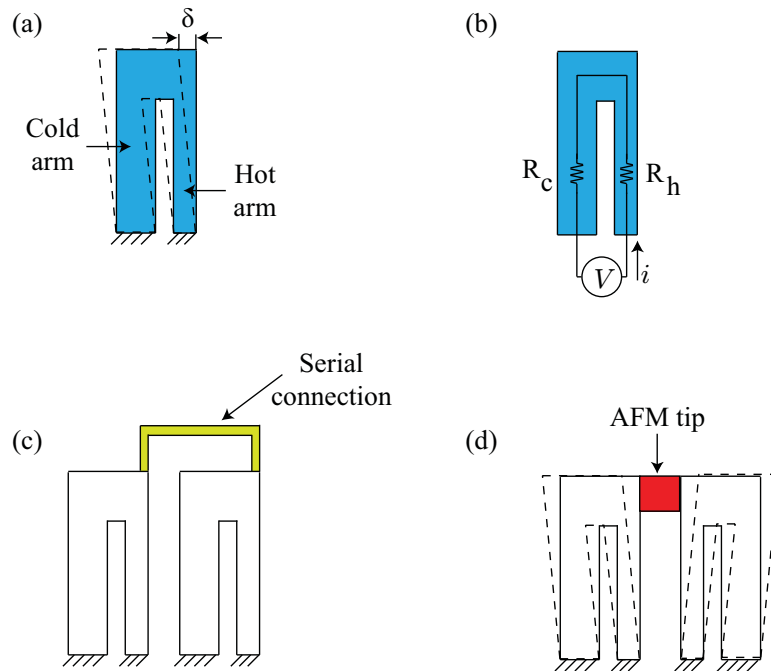


Figure 2.11: ETM actuation and displacement concept with applications: (a) actuation displacement, (b) resistive heating concept, (c) force multiplication application, and (d) AFM multifunctional probe application.

optimization program to create optimized structures for their homogenous thermal actuators [4, 107].

So far only single, homogenous thermal actuators have been discussed, but other groups have used multiple materials in their actuators. These actuators use two or more different materials, where one arm has a much greater thermal expansion coefficient than the others, thus resulting in a bending motion due to the mismatch in thermal expansion [108, 109]. Yet another variation utilizes a heater layer that provides the temperature rise for another material with a higher coefficient of thermal expansion [110, 111].

Other researchers have created ETM actuators for object pick and place with the

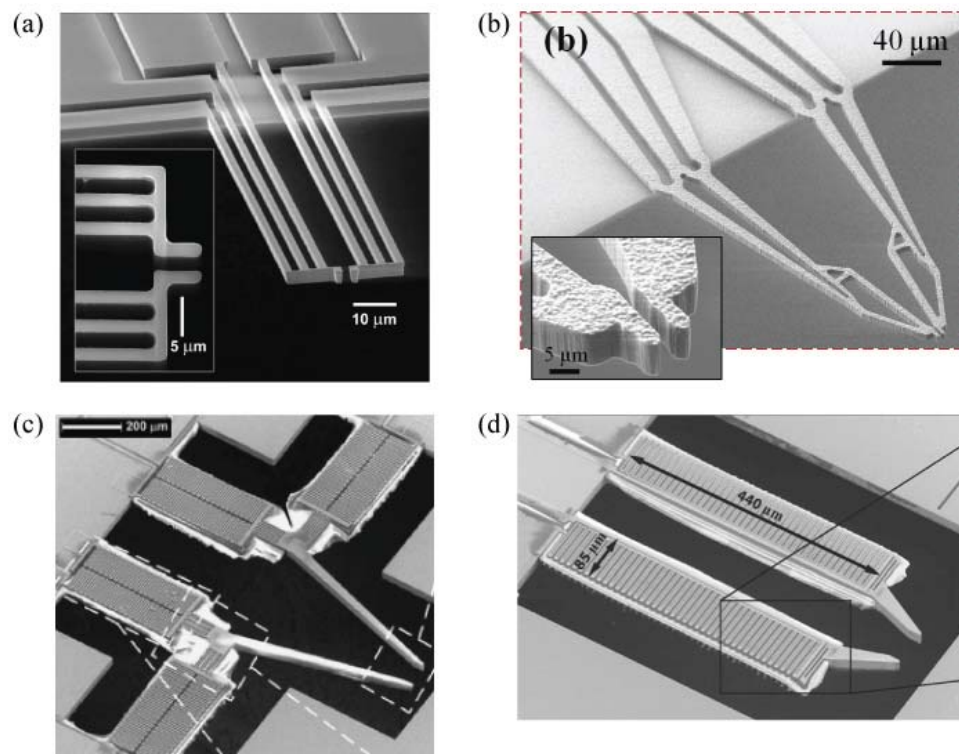


Figure 2.12: ETM actuators: (a) [3] and (b) [4] are composed only of silicon and utilizes varying cross-sectional areas for actuation, while (c) [5] and (d) [6] are composed of silicon and SU8 where the material property mismatch is exploited for actuation. The photos shown here are borrowed from the citations.

main distinction between them is their material composition. The first type only uses silicon as the actuator composition and utilizes either several actuators (Fig. 2.12(a)) or varying cross-sectional area (Fig. 2.12(b)) for their thermal expansion mismatch between the hot and cold arms for actuation displacement. Other researchers have relied on using two separate materials for the thermal expansions mismatch. The design presented in Fig. 2.12(c) has four separate actuators to control the opening and closing of the actuator ends, while Fig. 2.12(d) presents a design that only uses one actuator per actuator end.

The design presented here incorporates a compression-based gripper composed only of silicon, where an electric current is applied to the microgripper to open the gripper's jaws. A tip is inserted into the open jaw and the electrical current is removed to close the jaw onto the tip, which compresses and holds the tip. A depiction of this actuation along with thermal actuator arrangement for gripping applications is shown in Fig. 2.11(d). By using simple compression mechanics in our design, the tips can be changed rapidly with little downtime, which results in greater throughput for various applications. Our design will utilize the simplest ETM actuator layout, by fabricating the actuator out of a single material (silicon) and only using the cross-sectional area difference for the thermal expansion mismatch in the hot and cold arms, which results in the actuator's displacement.

2.3 Summary

This background section has provided an overview of the concept, previous work, and shortcomings of AFM and likewise for ETM actuators. It is shown that while the AFM is powerful tool for nano-scale applications, its future is greatly limited by its throughput. To solve this problem, ETM actuators are posed as the mechanism for AFM tip changes that will streamline the probe changing and calibration

process. ETM actuators operate with low power input, which is desirable when operating near sensitive AFM equipment. In contrast to previous work completed by other researchers, the ETM multifunctional probe designed in this document will be specifically tailored for an AFM probe application. This thesis will provide design, fabrication, and characterization of a custom AFM as well as the design, model, analysis, and characterization of an ETM-based multifunctional probe. This thesis also demonstrates the implementation of an ETM actuator within the custom AFM system that is able to pick and place an object to facilitate an autonomous tip changing AFM system.

Chapter 3

AFM Design, Fabrication, and Characterization

A custom AFM is designed and fabricated to provide both a characterization platform as well as an implementation platform for the multifunctional probe. The need for a custom AFM is facilitated from the lack of flexibility in current AFM systems where many components are fixed and not able to be adjusted for this custom application. The key idea behind the custom design is to keep components adjustable within reason, while still keeping the design transparent enough for any future modifications. A key component to keep highly flexible is the displacement measurement system, where different probe dimensions and reflective coatings can affect the system's performance. Special considerations are given to laser spot adjustments and photodetector circuitry. A simplified block diagram of the custom AFM system is presented in Fig. 3.1. The goal of this design is to have a platform that translates a probe holder in three axes, while recording probe displacement via photodetector sensor to both manipulate objects as well as image a sample's surface.

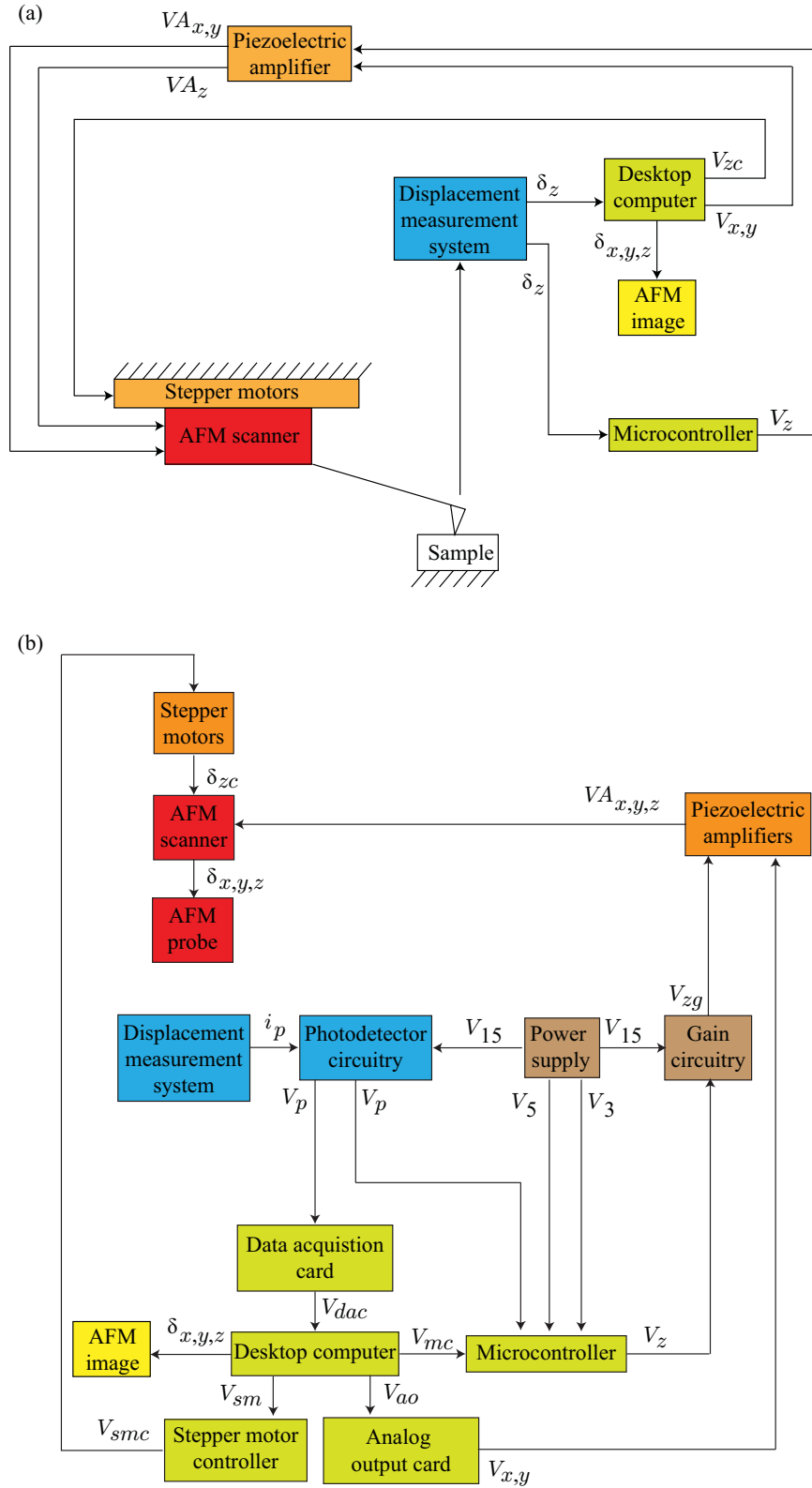


Figure 3.1: Block diagram of the custom AFM system's major components: (a) simplified functional block diagram and (b) complete AFM signal block diagram.

Figure 3.1 separates the the design into five functional categories. The first category is probe's displacement measurement system, which include the displacement measurement system and the photodetector circuitry. This category provides sample height information using the AFM probe's displacement change caused by tip-sample interaction. The displacement measurement system generates a current (i_p) based on the probe's displacement and sends it to the photodetector circuitry that converts the current into a voltage signal (V_p).

The displacement information (V_p) is sent to the second category in the figure, which contains the data acquisition system and the microcontroller. The data acquisition card contains analog to digital converters, which converts the photodetector circuitry's signal (V_p) to a discrete digital signal (V_{dac}) for microcontroller tasks. The data acquisition card is housed inside of a desktop computer, which contains software to control the stepper motor controller (V_{sm}) and the x, y AFM scanning trajectory (V_{ao}). The desktop computer also loads settings into the microcontroller (V_{mc}), which performs closed-loop control during AFM imaging. The stepper motor controller is used as the AFM approach and withdraw mechanism for the AFM probe by sending the proper input signals (V_{smc}) to the stepper motors.

The third category provides the necessary interface to the AFM scanner and contains the piezoelectric amplifiers and the stepper motors. The stepper motors lowers and raises the entire AFM scanner platform for sample removal and sample tilt correction (δ_{zc}). The piezoelectric amplifiers provide the high voltage ($V_{x,y,z}$) required to actuate the piezoelectric actuators within AFM scanner. The fourth category contains the AFM scanner and probe holder, which are the only moving parts during AFM operation. The AFM scanner provides the scanning trajectory via a two axis (x and y) nanopositioner with a custom z -axis actuator ($\delta_{x,y,z}$). The fifth and last category are the supporting power and voltage references for the custom circuitry (V_{15} ,

V_5 , and V_3) and the microcontroller interfacing circuitry (V_z) to the piezoelectric amplifier (V_{zg}). This concludes the general description of the major AFM components and the next section will discuss the design of a commercial AFM design to lay the foundation for the custom AFM design.

3.1 Mechanical Design

To gain familiarity with commercial AFM design, reverse engineering is used on a easyScan AFM is to gain insight into system configuration and fabrication practices.

After removing the front cover, the AFM can be immediately separated into two

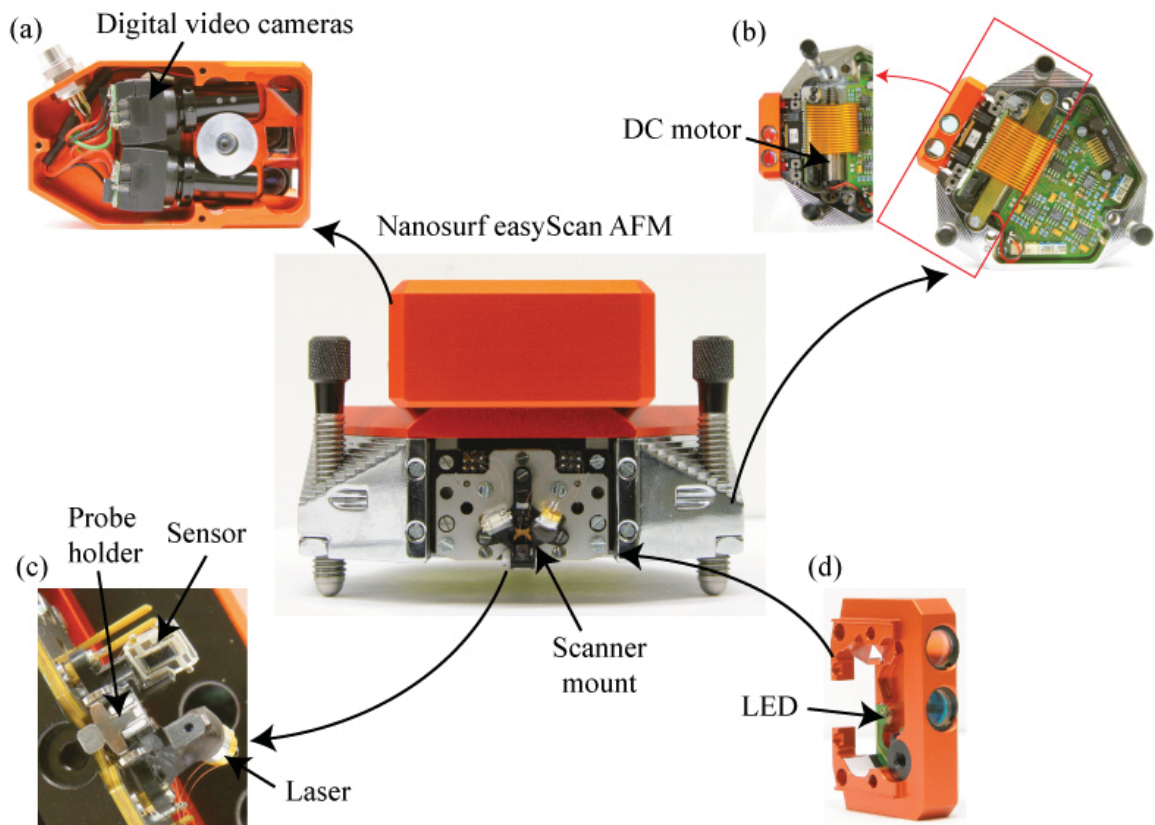


Figure 3.2: Reverse engineering a commercial AFM system into its various components: (a) video system, (b) AFM base, (c) scanning head, and (d) scanning head cover.

compartments (top and bottom). The top compartment houses the digital video camera that provides live video of the AFM probe and is seen in Fig. 3.2(a). This helps with the manual approach to the surface and also provides verification of successful probe withdrawal before moving the sample. The cameras utilize reflective mirrors to direct the camera's aperture to the probe below. One camera provides an overhead view of the probe, while the other camera has an isometric view of the AFM probe.

The bottom compartment (AFM base) contains the scanning head with all supporting circuitry as well as the coarse approach. The bottom compartment is a single metal house base that can be translated using three thumb screws attached to the outside base and is shown in Fig. 3.2(b). Within the base, a dc motor is attached to worm gear drive system, which translates the scanning head vertically during sample approach. Figure 3.2(c) shows the laser, AFM probe holder, and displacement sensor where they are all fixed together using a single backing plate.

The fixed optical systems demonstrates why special alignment marks on the AFM probes are needed, since the fixed system does not allow a user to adjust the optical displacement system components. The flexibility needed for custom AFM applications where various probe sizes needs an adjustable optical system is not available in this AFM. The probe holder is simply a lever-spring apparatus that applies uniform pressure over the AFM probe base. This also limits the probe's application by restricting electrical connections to the probe either at the distal end or through the center of the probe. To install an AFM probe, the spring is compressed and the probe is placed underneath a metal clip. After the probe is installed, the spring is released and provides the clamping force to securely hold the AFM probe. In Fig. 3.2(d), the scanning head cover provides three functions to the AFM system. The first function is to provide protection of the delicate wires to the optical displacement system. The second function is provide a mounting structure for mirrors and lenses for the video

camera system. Lastly, the cover houses an LED light for illumination of the AFM probe when the video camera system is in use. This disassembly process reaffirms the block diagram created earlier and provides verification of the design approach utilized in this section.

3.1.1 AFM Approach Mechanism

The easyScan AFM utilizes a DC motor connected to a worm gear system for its coarse system approach; however with its coarse gearing and analog input driving signal to the motor, repeatability and resolution suffers as a result. To increase the precision of the custom AFM, a stepper motor is implemented into the design. Stepper motors operate with a input pulse that moves the shaft a discrete amount per pulse. This gives the motor excellent starting, stopping, and reversing response because the motor has full torque at standstill. The speed of the motor is proportional to the frequency of the input pulses and the motor has non-cumulative error from one step to another.

In particular, a Thorlab model: DRV001 actuator provides translational movement using a stepper motor and provides up to 8 mm of travel, while maintaining a 26 nm resolution and at least 8 μm repeatability. The stepper motor is connected to a high precision screw inside the DRV001 motor housing that translates the rotational movement of a stepper motor shaft into a translational one. This provides the vertical travel used to lift and lower the AFM base platform. Each actuator can support up to 48 lbs, so this is the only limiting factor in the AFM's weight. The motor orientation is shown in Fig. 3.3, where each motor is mounted vertically. The approach mechanism incorporates three actuators arranged in a triangular pattern, such that the AFM stage can be translated in all three axes. The AFM base layout with stepper motor configurations and geometric measurements is located in Fig. 3.4.

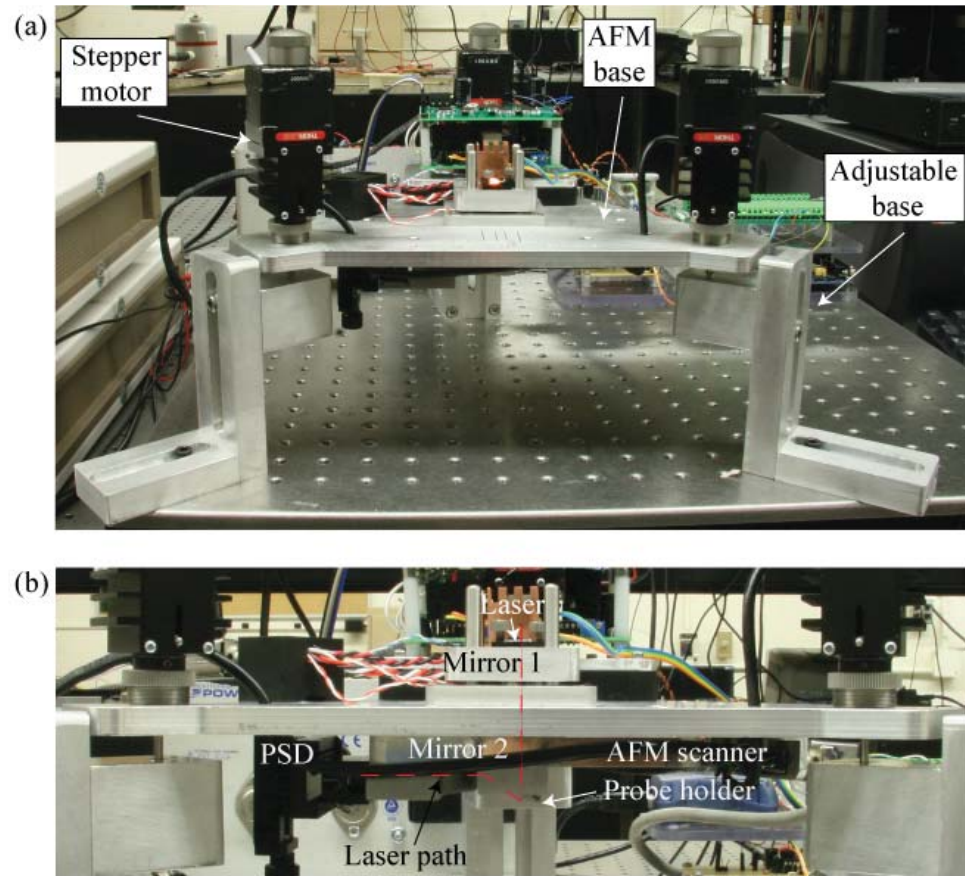


Figure 3.3: The (a) block diagram of stepper motor's implementation and contribution to vertical displacement along with the arrangement of components attached to top of AFM base platform: (b) stepper motor orientation and (c) laser trajectory.

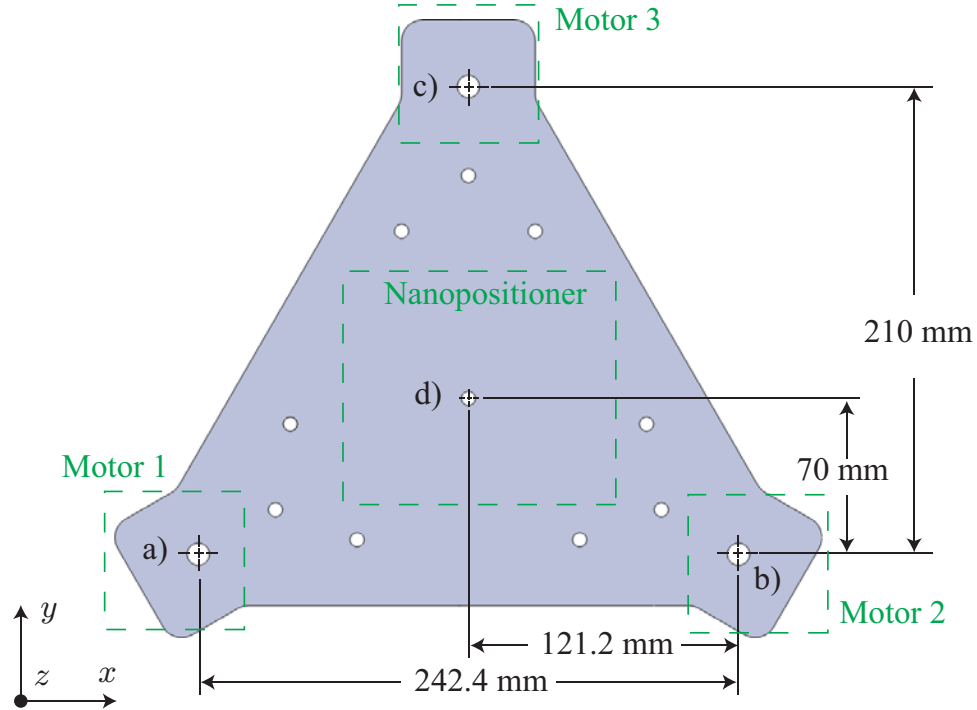


Figure 3.4: Top view of AFM base platform with stepper motor placement measurements at the following locations: (a) motor 1, (b) motor 2, (c) motor 3, and (d) center.

Knowing the distance between the stepper motors and the center of the AFM, translation of any one motor by $1 \mu\text{m}$ in the z -axis in either direction will result in a $0.33 \mu\text{m}$ translation at the center of the AFM in the same direction of actuation. In addition to the vertical translation, the AFM center also displaces approximately 1.587 pm along the center line from motor center to the AFM center resulting in a 2.7×10^{-4} degree of inclination. This results in a 1.374 pm translation along the x -axis and a 0.794 pm translation along the y -axis. The result is negligible for small actuation change between the motors; however this effect is compounded as height variations increase between motors and can become a source for error in x, y positioning. The largest error is seen by actuating motor 1 to its full actuation state, while keeping motors 2 and 3 at zero actuation (or any variation of this). This scenario results in a 2.18 degree of inclination of the AFM base platform as well as a $101.6 \mu\text{m}$ translation

along the center line from the motor's center to the AFM center. This leads to a $88.0 \mu\text{m}$ displacement in the x -axis and a $50.8 \mu\text{m}$ in the y -axis. Both of these values are large enough to impact AFM scanning position if care is not taken to compensate for this when actuating the motors. For example, when leveling out a sample surface the motors are actuated and their displacements are varied to tilt the AFM scanner into a plane parallel to the sample's surface plane. While performing this operation, the desired feature location can change due to the translation of the center point. The location can vary more than the scanning range of the AFM scanner (approximately $40 \mu\text{m}$ for x and y).

The motors are interfaced with a National Instruments model: MID-7604 power drive hardware. This hardware provides power to each motor and is interfaced with LabVIEW software using a National Instruments model: PCI-7340 motion control card.

3.1.2 AFM Scanner Mechanism

The AFM scanning head utilizes a two-axis serial-kinematic nanopositioner [50] with a custom z -axis probe holder. The probe holder houses a $5 \text{ mm} \times 5 \text{ mm} \times 8 \text{ mm}$ piezoelectric stack actuator and provides over $7 \mu\text{m}$ of displacement for z -axis control. The nanopositioner utilizes two $5 \text{ mm} \times 5 \text{ mm} \times 12 \text{ mm}$ piezoelectric stack actuators with a displacement multiplying fulcrum design that achieves over $40 \mu\text{m}$ of displacement for x -axis and y -axis translation. Figure 3.5 provides a depiction of the nanopositioner with actuator orientation information.

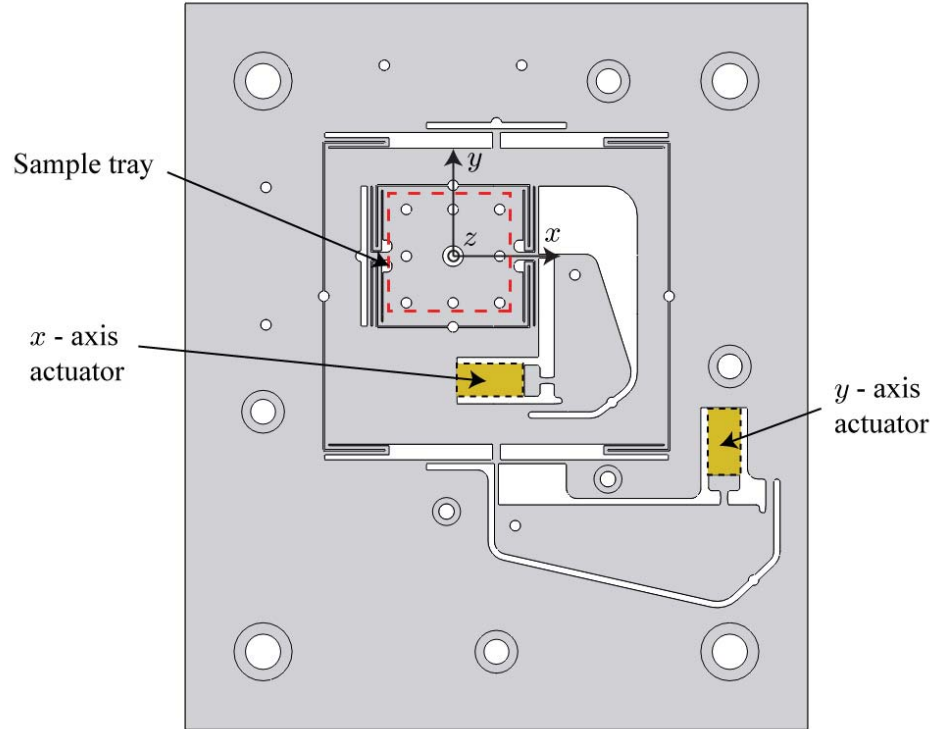


Figure 3.5: Coordinate system for nanopositioner with piezoactuator orientations.

The y -axis translates the inner platform that houses both the x -axis actuator as well as the sample tray, while the x -axis actuator only translates the sample tray. It can be noted that the y -axis actuator has a greater mass to move than the x -axis actuator and will thusly have a lower resonant frequency. This is intentional in the design of the nanopositioner, since a traditional AFM raster scan imaging trajectory incorporates a slow (y -axis) and a fast (x -axis) scanning axis. The sample tray is the platform that is translated both in the x -axis and y -axis by the actuators and serves as the location where the custom z -axis probe holder is mounted.

3.1.3 AFM Probe Displacement Measurement System

The custom AFM design presented measures the deflection of a laser beam off the cantilever's tip using a photodetector. Due to geometric restraints, the deflected

laser beam is redirected using a mirror before reaching the photodetector. The layout of the nanopositioner poses challenges to utilizing laser beam deflection sensing for cantilever displacement. First the laser had to be mounted at least 38 mm from the cantilever's surface due to the thickness of the nanopositioner and its mounting hardware. Next, to reduce the moving mass on the nanopositioner's traversing stage, the laser was fixed to the AFM's large stationary base plate. By fixing the laser's location, normally this would cause the laser beam to move off of the cantilever during scanning resulting in a degradation of the signal to the photodetector. This issue is solved by incorporating a movable focusing lens between the laser and the cantilever. The lens is attached to the top of the nanopositioner by recessing the lens inside an aluminum block that is mounted to the nanopositioner's traversing stage. This lens provides focusing and beam steering abilities to an otherwise dispersed and stationary laser beam.

Another challenge to overcome is the routing of the reflected laser from the tip of the cantilever to the photodiode sensor. Space requirements allowed only two options. The first option was to drill a hole through the nanopositioner and AFM base plate to allow for the reflected laser beam to be sensed by a photodiode that will be mounted on the top of the AFM base plate. However, this would require disrupting the dynamics of the nanopositioner by drilling and removing material from movable stage and possibly the flexures. Also, the distance between the cantilever and suitable mounting location on top of the AFM is so large that the deflected laser beam could be so dispersed when it reaches the photodetector that cantilever deflection might not be measurable. The second option is to mount a mirror to reflect the laser beam off to the side of the nanopositioning stage, where a photodetector sensor can be mounted. This is our most feasible alternative, but can potentially introduce undesirable noise and errors into our cantilever displacement measurements from poor mirror selection

or mounting.

The first issue to resolve was the mirror properties itself. Critical mirror specifications for our application include mirror thickness and surface accuracy. The mirror thickness constrains the geometric layout of the mirror holder and a thinner mirror is desired. The surface accuracy of a mirror is a measure of the flatness of the mirror's surface. Surface accuracy is expressed in terms of wavelength of the light per inch and determines how much error is introduced into a reflected beam's trajectory. For our application, mirror thickness is limited to 2 mm and the best surface accuracy was chosen from commercially available mirrors. The chosen mirror has a surface accuracy of $1/10\lambda \text{ in}^{-1}$, which results in a 14 nm maximum error across the 5-mm diameter mirror and a maximum optical path error at the photodetector of 28 nm for a red laser light. The second issue is how to mount the mirror underneath the nanopositioner in such a way that would deflect the laser beam horizontally to the photodetector. Due to geometric restraints, a mirror was placed on the end of a cantilever beam style mount as seen in Fig. 3.6.

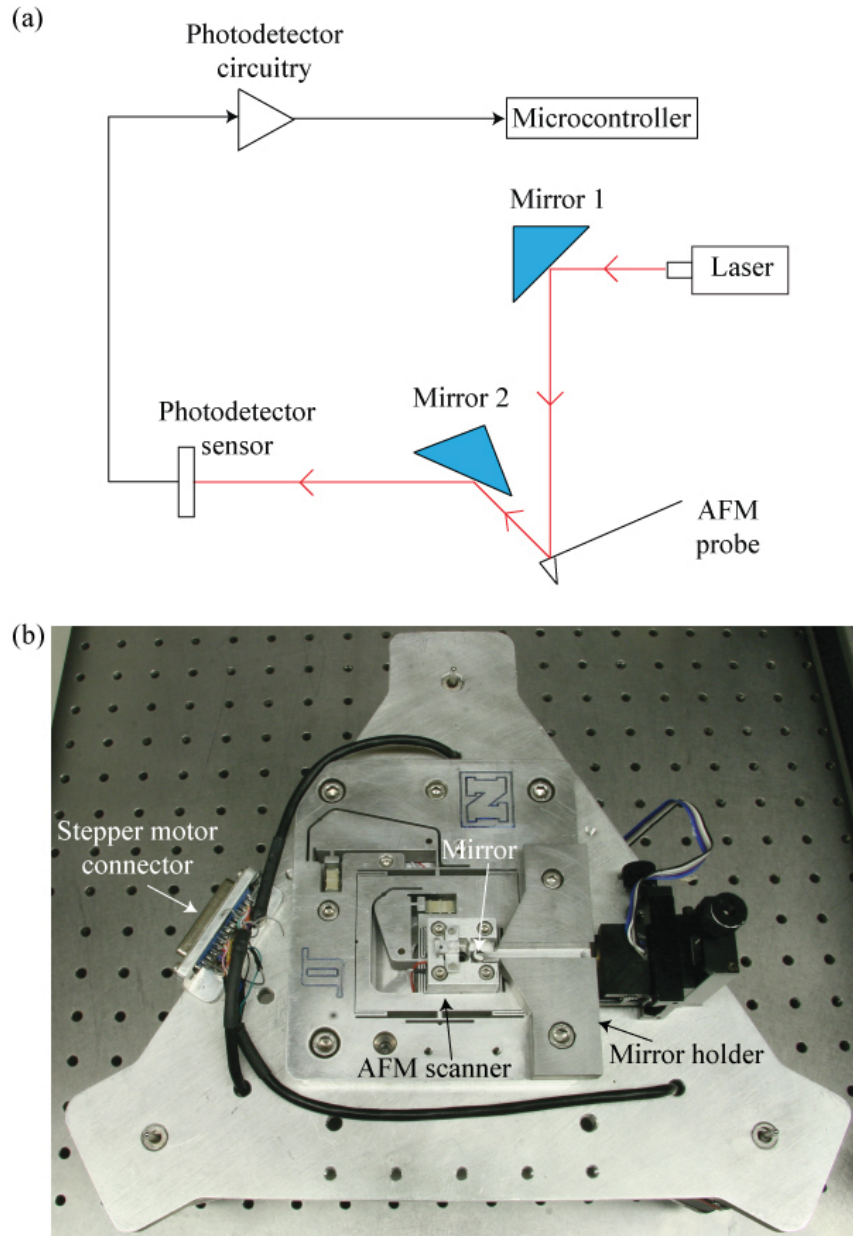


Figure 3.6: The (a) laser's trajectory and the (b) layout of mirror holder and AFM optics.

In order to increase the frequency of the first mode for the mirror holder, the mount is kept as short as possible while trying to reduce end mass. Existing mounting holes are used to secure the mirror holder to the nanopositioner. Thickness of the mirror holder mount is dictated by the distance from the AFM base plate to the cantilever

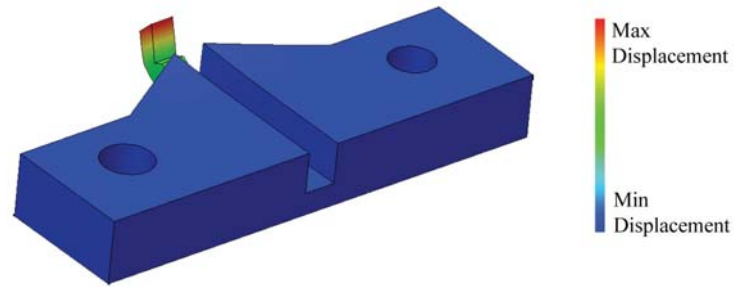


Figure 3.7: Mirror holder FEA frequency response analysis depicting the first mode shape at 19.2 kHz.

tip, such that the mirror holder will not protrude lower than the cantilever tip and thusly not interfere with the sample. Figure 3.7 shows the first mode from a frequency response analysis using SolidWorks FEA software.

The material specified in this analysis is 1018 steel with approximate overall dimensions of 94.0 mm [w] \times 48.3 mm [l] \times 12.7 mm [t]. Additional material properties include: elastic modulus of 200 GPa, Poisson's ratio of 0.285, and density of 7865 kg/m³.

The AFM probe displacements are measured using a quadrant photodetector sensor (Pacific Silicon Sensor model: QP5.8-6-TO5). This sensor is chosen for its small active detector area, sealed TO package, and red laser light responsivity (0.4 A/W). The small detector area helps reduce noise by limiting the amount of dark current (0.4 nA) in the sensor because dark current is proportional to detector surface area. Dark current is the amount of current that flows from the sensor when there is no light on the sensor and is seen as a source of noise. The displacement sensor outputs a current proportional to the amount of light it receives. An illustration of a quadrant photodetector is shown in Fig. 3.8 for sensor configuration and equivalent circuit representation.

The active area in the chosen sensor is a 2.6-mm square with individual active areas

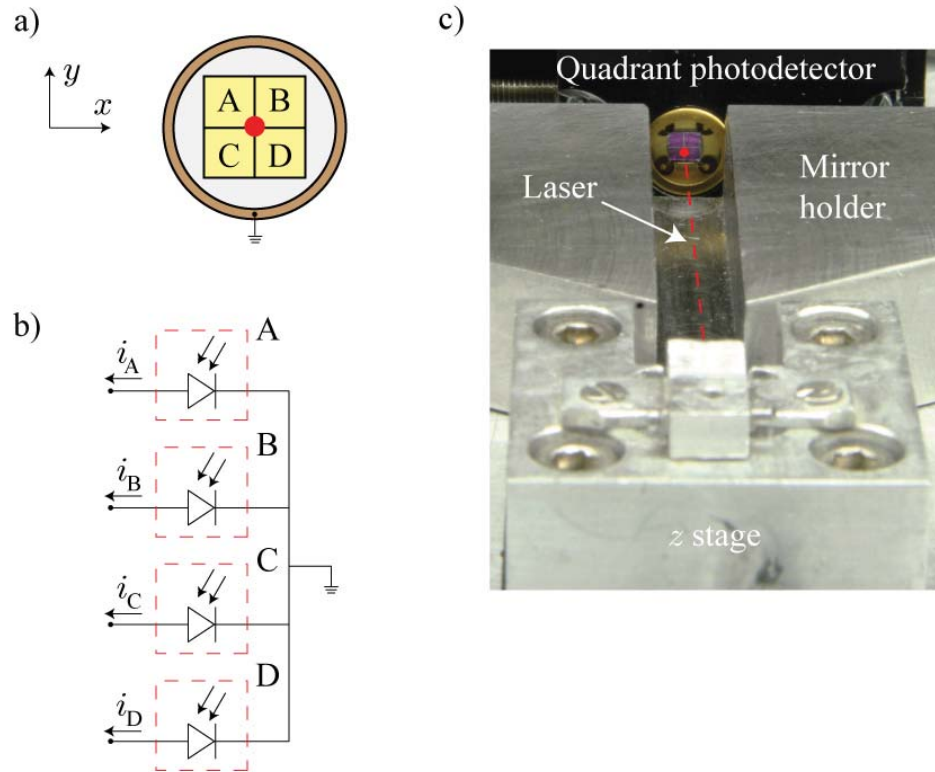


Figure 3.8: Quadrant photodetector sensor illustration of: (a) sensor configuration, (b) equivalent circuit representation, and (c) actual photodetector.

of $1.2 \text{ mm} \times 1.2 \text{ mm}$ (A, B, C, and D areas). Each quadrant region can be represented as a single light sensitive diode, where the amount of light exposure is proportional to the amount of current generated from the sensor as shown in Fig. 3.8(b). However, the peak current generated by the sensor is limited to 10 mA and in this application will be significantly less due to the light intensity loss as the laser beam is redirected off of the AFM probe as well as a mirror. For this reason, the photodetector circuitry utilizes high impedance resistors to increase the voltage output signal. This will be discussed in more detail in the following sections.

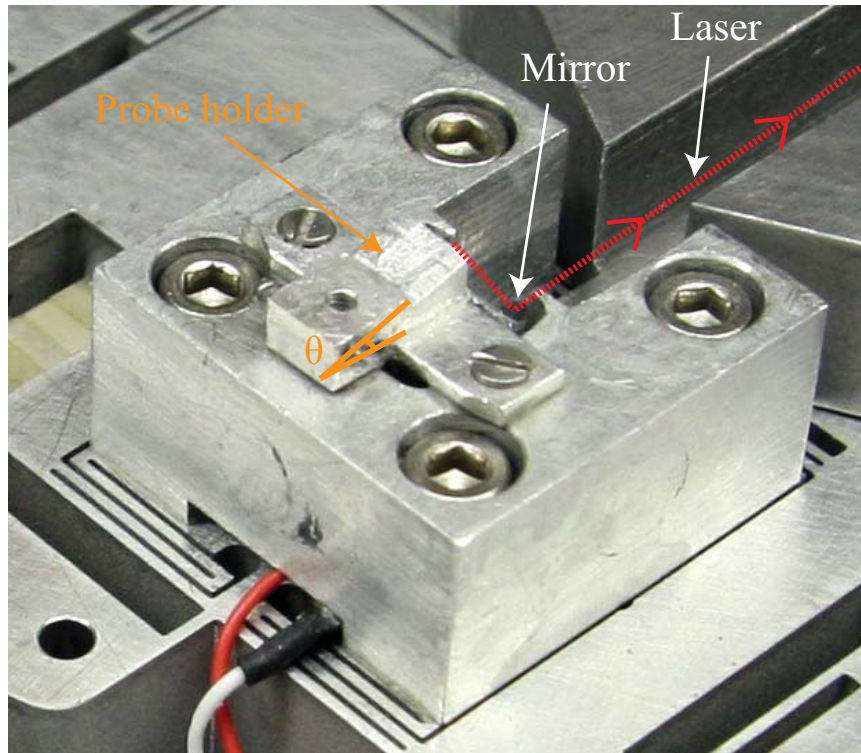
Table 3.1 presents more information on the AFM's optical system components.

Table 3.1: Summary of AFM optical system components.

Optical component	Retailer	Part No.
Scanner mirror	Edmund Optics	NT32-307
Mirror 2 (Fig. 3.6(a))	Edmund Optics	NT64-007
Optics cage rods	Thorlabs	ER6
Quadrant photodetector	Mouser Electronics	718-QP5.8-6-TO5

3.1.4 AFM Probe Holder

A custom AFM probe holder is needed for the design to provide a mounting platform for the multifunctional probe as well provide z -axis actuation for control. The fabricated AFM probe holder is shown in Fig. 3.9 for clarification on the design. Underneath the cantilever holder is a 5 mm \times 5 mm \times 8 mm piezoelectric stack actuator that provides z -axis translation of the AFM probe. The AFM probe holder

Figure 3.9: AFM probe holder with inclination angle identified (θ).

is machined to a 15° angle of inclination (θ) to redirect the laser beam off of the cantilever and into the AFM probe displacement sensor. AFMs typically use a 10° to 15° inclination angle for the cantilever chip and a 15° angle is chosen to provide enough clearance so the reflected laser beam can reach mirror.

3.2 Electrical Design

The goal for the AFM circuitry is to minimize noise from outside and within the circuit, while providing electrical signal interfacing between components of varying input voltage ranges. The electrical design emphasizes on using low noise, high bandwidth operational amplifiers along with surface mount components. The surface mount components required custom printed circuit boards (PCBs) to be designed and fabricated. By using custom circuit boards, large ground planes are utilized to reduce noise and help eliminate grounding issues found in prototype circuits using breadboards. Custom PCBs are created using ExpressPCB software and printed circuit board fabrication services. Also, important considerations are given to the operation speed and associated delay with each circuit component.

3.2.1 Power Circuitry

All custom circuitry is powered by a International Power model IHCC15-3 power supply, which is able to output ± 15 VDC at 3 A. Figure 3.10 shows the power supply with added voltage regulators and custom power terminals. This power supply allows for an integrated, stand-alone AFM system.



Figure 3.10: Power supply for AFM circuits and voltage references

The ± 15 V terminals supply power to operational amplifiers in the photodetector and gain circuitry. The +5 V terminal supplies power to the laser circuitry and uses a LM7805 voltage regulator to step down the +15 V to a +5 V signal. The LM7805 and LM317 are chosen for their high output current of 1 A and 1.5 A, respectively and their TO package, which makes prototyping off of the main power supply a less formidable task. The LM7805 has several output voltages, but are limited to values no less than 5 V, so an alternative voltage regulator is required for lower voltage. A LM317 is an adjustable voltage regulator able to output a voltages down to 1.2 V and is used for the +3 V reference for the microcontroller. The laser circuitry is powered with a +5 V source from the LM7805. This self-contained unit is created to increase system portability and create a stand-alone AFM system with dedicated equipment.

3.2.2 Photodetector and Gain Circuitry

The quadrant photodetector and its interface with the system is the most critical electrical circuit component of the system, since all surface measurements rely on it. All components in this circuit are surface mount components, which help in reducing circuit noise. The OPA4131UA operational amplifiers (op-amps) are selected for their low noise, low offset voltage, wide bandwidth, and compact package size (plastic small outline). The op-amps are used in the circuit design as buffers, adders, and subtractors. Circuit noise is also reduced using 1000 μF electrolytic capacitors close to the power source and 0.1 μF surface mount capacitors at each power trace to the op-amps ($\pm 15\text{ V}$). The capacitors help stabilize the supply voltages during large loads.

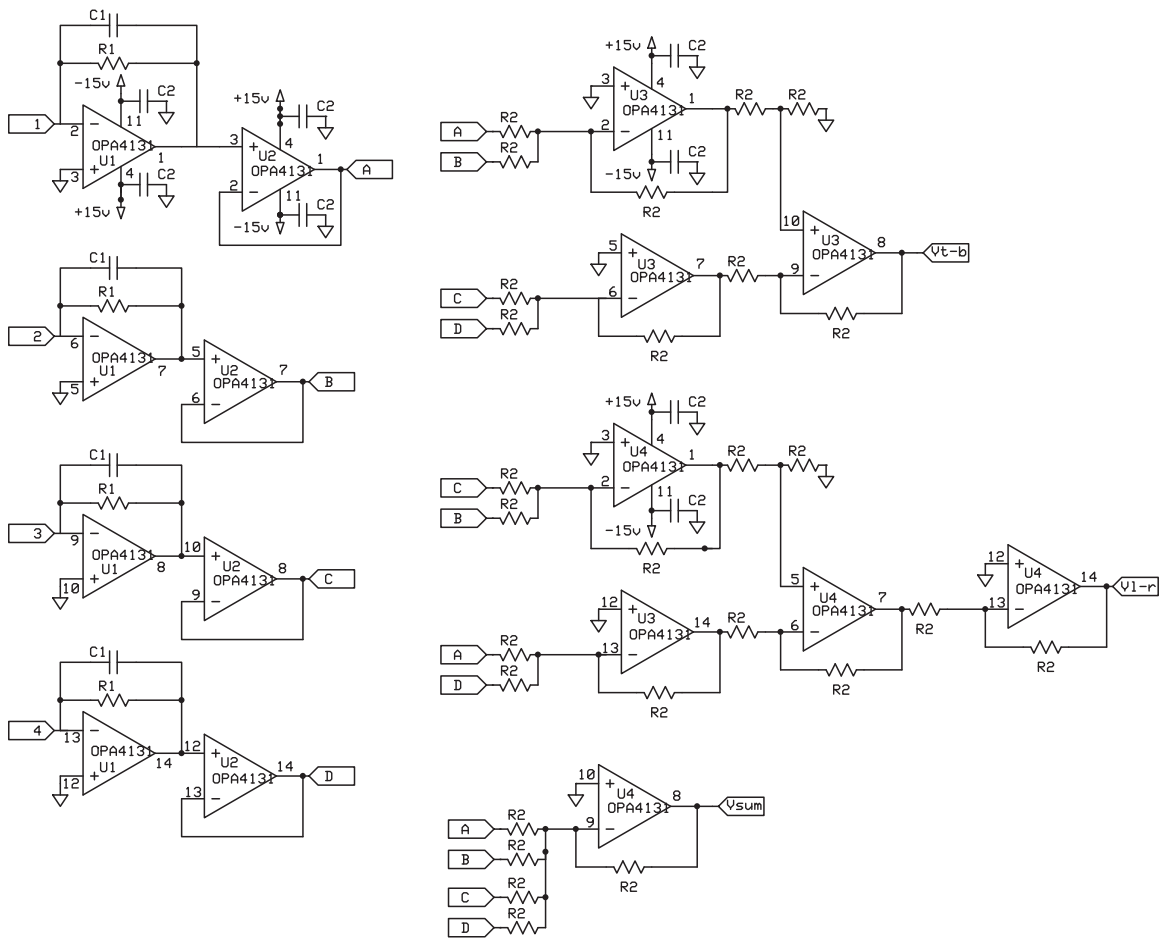


Figure 3.11: Circuit schematic of quadrant photodetector circuit where 1, 2, 3, and 4 represent the output from each quadrant of the photodetector.

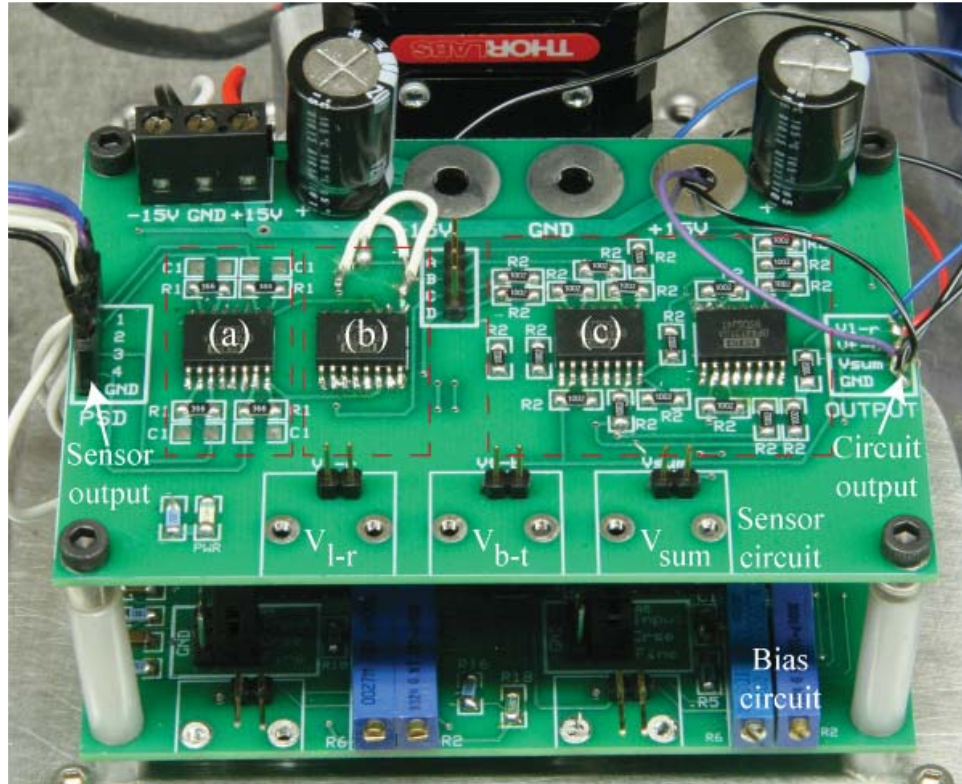


Figure 3.12: Quadrant photodetector sensor circuit that performs the following procedures: (a) converts current signal to voltage signal, (b) buffers the voltage signals, and (c) adds and subtracts voltage signals for AFM probe displacement data.

The photodetector circuit is broken into the following three main functions: (a) generate a voltage signal from the photodetector sensor, (b) buffer the signals, and (c) perform addition and subtraction to the various voltage signals for x and y laser spot locations. Section (a) of the circuit presented in Fig. 3.12 takes the current signal leaving the quadrant photodetector sensor and passes it across a $36\text{ M}\Omega$ resistor to generate a voltage potential signal. A high resistance value is used here because the twice reflected laser beam has low intensity by the time it reaches the sensor. Next in section (b), the voltage potential signals are passed through buffers to isolate the current sensitive section (b) from the rest of the circuit. After passing through the buffers, the voltage signals enter section (c) where the signals are added

and subtracted from one another to produce voltage signals with x -axis and y -axis displacement information of the laser beam on the sensor. The following equations are used to calculate the x and y displacements

$$\begin{aligned} x &= \frac{(i_A+i_C)-(i_B+i_D)}{i_A+i_B+i_C+i_D} \\ y &= \frac{(i_A+i_B)-(i_C+i_D)}{i_A+i_B+i_C+i_D} \end{aligned} \quad (3.1)$$

where A , B , C , and D are the photodetector quadrants shown in Fig. 3.8 and i is the current flow from the quadrant.

The circuit schematic for this board is provided in Fig. 3.11, where R_1 is $36 \text{ M}\Omega$, R_2 is $10 \text{ k}\Omega$, C_1 is optional (pF range) for circuit dynamic response compensation, and C_2 is $0.1 \text{ }\mu\text{F}$. While the photodetector circuit has gain circuitry built in (section A), it does require bias circuitry to interface with our data acquisition system. Additional external bias circuitry is utilized to help interface the signals with both the data acquisition system and the microcontroller's analog to digital converter as is shown in Fig. 3.12 below the sensor circuit board. This board utilizes operational amplifiers to add voltage signals from potentiometers to the input signal in order to bias the output signals from the sensor circuit. The bias circuit board also contains gain circuitry, which is not used in this application (set gain=1) because of the built in gain circuitry in the photodetector circuit.

3.3 Control and Data Acquisition System

3.3.1 Controller Design and Implementation

Control of the z -axis is accomplished by using an ATxmega128A1 microcontroller. The microcontroller is programmed using a proportional-integral (PI) control algorithm to compensate for the error between the desired and actual photodetector signal.

The proportional controller (P) compensates for the instantaneous error, while the integral controller (I) addresses the cumulative error. In PI control the first step is to calculate the error between the current sensor value and the desired value

$$e_c = r - y \quad (3.2)$$

where e_c is the current error tabulated by subtracting the sensor measurement, y , from the desired value, r . In proportional control, this current error is use to calculate an input to the system that compensates based on a scale factor of the error. To calculate the proportional contribution of the system input, u_p , a gain, K_p , is multiplied by the present error, e .

$$u_p = K_p \cdot e \quad (3.3)$$

In integral control, the current error is added to the sum of all previous errors in order to calculate a system input. This shows that integral control uses history, while proportional control does not and this quality is used to compensate for the steady-state error rather than instantaneous error. To calculate the integral contribution, the present error must be added to the past history of errors

$$e_t = e_c + e_p \quad (3.4)$$

where e_t is the total error, e_c is the current error, and e_p are the previous cumulative errors. After the errors are summed together, the integral contribution to the system input, u_i , is

$$u_i = K_i \cdot e_t \quad (3.5)$$

where K_i is the integral gain. After the two separate system input contributions are

tabulated, u_p and u_i , both are added together to determine the total system input

$$u_t = u_p + u_i \quad (3.6)$$

where u_t is the total system input. Lastly, the previous error is updated to the total error and the process is repeated.

The microcontroller implemented in AFM z -axis control is the ATxmega128A1 microcontroller mounted onto a EVK XA1 development board as shown in Fig. 3.13(a). The output from the microcontroller is limited to 2.8 V, while the maximum input range for the piezo amplifiers is 0 to 10 V. A gain circuit is created to amplify the output voltage from the microcontroller by four. This allows the total range of the piezo's displacement to be utilized for control. The microcontroller and pin assignments are shown in Fig. 3.13.

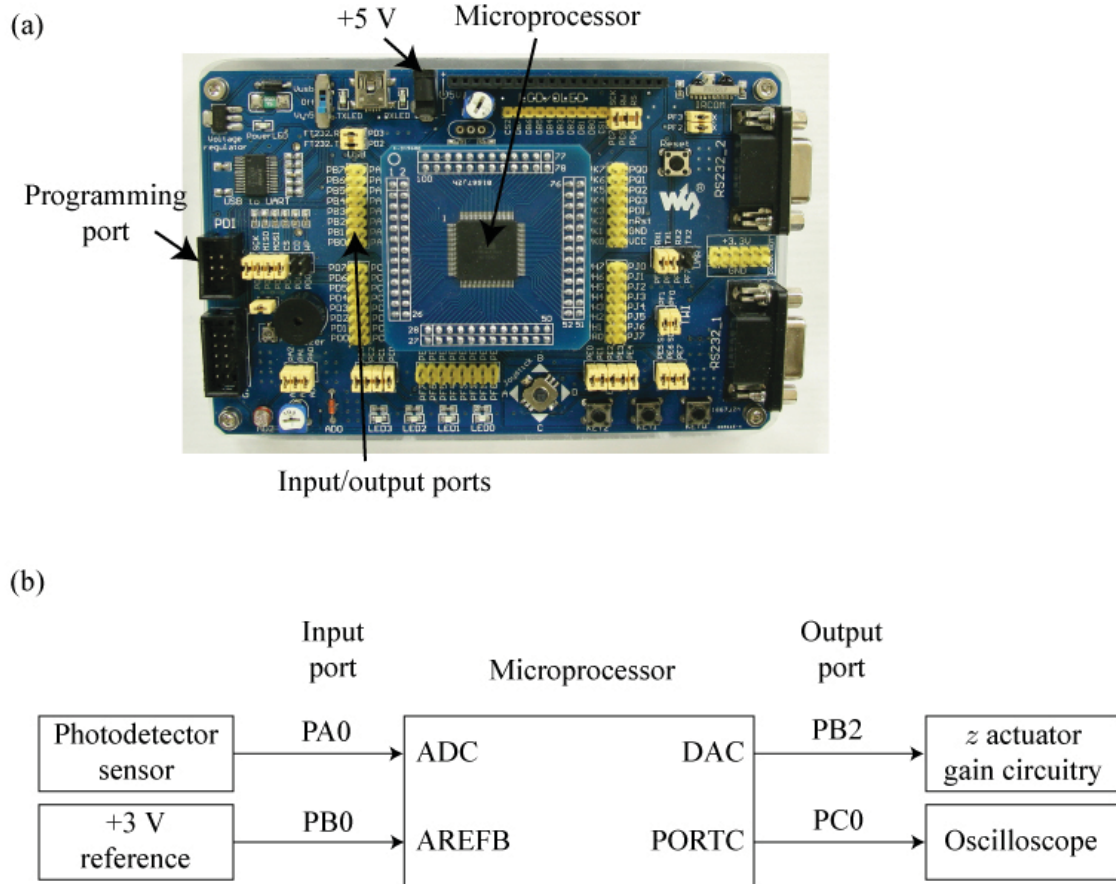


Figure 3.13: ATxmega128A1 microcontroller: (a) component labeling and (b) pin assignments.

Figure 3.13(a) identifies the major components utilized on the EVK XA1 development board. Figure 3.13(b) provides the pin assignments used in the programming code as well as the electrical connections completed for AFM z -axis control.

3.3.2 Data Acquisition System

The data acquisition system for the AFM incorporates a National Instruments PCI-6221 data acquisition card and LabVIEW software. The data acquisition card also has two analog output channels operating at 833 kS/s with 16-bit resolution and a ± 10 V output range, which provides control of the x -axis and y -axis for AFM control.

The analog input operates at 250 kS/s with 16-bit resolution and ± 10 V input range. The sampling rates are sufficiently fast for our application, since the bottleneck in our system is the desktop computer's performance capability as seen during testing. LabVIEW software provides a graphical user interface for the AFM imaging and control software. A custom program is created that provides the necessary controls needed for a complete AFM imaging system.

3.4 Fabricated Design

The fabricated AFM design incorporates components can be easily removed and replaced, so upgrades are possible for an future iterations. Key components include: coarse approach mechanism, fine approach mechanism, cantilever displacement sensor, cantilever probe holder, control system, data acquisition system, support circuitry, and user interface software. An overview of the entire fabricated and interfaced system is presented in Fig. 3.14. It provides an illustration of all the components that makeup the complete custom AFM system and to show that the AFM scanning platform needs additional off-the-shelf support equipment for a fully operational system (vibration isolation table, piezoelectric amplifiers, microcontroller, stepper motor control, and data acquisition system).

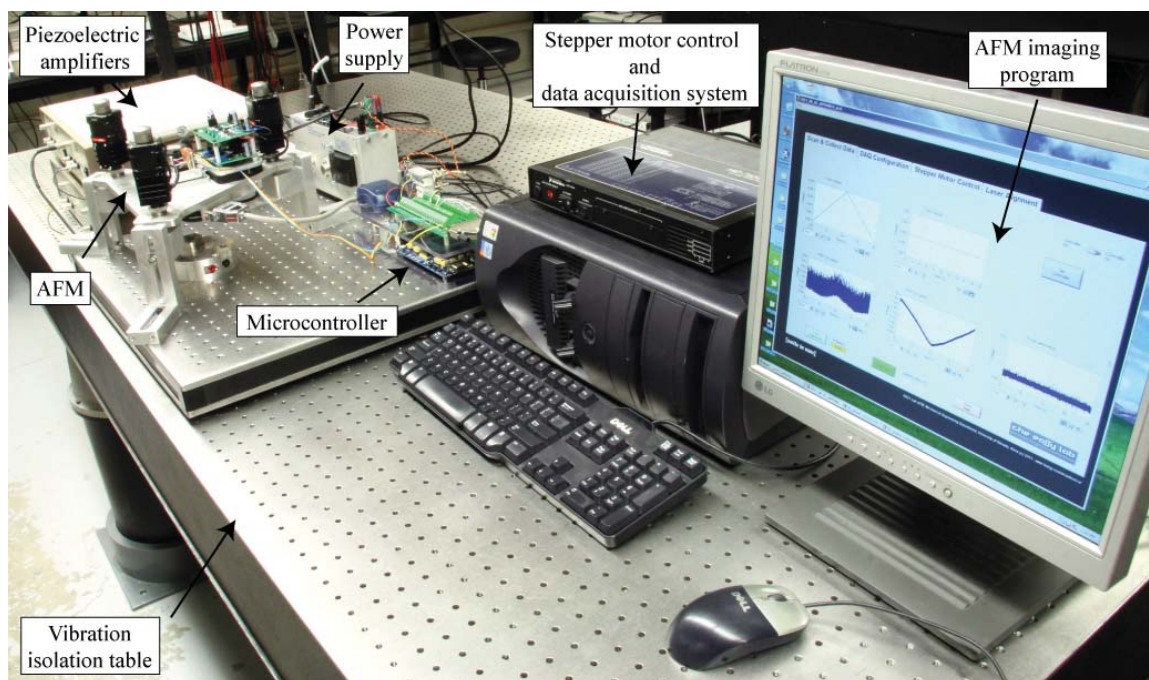


Figure 3.14: Overview of completed custom AFM system.

The vibration isolation table provides suppression of external vibrations from the surrounding environment, which helps reduce the noise of the system. Piezoelectric amplifiers supply the high voltage required to fully actuate the piezoelectric actuators (approximately 200 V). A microcontroller is used for close-loop control of the z -axis actuator, while a stepper motor controller provides the input signals for the approach mechanism on the AFM. The data acquisition system is a PCI card located inside the desktop computer and is interfaced with LabVIEW for control and data collection.

All custom parts were designed and fabricated in-house. Custom parts include: AFM base platform, adjustable base, laser holder, quadrant photodetector holder, power connector bracket, stepper motor connector bracket, mirror holder, high voltage connector bracket, microcontroller and data acquisition terminal brackets, and the AFM probe holder. Figure 3.15, 3.16, and 3.17 show the custom created LabVIEW program for AFM imaging and its operating procedure is shown in Fig. 3.18 and 3.19.



Figure 3.15: LabVIEW AFM program: AFM imaging screen.

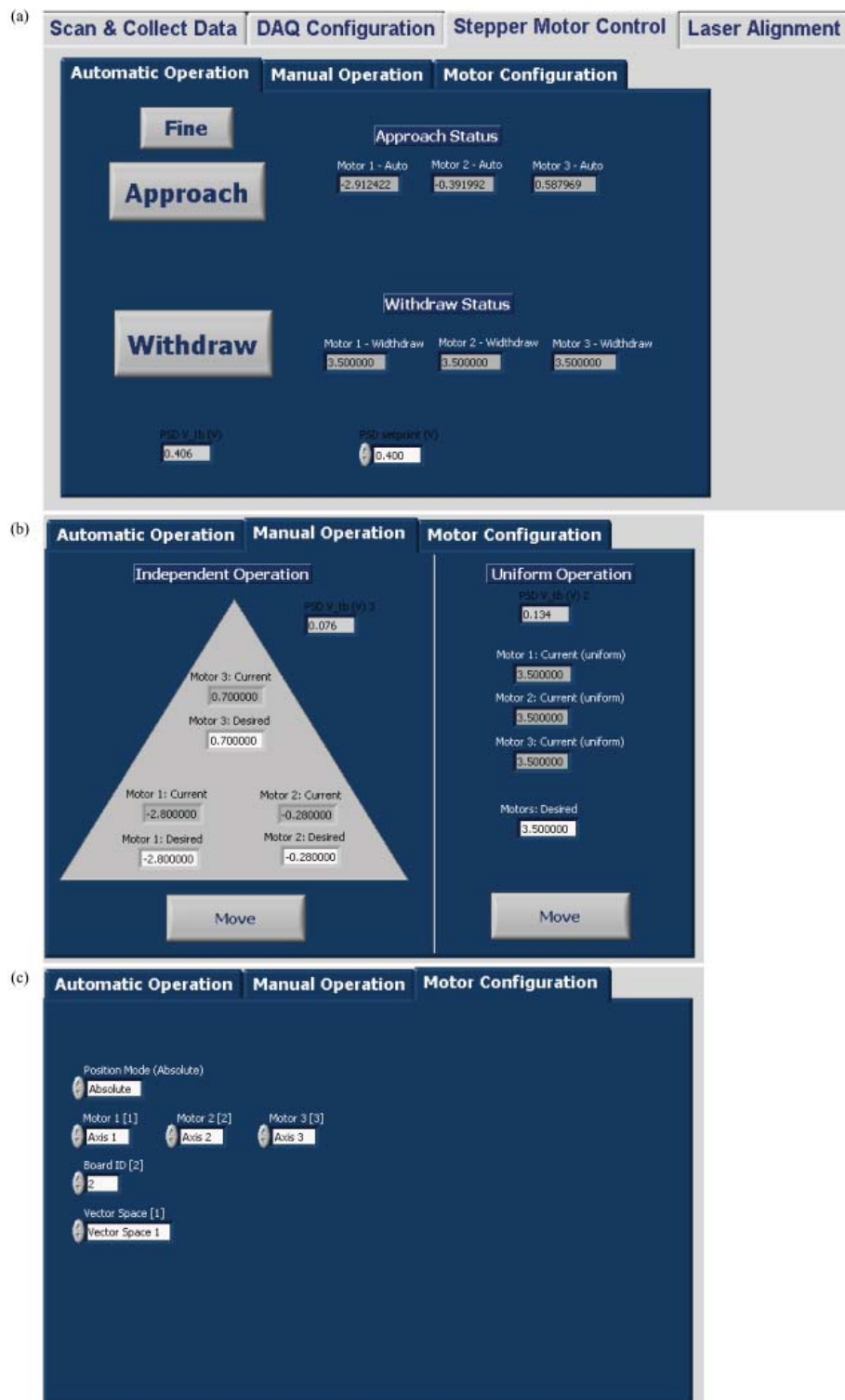


Figure 3.16: LabVIEW AFM program: stepper motor control with (a) automatic approach and withdraw, (b) manual movement, and (c) stepper motor settings.

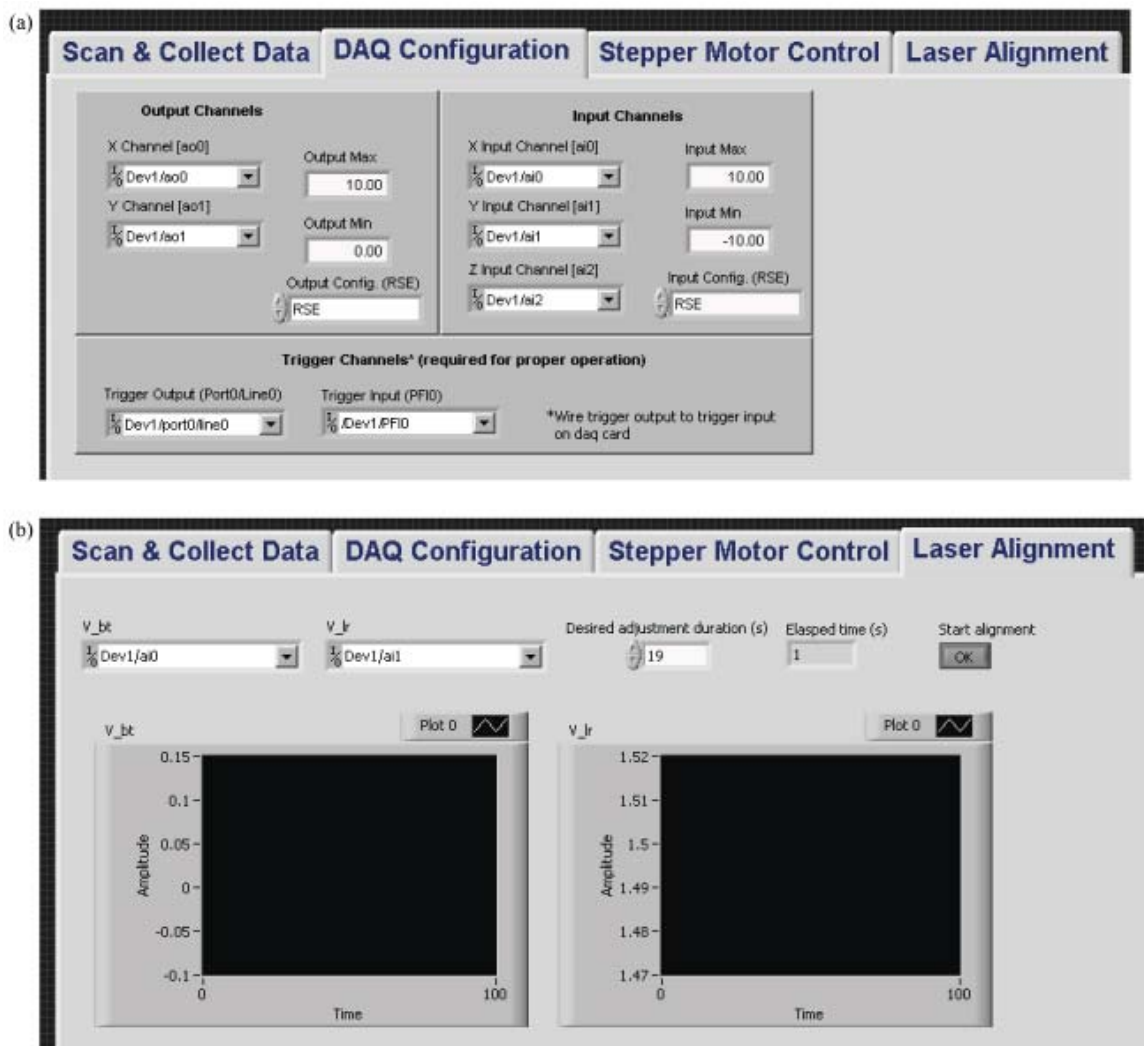
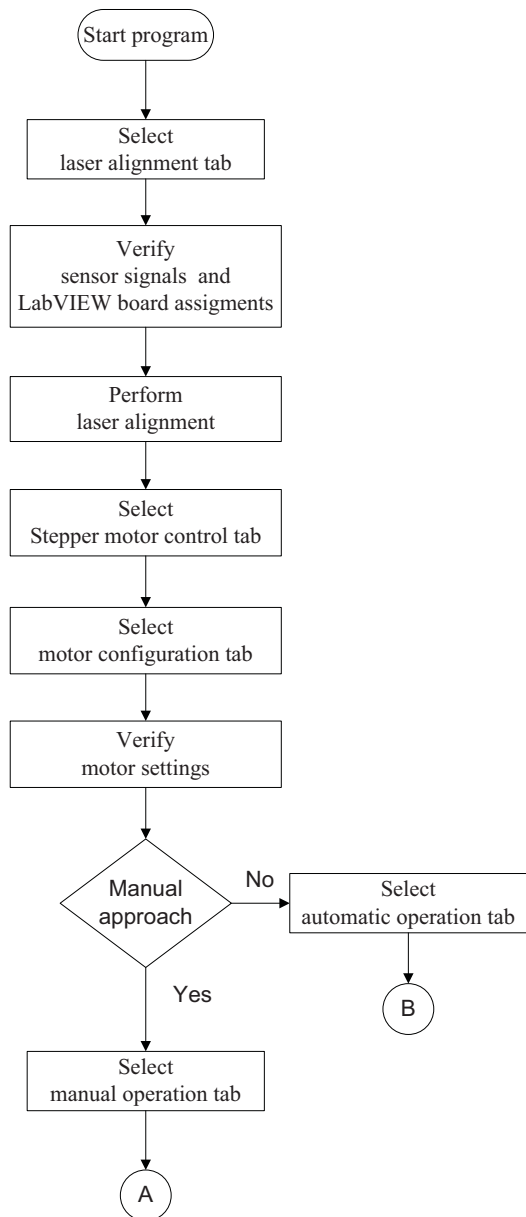
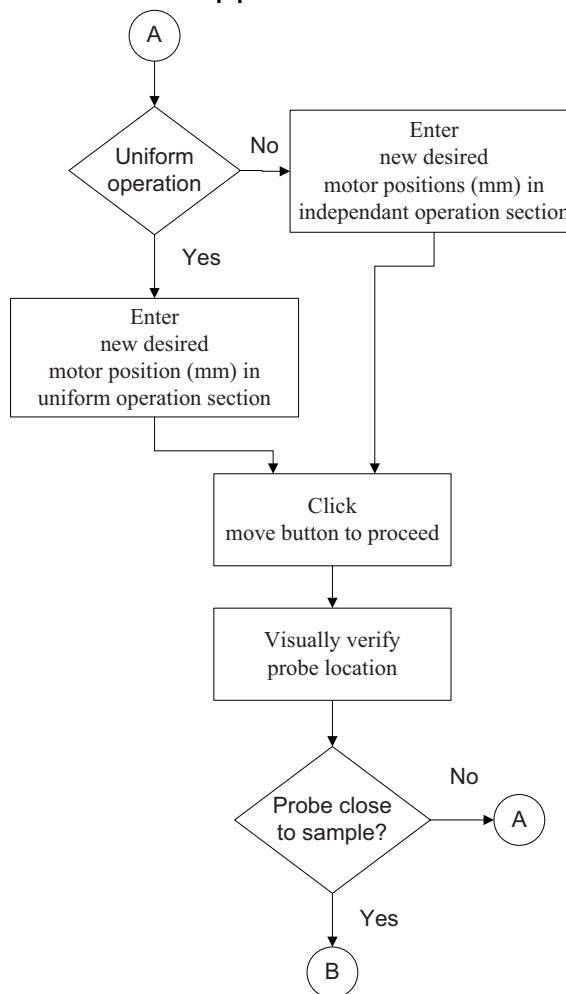


Figure 3.17: LabVIEW AFM program: (a) AFM imaging settings and (b) photodetector alignment screen.

Start of program



Manual approach



Automatic approach

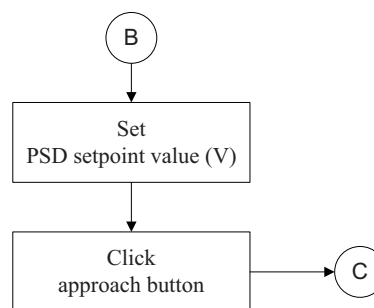


Figure 3.18: Flow chart for AFM program operation part 1 of 2.

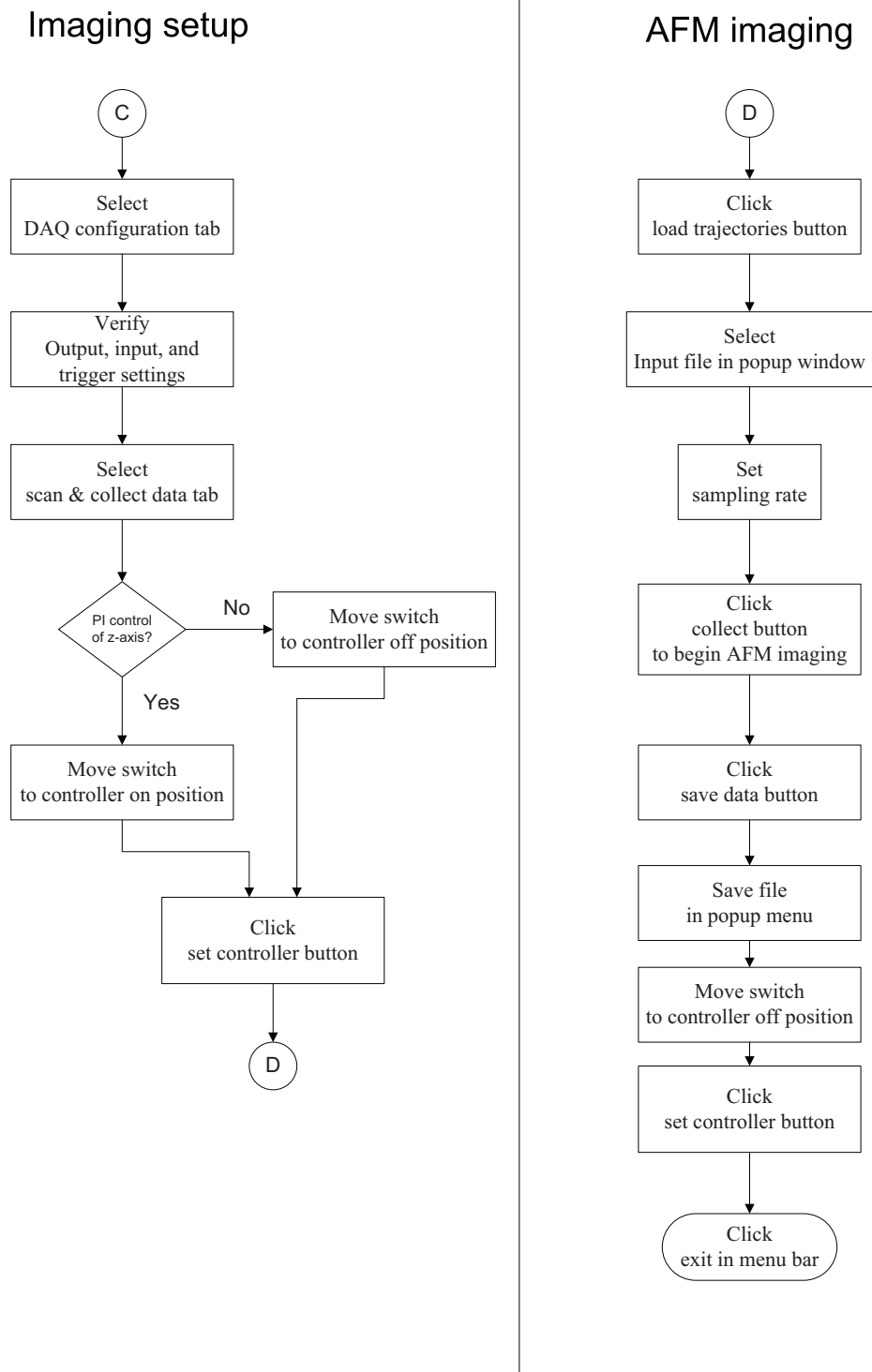


Figure 3.19: Flow chart for AFM program operation part 2 of 2.

3.5 AFM Characterization

The AFM characterization process includes the following tasks:

1. Obtain experimental frequency response of nanopositioner
2. Formulate models for x and y axes of nanopositioner
3. Quantify cross-coupling effect of nanopositioner
4. Obtain experimental frequency response of AFM probe holder
5. Formulate model for AFM probe holder

The coordinate system for the AFM system is shown in Fig. 3.5. Modifications to the long-range serial-kinematic nanopositioner are made to incorporate the necessary AFM hardware. Changes in the scanning stage's mass distribution from top to bottom as well as side to side resulted in changing the dynamic characteristics of the nanopositioner, thus an evaluation of the dynamic response is performed to investigate the new nanopositioner's dynamics. Results of the system's new dynamics are presented as frequency response plots shown in Fig. 3.20.

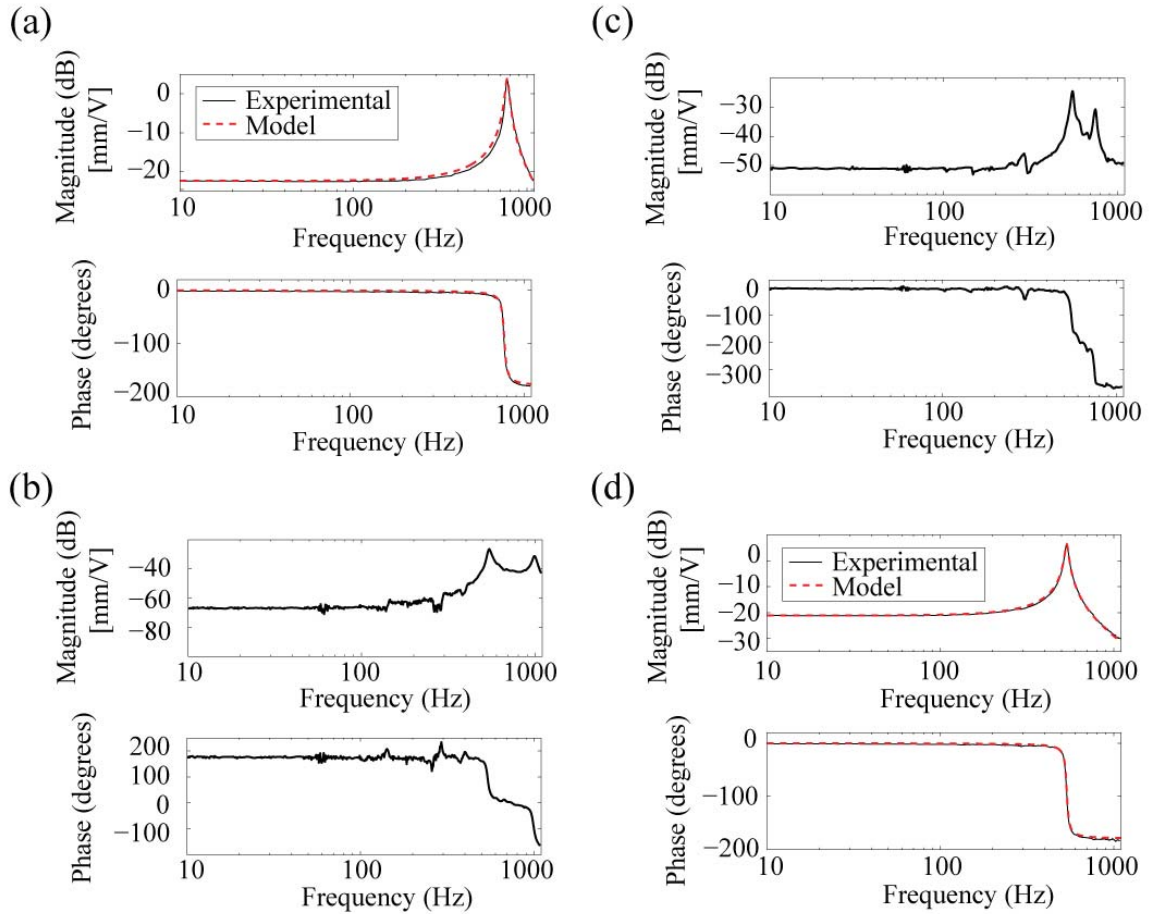


Figure 3.20: Nanopositioner frequency responses for (a) x -axis (actuation) to x -axis (sensing), (b) x -axis to y -axis, (c) y -axis to x -axis, and (d) y -axis to y -axis.

The results fit a second order system response for both the x -axis and y -axis with first mode resonances at 768 Hz and 535 Hz, respectively. Additionally, cross coupling measurements are made and presented in Fig. 3.20 as well. In the cross-coupling frequency responses in Fig. 3.20(b), the x -axis is actuated while the y -axis's displacement is recorded and vice versa for Fig. 3.20(c). Cross-coupling time responses are shown in Fig. 3.21. The time response plots reveal low cross coupling across full actuation range of the scanner ($40 \mu\text{m}$). Approximate cross coupling displacements of $0.42 \mu\text{m}$ and $0.34 \mu\text{m}$ are observed for the x -axis to y -axis and y -axis to x -axis,

respectively. This amounts to over 45 times less out-of-axis actuation when compared to in-axis actuation.

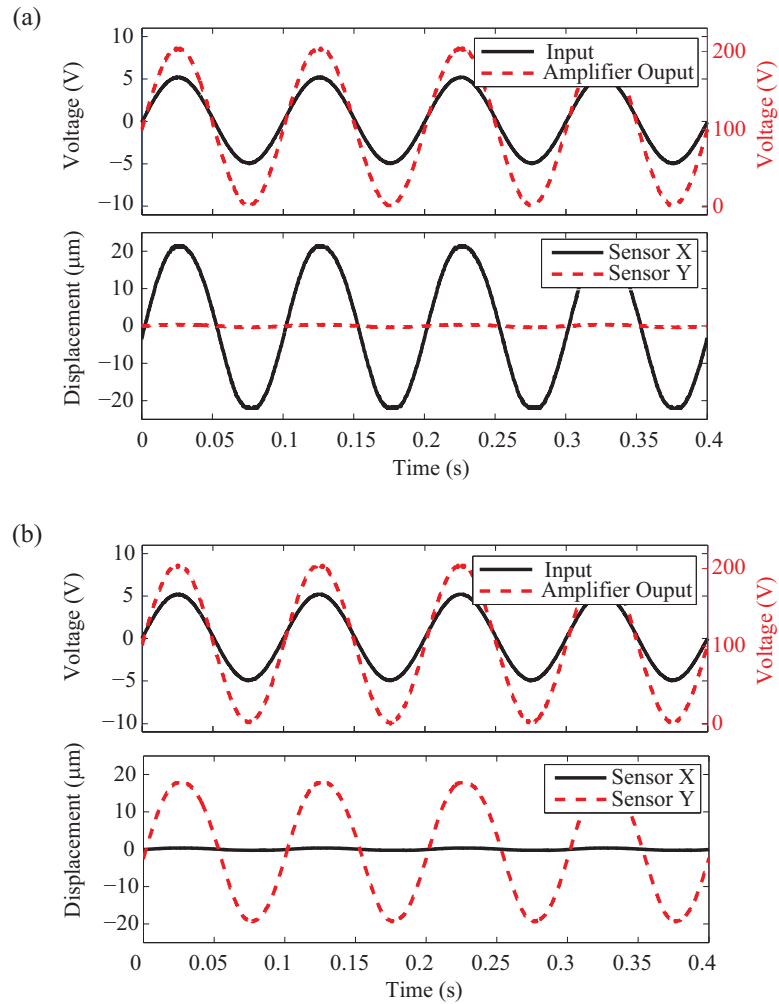


Figure 3.21: Time response of cross coupling from (a) x -axis to y -axis and (b) y -axis to x -axis

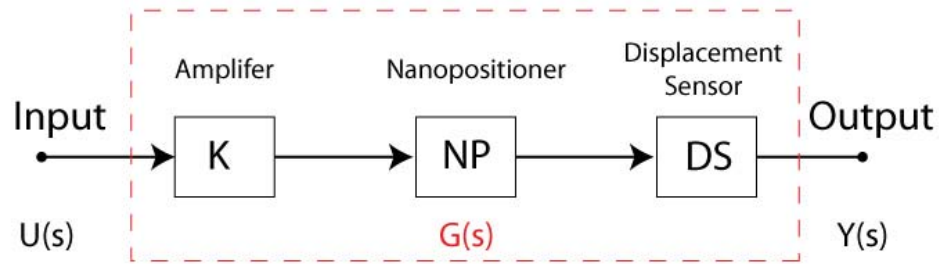


Figure 3.22: Block diagram of the modeled system.

A ± 5 V, 10-Hz sinusoidal reference input is applied to the system (± 5 V for full range) where the amplifier, K, gains the output by 20-times and the maximum output from the amplifier is from 0-200 V. The amplifier output voltage is then sent to the nanopositioner, NP, where the piezoelectric actuators are used to drive the AFM scanner. The scanner displacement measurements are performed using ADE 5130 and ADE 4810S capacitive displacement sensor systems, DS, which output a voltage that is proportional to the displacement of the nanopositioning stage. Frequency responses from 10 Hz to 1 kHz are performed to create a model for the system, $G(s)$. A second order system fits well to the experimental data and Eqs. (3.7) and (3.8) are used for the x -axis and y -axis, respectively.

$$G_x(s) = \frac{1.78 \times 10^6}{s^2 + 236.6s + 2.331 \times 10^7} \quad (3.7)$$

$$G_y(s) = \frac{9.966 \times 10^5}{s^2 + 141.2s + 1.13 \times 10^7} \quad (3.8)$$

The z -axis of the AFM stage is characterized as well using a laser vibrometer, which measures velocity, so the recorded data is integrated for displacement data. Figure 3.23 shows the raw data with a model for the system dynamics.

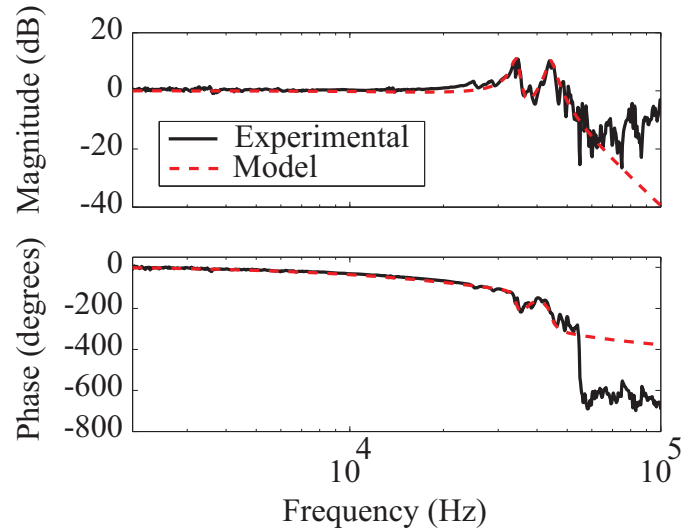


Figure 3.23: The z -axis experimental frequency response compared with model.

The model presented here is a higher order model than the x and y -axis models. The additional poles and zeros are needed to capture the first two peaks in the magnitude plot along with the associated phase response. The model's transfer function is presented in Eq. (3.9) and captures the experimental results up to 50 kHz.

$$G_z(s) = \frac{s^2 + 2.2 \times 10^4 s + 5.34 \times 10^{10}}{a(s + 2.5 \times 10^5)^3 (s^2 + 1.75 \times 10^4 s + 7.79 \times 10^{10})} \quad (3.9)$$

$$a = s^2 + 1.01 \times 10^4 s + 4.647 \times 10^{10}$$

3.5.1 AFM Operation Validation

In order to validate the AFM's operations, the AFM is scanned over a calibration sample (Nanosurf No. BT01015) with a $10 \mu\text{m}$ x, y periodicity and a 98 nm z depth using a commercial AFM probe (BudgetSensors' ContAL-G). The results from controller implementation into the system is shown and the impact is compared to a system without a controller. Figure 3.24 demonstrates a standard AFM deflection image, which means that there is no voltage change in the piezo, while it is being scanned across a sample. The PSD sensor gathers all the information about the

sample's surface features by recording position changes across the sensor due to cantilever deflection. The single line trace shows over a 0.5 V change in surface height for the surface features, which are specified at 98 nm. The piezo amplifier plot has no features and remains a constant voltage throughout the imaging process.

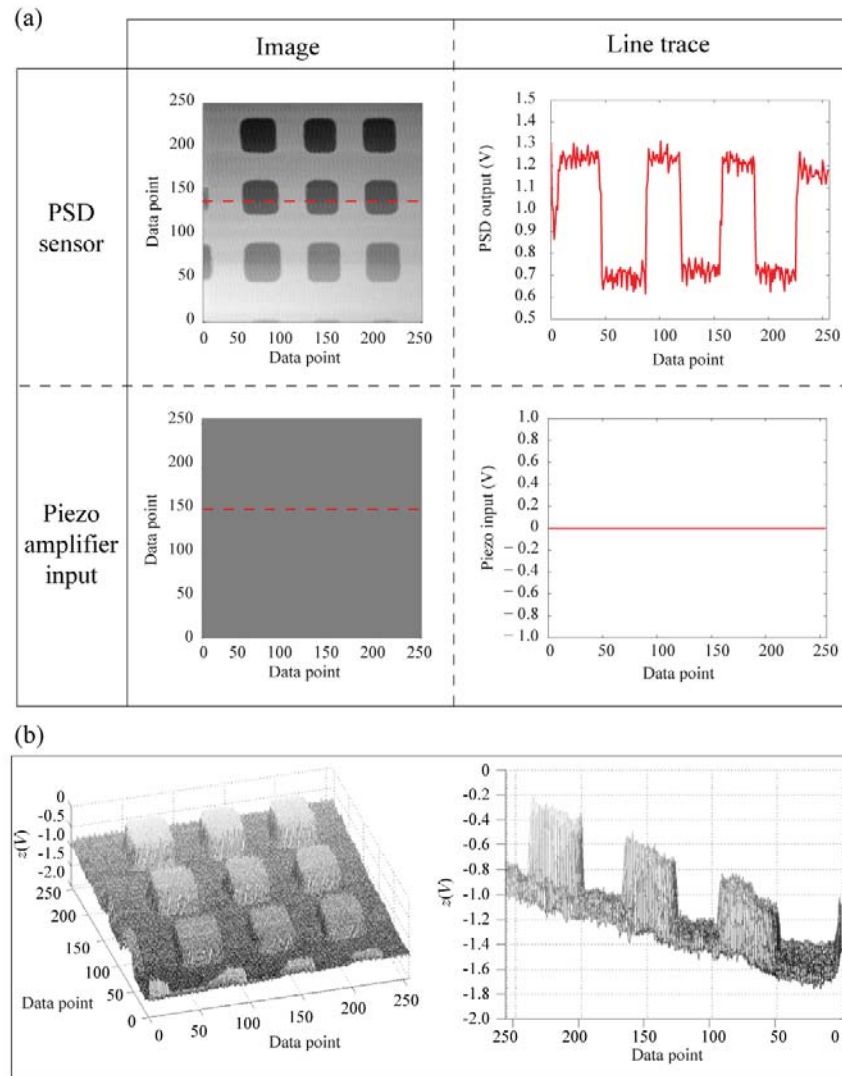


Figure 3.24: PSD sensor output and piezo input voltage for a 256×256 pixel image at a 1-Hz line rate scan with no controller or z -axis input. Two-dimensional plots are presented in (a), while a three dimensional PSD sensor plot is presented in (b, left) and a rotated side view PSD sensor plot is presented in (b, right).

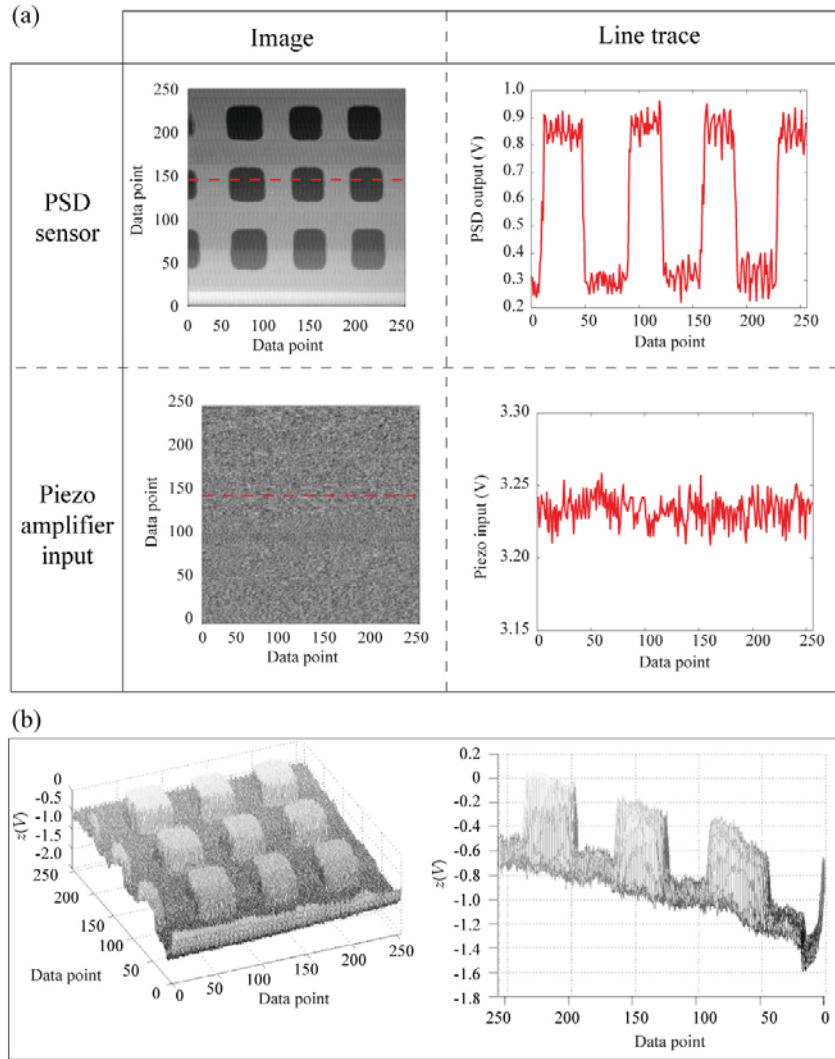


Figure 3.25: PSD sensor output and piezo input voltage for a 256×256 pixel image at a 1-Hz line rate scan with the following controller gains: $K_p = 1 \times 10^{-6}$ and $K_i = 1 \times 10^{-11}$. Two-dimensional plots are presented in (a), while a three dimensional piezo amplifier input voltage plot is presented in (b, left) and a rotated side view piezo amplifier input voltage plot is presented in (b, right)

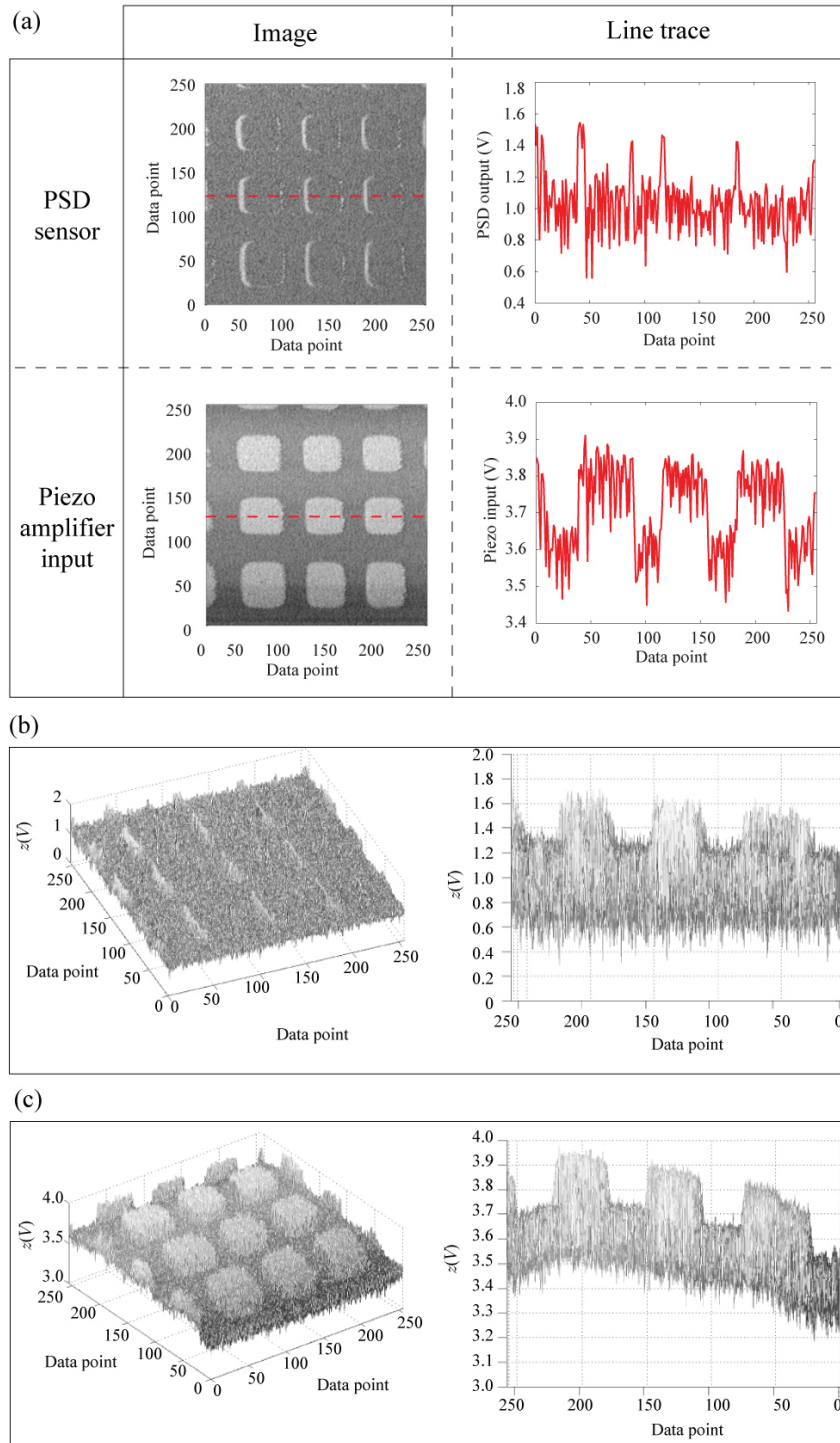


Figure 3.26: PSD sensor output and piezo input voltage for a 256×256 pixel image at a 1-Hz line rate scan with the following controller gains: $K_p = 2 \times 10^{-2}$ and $K_i = 1 \times 10^{-5}$. Two-dimensional plots are presented in (a), while a three dimensional PSD sensor and piezo amplifier input voltage plots are presented in (b, left) and (c, left), respectively and PSD sensor and piezo amplifier input voltage plots are rotated side views are presented in (b, right) and (c, right), respectively.

Figure 3.25 shows a similar image to that in Fig. 3.24. The deflection signal is over 0.5 V, which is the same as the system with no controller; however the piezo amplifier input has very slight changes. These changes are observed in the line trace to the right of the piezo amplifier input image plot and show that the overall trend remains a constant value, which is similar to the no controller scenario.

Figure 3.26 is a sharp contrast to the previous two plots. The photodetector (PSD) sensor image only shows outlines from the sample's surface, while the piezo amplifier input image looks similar to the PSD sensor image from the previous plots. The outlines in the PSD sensor image plot is cause by the abrupt change in surface height and the large error associated with the immediate error; however as the scan progresses from left to right, the outline disappears as the controller is able to compensate for the past error. This compensation shows up in the piezo amplifier input. The rise of to the steady state value is not as fast as the PSD sensor output in the previous plot, but a steady state value is observed in the plateau of the piezo amplifier input line trace. The AFM is setup using the procedure found in Fig. 3.27. The piezo amplifier input has a low range that can be increased by modifying the external gain circuitry.

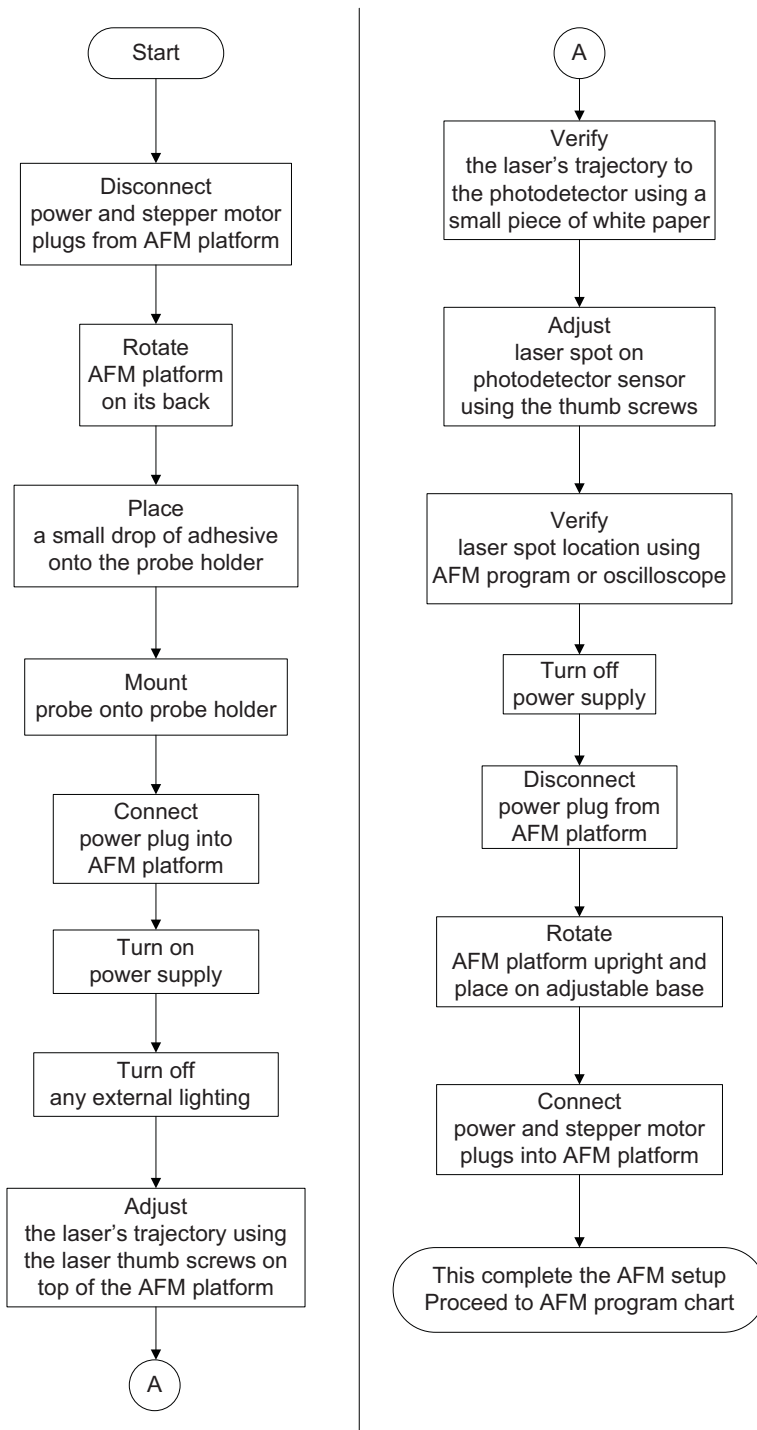


Figure 3.27: Flow chart for atomic force microscope setup.

Chapter 4

Multifunctional Probe Design, Model, and Fabrication

This chapter presents design and fabrication results for the multifunctional probe, which includes electro-thermo-mechanical and dynamic modeling along with finite element analysis (FEA) simulation results. By analyzing the probe's actuation and dynamics, the probe's design is verified and its multifunctional application is presented in Fig. 4.1 and 4.2.

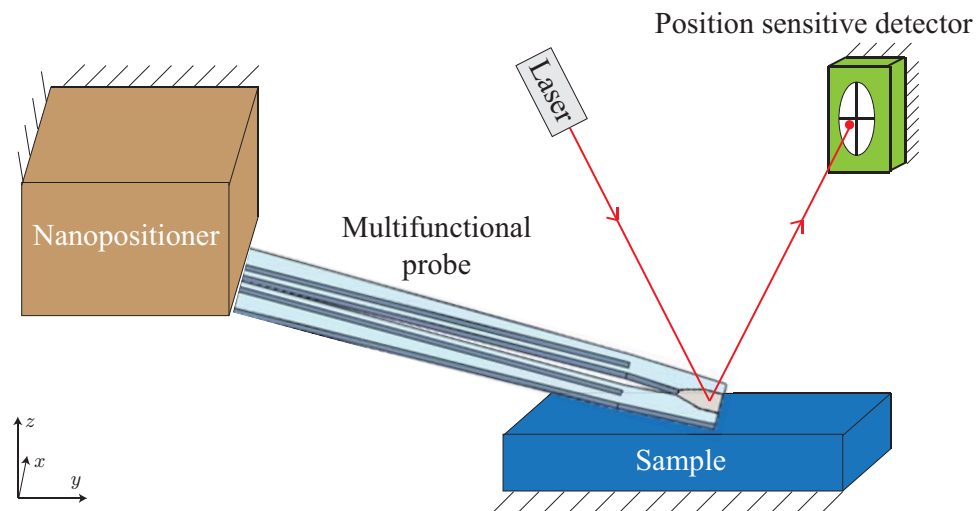


Figure 4.1: Multifunctional probe implementation into atomic force microscopy system with scanning application.

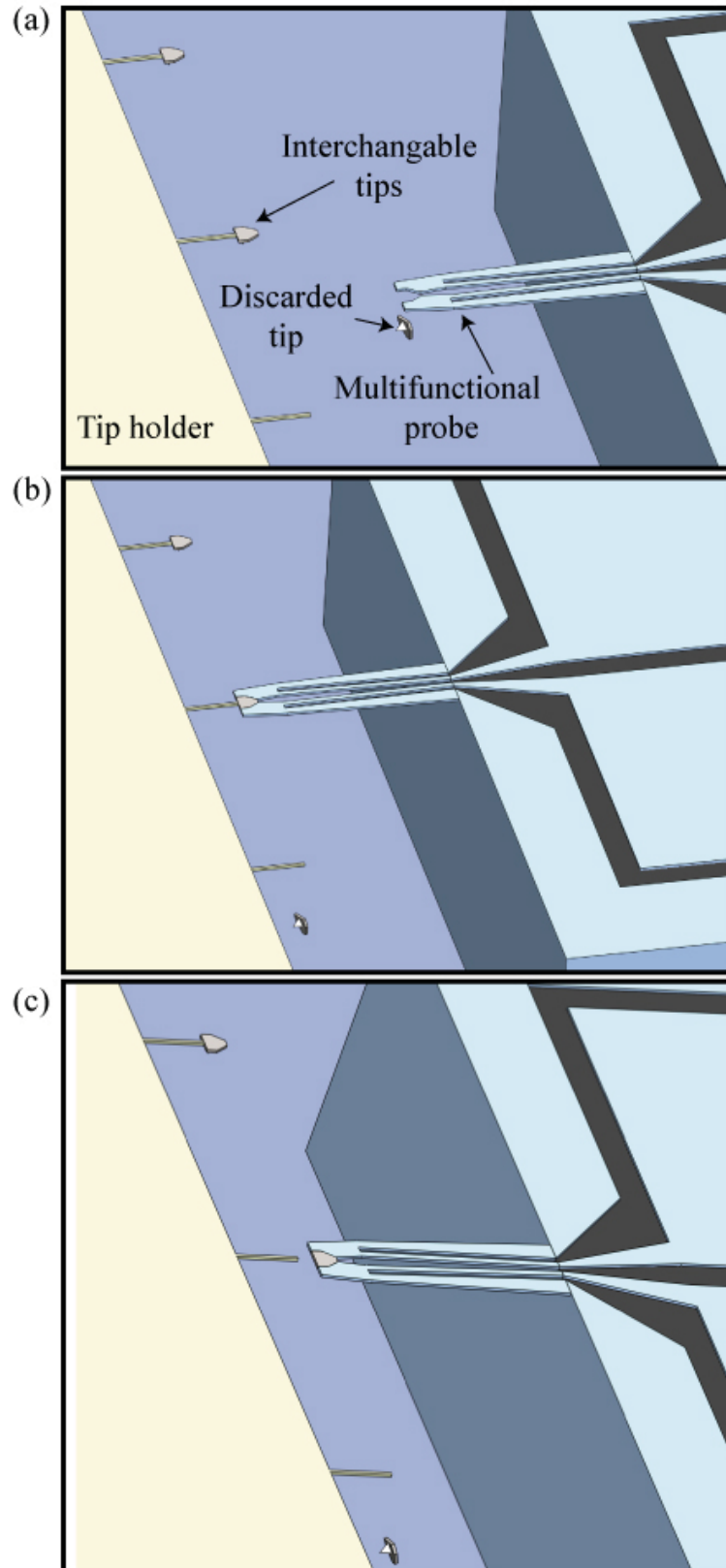


Figure 4.2: Interchangeable tip concept of the multifunctional probe application for the following tasks: (a) discarding worn or fouled tip, (b) grasping a new tip, and (c) releasing tip from tip holder begin specialized tip operations.

The basis for the probe's design is to maintain traditional cantilever beam dynamics, while still maintaining a minimum of $2\ \mu\text{m}$ of lateral displacement per actuator. The probe's design utilizes two actuators with a passively gripping mechanism to perform pick and place of objects. After consultations with UFL's MEMS fabrication, feature line widths are limited to $10\ \mu\text{m}$ with minimum device thickness of $5\ \mu\text{m}$ for prototyping. Overall physical dimensions for the probe are $400\ \mu\text{m}$ length and $110\ \mu\text{m}$ width. The designed multifunctional probe is analyzed as a cantilever beam with fixed end (silicon chip anchor) and a free end (gripping jaw end). Lastly in this chapter, a fabrication recipe is presented along with images of the fabricated probes.

4.1 Electro-Thermo-Mechanical Modeling

The objective of this section is to provide a model that takes current input and outputs a steady state displacement value for a single electro-thermo-mechanical actuator. This model incorporates the resistive heating effect of the silicon materials, while also taking into account the convective heat transfer out of the material and into air.

Silicon microbeams are usually simplified in one dimension for electrothermal analysis because the length is significantly larger than the size of its cross-section [112,113]. Figure 4.3 is referenced throughout this section and provides (a) actuator dimensions, (b) model simplification into three sections, (c) coordinate system for heat flow analysis, and (d) heat flow through a differential element of the actuator.

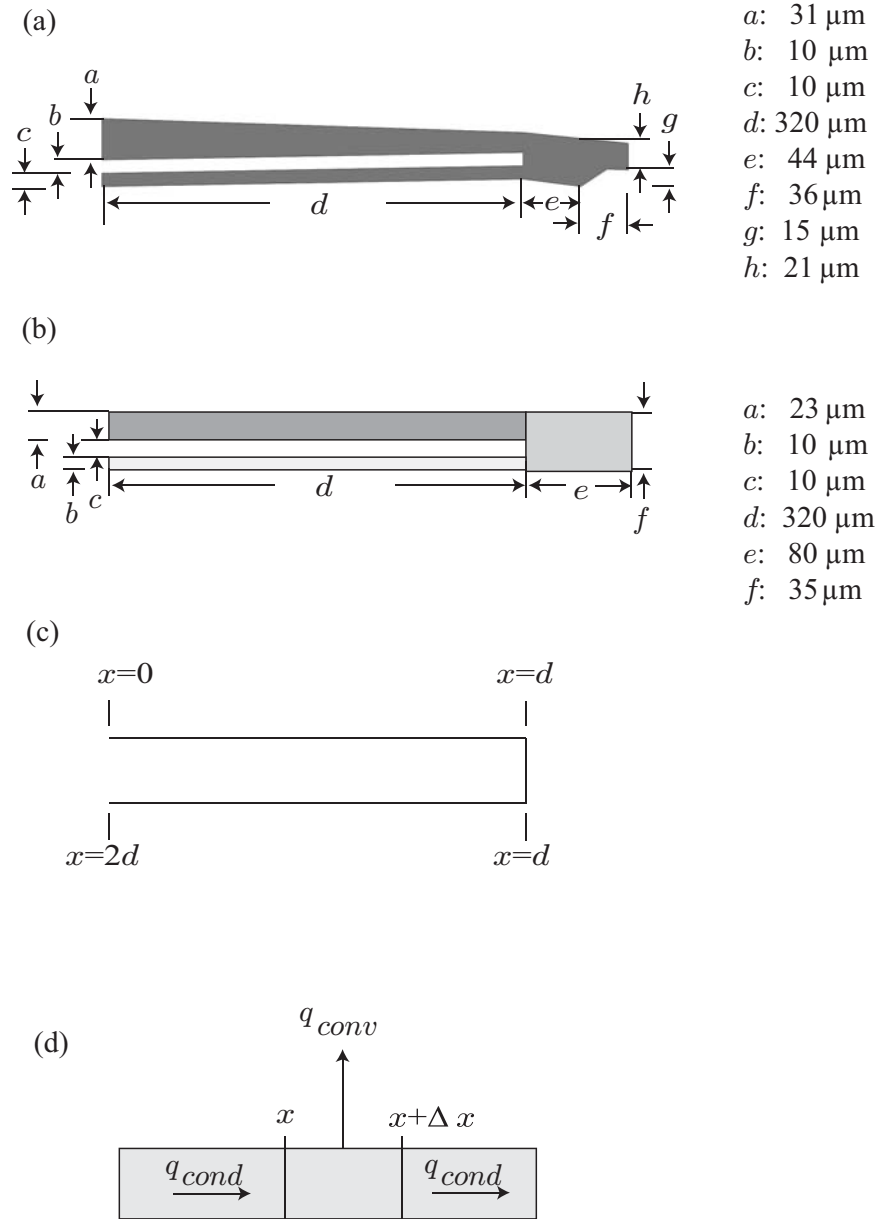


Figure 4.3: Multifunctional probe modeling parameters: (a) multifunctional probe dimensions, (b) model simplification, (c) model coordinate system, and (d) heat flow within the probe.

The simplification is made because all sections have the same material composition and resistivity throughout. This allows for an averaged volume for the sections while still maintaining the same averaged resistivity resulting in no change in thermal

conduction through the actuator. The resistivity of silicon has a temperature range where a linear approximation can be made and is shown in literature [114]. In this model, the resistivity (ρ) is assumed to have a linear temperature coefficient (ξ)

$$\rho(T) = \rho_0[1 + \xi(T - T_0)] \quad (4.1)$$

where T is the temperature of the element at a particular point in time and ρ_0 is the resistivity at the starting temperature, T_0 . The substrate in this analysis is silicon and the heat flow equation is derived from Fig. 4.3(d). The model uses the differential element (Δx) of the simplified actuator (Fig 4.3(b)). The differential element has a length of Δx , width of w , and thickness of t . Using a steady state analysis and having the free heat convection out of the actuator equal to the resistance heating, results in

$$-k_p w t \left[\frac{dT}{dx} \right]_{x+\Delta x} + \Delta x w (T - T_s) h = -k_p w t \left[\frac{dT}{dx} \right]_x + J^2 \rho w t \Delta x \quad (4.2)$$

where J is the current density flowing through the element, k_p is the thermal conductivity of silicon, h is the convective heat transfer coefficient of air, T_s is the probe's base substrate temperature, and T is the element temperature. Now taking the limit as Δx goes to zero in Eq. (4.2) yields

$$\frac{h}{t} (T - T_0) = k_p \left[\frac{d^2 T}{dx^2} \right] + J^2 \rho \quad (4.3)$$

where the right side is the net rate of heat conduction within the element per unit volume (first term) and the heat generation per unit volume within the element (second term). The left side is rate of heat loss through convection per unit volume of the element. Now rearranging terms and using Eq. (4.1), the following differential equation is obtained.

$$\frac{d^2\theta(x)}{dx^2} - a^2 \theta(x) = 0 \quad (4.4)$$

$$\begin{aligned} \theta(x) &= T(x) - T_\theta \\ T_\theta &= T_s + \frac{J^2 \rho_0}{k_p a^2} \\ a^2 &= \frac{h - J^2 \rho_0 \xi t}{k_p t} \end{aligned} \quad (4.5)$$

Now solving Eq. (4.4) and applying it to the hot and cold arm, the following temperature distribution is found

$$\begin{aligned} T_h(x) &= A e^{a_h x} + B e^{-a_h x} + T_s + \frac{J^2 \rho_0}{k_p a^2} \\ T_c(x) &= C e^{a_c x} + D e^{-a_c x} + T_s + \frac{J^2 \rho_0}{k_p a^2} \end{aligned} \quad (4.6)$$

where $T_h(x)$ and $T_c(x)$ are the temperature distributions along the hot and cold arm length, respectively. The A, B, C, and D constants are found using boundary conditions. The following boundary conditions are used to solve the two equations above for the four unknown constants

1. At $x = 0 \mu\text{m}$, $T_h(0) = T_s = 27^\circ\text{C}$

$$27^\circ\text{C} - T_H = A + B$$

2. At $x = 640 \mu\text{m}$, $T_c(0) = T_s = 27^\circ\text{C}$

$$27^\circ\text{C} - T_C = C e^{a_c x} + D e^{-a_c x}$$

3. At $x = 320 \mu\text{m}$, $T_c(320) = T_h(320)$

$$T_H - T_C = -A e^{a_h x} - B e^{-a_h x} + C e^{a_c x} + D e^{-a_c x}$$

4. At $x = 320 \mu\text{m}$, $T'_c(320) = T'_h(320)$

$$A w_h a_h e^{a_h x} - B w_h m_h e^{-a_h x} = C w_c m_c e^{a_c x} - D w_c a_c e^{-a_c x}$$

where w_c and w_h are hot and cold arm widths, while a_c and a_h are found using Eq. (4.5). Using the equations found above, the system of equations are written in matrix form as the following

$$\begin{bmatrix} 1 & 1 & 0 & 0 \\ 0 & 0 & e^{m_c(2L)} & e^{m_c(2L)} \\ -e^{m_h(L)} & -e^{-m_h(L)} & e^{m_c(L)} & e^{-m_c(L)} \\ e^{m_h(L)} & -e^{-m_h(L)} & -\lambda e^{m_c(L)} & \lambda e^{-m_c(L)} \end{bmatrix} \begin{bmatrix} A \\ B \\ C \\ D \end{bmatrix} = \begin{bmatrix} T_s - T_H \\ T_s - T_C \\ T_H - T_C \\ 0 \end{bmatrix} \quad (4.7)$$

where $\lambda = \frac{w_c m_c}{w_h m_h}$. Once the constants are determined, they are inserted in Eq. (4.6) and $T_h(x)$ is determined. To simplify the model, the resistive heating of cold arm's is assumed to be zero due to its larger cross-sectional area ($> 2 \times$ (cold arm width)). This leaves conduction from the hot arm to the base and free convection to air as the sources of heat transfer through the length of the cold arm. The heat transfer rate (q_x) through the arm is found as the following [115].

$$q_x = (-kA + \frac{1}{hA}) \frac{dT}{dx} \quad (4.8)$$

where k is the thermal conductivity of silicon, A is the cross-sectional area of the cold arm, and h is the convection heat transfer coefficient. By separation of variables and integrating both sides, the temperature distribution, $T(x)$, is represented as

$$\begin{aligned} q_x \int_{x_1}^x dx &= \frac{-khA^2+1}{hA} \int_{T_1}^{T(x)} dT \\ q_x &= \frac{-khA^2+1}{(x-x_1)hA} (T(x) - T_1) \\ T(x) &= \frac{q_x(x-x_1)hA}{-khA^2+1} + T_1 \end{aligned} \quad (4.9)$$

The temperature distribution throughout the cold arm is found by solving for q_x at location x_2 with associated temperature T_2 and plugging this into the temperature

distribution equation. Doing so results in the following equation

$$T(x) = \frac{(T_2 - T_1)(x - x_1)}{x_2 - x_1} + T_1 \quad (4.10)$$

where T_2 and T_1 are the two known boundary temperatures (end temperature of hot arm and substrate temperature, respectively). Now the temperature distributions throughout the hot and cold arms can be written as the following piecewise function that takes an input current and outputs a temperature distribution

$$T(x) = \begin{cases} A e^{a_h x} + B e^{-a_h x} + T_s + \frac{J^2 \rho_0}{k_p a^2}, & 0 \leq x \leq 320 \mu m \\ \frac{(T_2 - T_1)(x - x_1)}{x_2 - x_1} + T_1, & 320 \mu m < x \leq 640 \mu m \end{cases} \quad (4.11)$$

where $0 \leq x \leq 320 \mu m$ domain represents the hot arm and $320 \mu m < x \leq 640 \mu m$ domain represents the cold arm. Figure 4.4 provides a plot of the temperature distribution through the hot and cold arms using a 5.5-mA current input into the system. A 5.5-mA current input is chosen because the temperature distribution of the hot arm does not rise above 500°C (approximately 800 K). The parameter values used in this model are valid from 300 K to 800 K.

Now that the temperature distribution throughout the hot and cold arms have been established, the deflection of each arm can be calculated by taking the average temperature of each arm and applying it to silicon's thermal expansion coefficient (α) to yield

$$\begin{aligned} \Delta L_H &= \alpha \int_0^L (T_h(x) - T_s) dx = \alpha L (T_{avg,H} - T_s) \\ \Delta L_C &= \alpha \int_L^{2L} (T_c(x) - T_s) dx = \alpha L (T_{avg,C} - T_s) \end{aligned} \quad (4.12)$$

where ΔL_H and ΔL_C are displacements of the hot and cold arm. Using geometric relations of the probe's approximation found in Fig. 4.3(b) with the results above, the

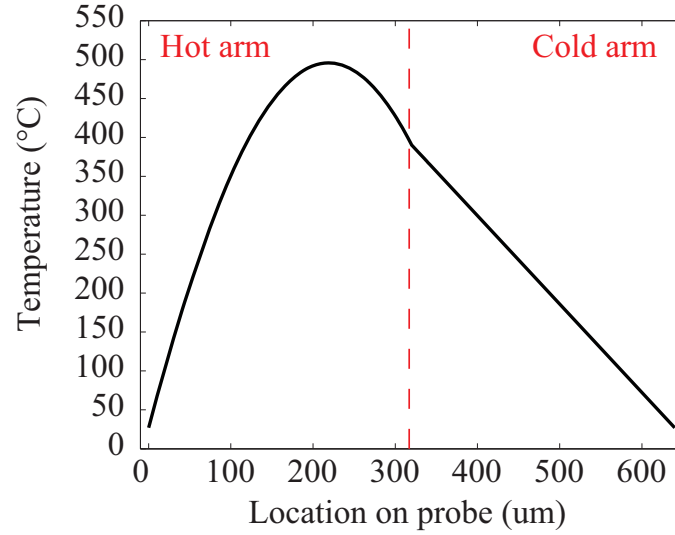


Figure 4.4: Temperature distribution along the multifunctional probe.

difference in displacements generated by the thermal expansion mismatch results in a 0.82° angle of inclination from the cold arm displacement to the hot arm displacement. The approximation uses a $80 \mu\text{m}$ end effector to amplify the displacement mismatch of the cold and hot arms to result in a $1.14 \mu\text{m}$ lateral displacement for a single actuator ($2.28 \mu\text{m}$ total gripper displacement).

Now, the probe's lateral displacement, x , throughout the length of the probe, y , is investigated in Fig. 4.5.

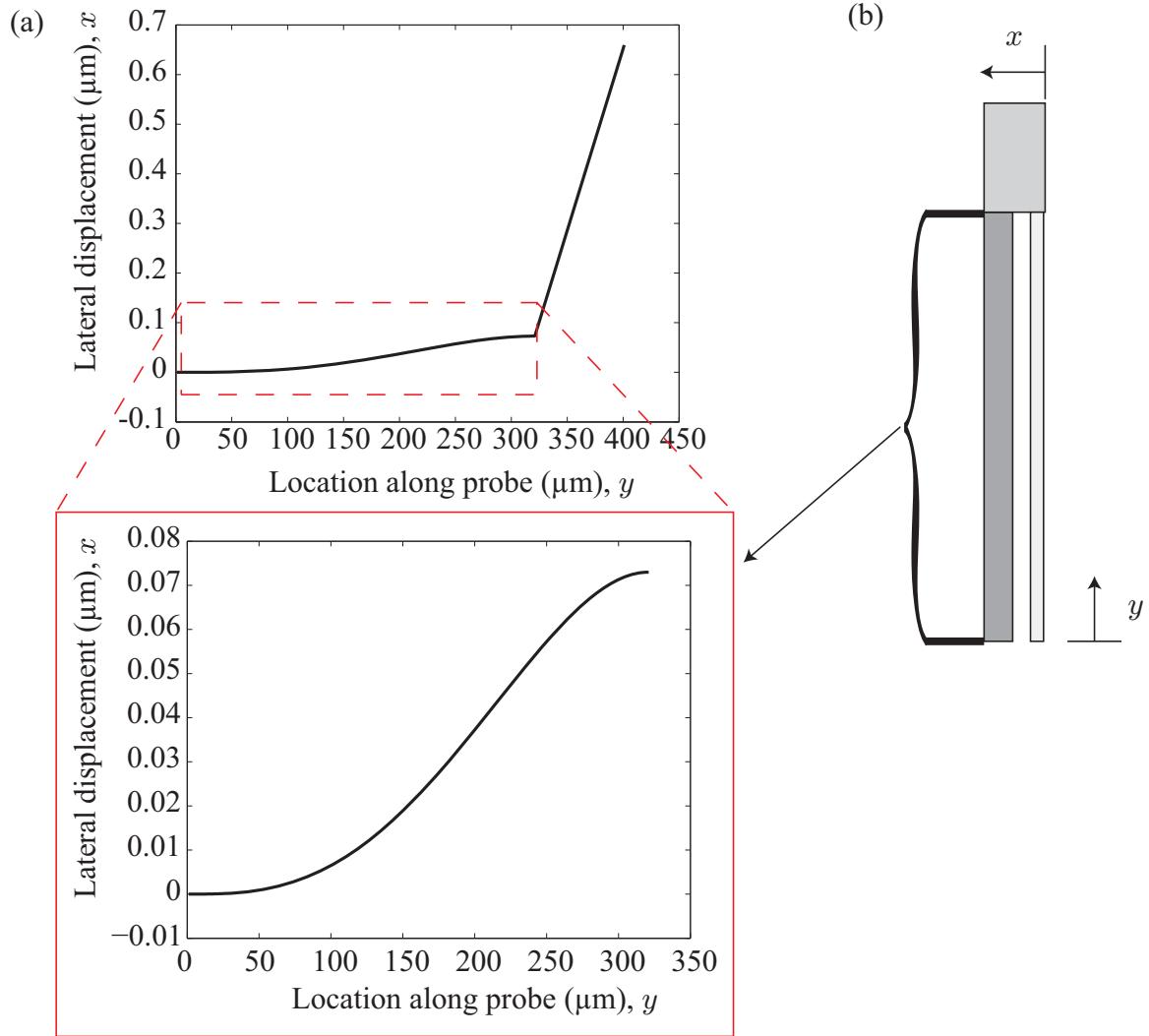


Figure 4.5: Multifunctional probe displacement along its length: (a) displacement plots and (b) corresponding geometric layout of the plots.

The resulting displacement at the distal end of the probe ($y = 400 \mu\text{m}$) is $0.67 \mu\text{m}$, which is almost half the displacement of the averaged lateral displacement found using an averaged temperature throughout each arm ($1.14 \mu\text{m}$). The large discrepancy is due to the nonlinear temperature difference between the hot and cold arm, which is observed in the probe's lateral displacement from 0 to $320 \mu\text{m}$. At the bottom and top of the hot and cold arms, the temperatures are assumed to be the same in the model, thus the differences in expansion coefficients will be minimal close to these

boundaries and results in low lateral displacement. The linear lateral displacement region from 320 μm to 400 μm is contributed to the assumption that no heating is in this part of the probe and that all the displacement below the arm is amplified by geometric relationships to the end of the probe. The results from this section is presented in Table 4.1.

Table 4.1: Calculated lateral displacement at the distal end of multifunctional probe.

Calculation Method	Single actuator disp. (μm)	Probe total disp. (μm)
Averaged	1.14	2.28
Non-averaged	0.67	1.34

4.2 Dynamic Modeling

This section provides a simplified cantilever beam model for the multifunctional probe with estimated deflection. FEA simulation results on the actual probe dimensions is conducted to determine physical constraints that need to be placed onto the multifunctional probe's design, such that typical AFM probe dynamics can be mimicked. Using cantilever beam analysis, analytical predictions of the modal frequencies are obtained. First, a geometric approach is used to obtain the deflection curve of a beam differential equation [116, 117]. Figure 4.6 contains additional information to clarify the following equations.

The arc length can be expressed as,

$$ds = \rho d\theta \quad (4.13)$$

where ds is the arc length, R is the beam's curvature radius, and $d\theta$ is the change in curvature angle from the starting point to the ending point of the arc. Curvature of the beam is expressed as the reciprocal of the beam's curvature radius,

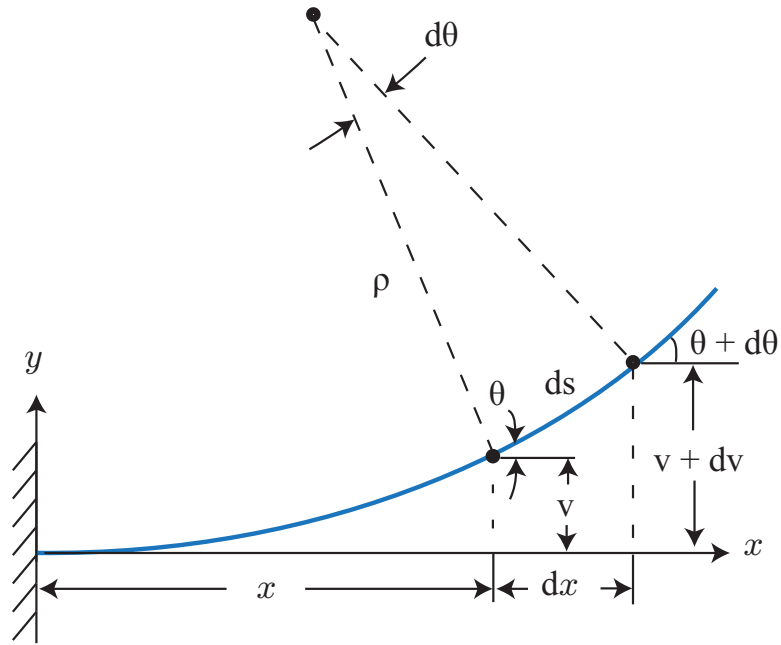


Figure 4.6: Deflected cantilever with variable assignments for dynamic model.

$$\kappa = \frac{1}{\rho} = \frac{d\theta}{dx} \quad (4.14)$$

where κ is the curvature. Further geometric relations result in the slope of the deflection curve given as,

$$\frac{dv}{dx} = \tan \theta \quad (4.15)$$

where θ is the curvature angle and v is the deflection of the beam. Using small angle approximation,

$$\begin{aligned}
ds &\approx dx \\
\kappa &= \frac{1}{\rho} = \frac{d\theta}{dx} \\
\theta &\approx \tan \theta = \frac{d^2v}{dx^2} \\
\frac{d\theta}{dx} &= \frac{d^2v}{dx^2} \\
\kappa &= \frac{d^2v}{dx^2}
\end{aligned} \tag{4.16}$$

simplifications can now be used to utilize Hooke's law for linearly elastic materials. By combining geometric relations, small angle approximation, and Hooke's law, the differential equation for a the deflection curve of a beam is presented,

$$\begin{aligned}
\kappa &= \frac{1}{\rho} = \frac{M}{EI} \\
\frac{d^2v}{dx^2} &= \frac{M}{EI}
\end{aligned} \tag{4.17}$$

where M is the bending moment, E is the modulus of elasticity, and I is the moment of inertia. Taking the derivatives with respect to x , results in relations for both shear force and load,

$$\begin{aligned}
EI \frac{d^3v}{dx^3} &= V \\
EI \frac{d^4v}{dx^4} &= -q
\end{aligned} \tag{4.18}$$

where V is the shear force and q is load. Using the load equation with the transverse force (q) equal to mass time acceleration yields

$$\frac{EI}{\rho A} \frac{\partial^4 v}{\partial x^4} = -\frac{\partial^2 v}{\partial t^2} \tag{4.19}$$

where no lengths are associated with the equation due to the infinitesimally small length scales. Next, the displacement (v) of the beam is expressed as the following

$$v(x, t) = p(t)r(x) \tag{4.20}$$

since displacement of the beam varies with time ($p(t)$) as well as position along the beam ($r(x)$). Substituting 4.20 into 4.19 and separating into functions of time and x yields,

$$-\frac{1}{p(t)} \frac{d^2 p(t)}{dt^2} = \frac{EI}{\rho A} \frac{1}{r(x)} \frac{d^4 r(x)}{dx^4} \quad (4.21)$$

where the functions of time are on the left and functions of x are on the right. For both sides to equal one another, both sides must be equal to a constant and yields the following equations

$$\frac{d^4 r(x)}{dx^4} - \frac{\rho A \omega^2}{EI} r(x) = 0 \quad (4.22)$$

$$\frac{d^2 p(t)}{dt^2} + \omega^2 p(t) = 0 \quad (4.23)$$

where a solution exists for a positive constant (ω^2) and results in the two ordinary homogeneous differential equations above. Next, the displacement variables are nondimensionalized using the following variable,

$$\xi = x/L \quad (4.24)$$

and plugging this nondimensionalized variable into 4.23 yields:

$$\begin{aligned} \frac{d^4 r(x/L)}{L^3 d(x/L)^4} - \frac{\rho A \omega^2 L^4}{EI} L r(x/L) \\ \frac{d^4 r(\xi)}{d\xi^4} - \frac{\rho A \omega^2 L^4}{EI} r(\xi) \\ \beta^4 = \frac{\rho A \omega^2 L^4}{EI}. \end{aligned} \quad (4.25)$$

With the equation above and the following,

$$f = \frac{\omega}{2\pi} = \frac{\beta^2}{2\pi L^2} \sqrt{\frac{EI}{\rho A}} \quad (4.26)$$

the modal frequency (f) is calculated using the eigenvalues for a beam with a clamped - free boundary condition.

Table 4.2: Eigenvalues for a clamped - free cantilever beam.

<i>Mode</i>	Eigenvalue (β)
1	1.875
2	4.694
3	7.855
4	10.996
5	14.137

Table 4.3: Calculated modal frequencies for an equivalent beam model of the multifunctional probe with a constant cross-sectional area throughout.

<i>Mode</i>	Frequency (kHz)
1	41.8
2	262.1
3	734.1
4	1438.6
5	2377.8

Table 4.2 presents the eigenvalues to use with 4.26 for modal frequency calculation. Using a SolidWorks solid model of the multifunctional probe, the volume of the multifunctional probe arm is calculated as $65134 \mu\text{m}^3$. Since the thickness and length of the probe is known, these values are used as the given constraints of a simplified cantilever beam model of the probe. This results in a constant $32.57 \mu\text{m}$ width throughout the length of the beam. The constant width beam simplification allows the use of Eq. (4.26) and the results are presented in Table 4.3. Dynamic modeling is conducted using SolidWorks' linear dynamic FEA study and the results are shown in Fig. 4.7.

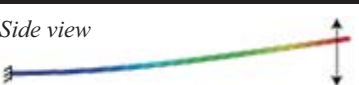
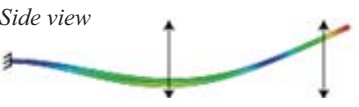
Mode	Mode Shape	Frequency (kHz)
1	<i>Side view</i> 	49.8
2	<i>Side view</i> 	282.3
3	<i>Top view</i> 	333.8

Figure 4.7: Mode shapes and modal frequencies from FEA for non-simplified multifunctional probe.

4.3 Design Tradeoffs

The largest multifunctional probe design hurdle to overcome is to produce a large enough actuation displacement to grasp an AFM modular tip, while stiffening the gripper in the lateral direction to obtain the first two modal shapes of a traditional cantilever beam within the multifunctional probe's design. By increasing the first modal frequency, the probe can be scanned faster across the surface without exciting higher vibrational modes. The multifunctional probe thickness is greater than that of a traditional AFM probe due to fabrication constraints. The main challenge was to reinforce the base of the probe to allow for a traditional cantilever beam first and second modal shapes. Without a wider base, the multifunctional probe has a horizontal side-to-side motion rather than a solely vertical up-down motion as with a traditional cantilever beam. The tapered head design allowed for a lower effective mass for the probe, which pushes the first modal resonance higher. The undesired horizontal side-to-side motion is designed to occur as the third modal shape, where as the second modal shape being the same as a traditional cantilever beam's second modal shape. The frequency is significantly higher for the second and third mode

when compared to the first mode. This was designed so that it would be less likely to excite other modes when nearing the first resonant frequency. However by widening the base of the probe and increasing the side-to-side stiffness, actuation displacement is decreased due to the increased force needed for a given actuation displacement.

4.4 Fabrication

All fabrication was performed at the Nanoscale Research Facility (NRF) at the University of Florida (UFL), which is a class 100-1000 clean room facility. Personal protection clothing is required by the facility and is shown in Fig. 4.8.

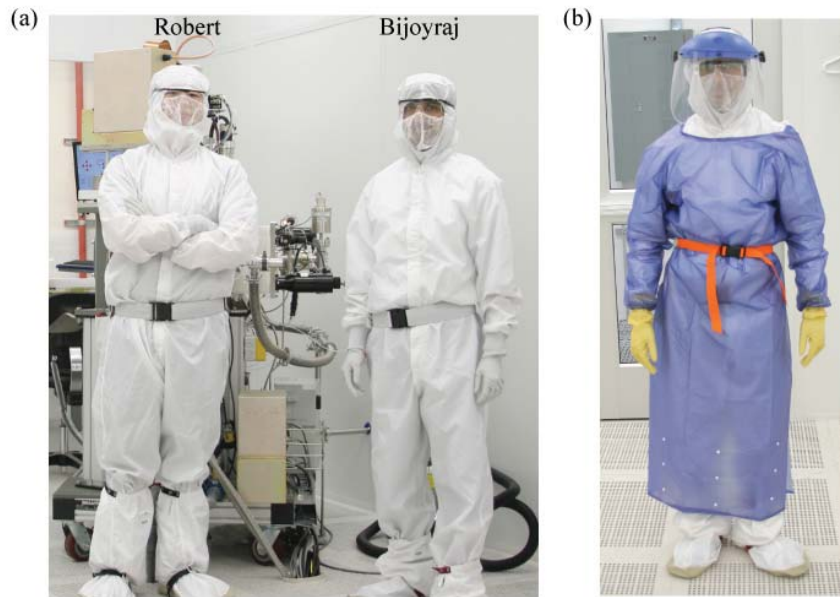


Figure 4.8: Personal protection for University of Florida clean room facility: (a) general protective clothing and (b) wet chemical (acid) protection clothing.

The multifunctional probes are fabricated with conventional surface and bulk micromachining methods using a p-type (boron doped) silicon-on-insulator (pSOI) wafer [118]. Fabrication started with 4 in. SOI wafers (Ultrasil Corporation) with a 5 μm silicon (100) device layer, a 1 μm buried oxide (SiO_2) layer, and a 500 μm

silicon handling layer. A high device layer doping concentration ($> 10^{18}/\text{cm}^3$ resulting in 0.002 to 0.005 $\Omega\text{-cm}$ resistivity) is chosen for its low resistance interface for the electrical contact pads. The photolithography process utilizes three chromium masks (Photo Sciences, California) for patterning the electrical contact pads, device layer, and handling layer. The major fabrication steps are presented in Fig. 4.9 and are categorized into three stages (Stage 1-3). Stage 1 represents processes needed to deposit and etch the aluminum layer, while stage 2 represents the device level etching to machine the multifunctional probe. The last stage (stage 3) represents the processes needed to remove the probe from the supporting wafer.

The fabrication process first starts with a standard RCA cleaning procedure to remove organic and metallic contaminants along with the native oxide layer on the SOI wafer (Fig. 4.9(a)). Next, a 1 μm thick layer of aluminum (Al) is sputtered onto the device layer using a KJL CMS-18 multi-source sputtering system (Fig. 4.9(b)). Material deposition is characterized using a Dektak 150 profilometer. Photolithography is now used to pattern positive photoresist (Shipley 1813) to define the aluminum contact pads. The process starts with spinning a 1.86 μm thick photoresist layer using a Sus Delta 80 spin coater followed by a 2 min soft bake at 110°C to stiffen up the layer before patterning (Fig. 4.9(c)). Next, the photoresist is exposed in a Karl Suss MA6 mask aligner at an intensity of 150 mJ/cm^2 followed by 90 s in AZ 300 MIF developer (Fig. 4.9(d)). The patterned photoresist is now baked in an oven at 105°C for 20 min. After baking, the aluminum is etched using aluminum etchant 80-15-3-2 until the device layer is exposed (Fig. 4.9(e)). The mask is then removed by cleaning in acetone, followed by methanol and de-ionized (DI) water. This concludes the processes for stage 1 and process photos are presented in Fig. 4.10.

Figure 4.10(a) shows the entire sputter coating machine. The silicon wafer is loaded from the side chamber that is shown in more detail in Fig. 4.10(b). After load

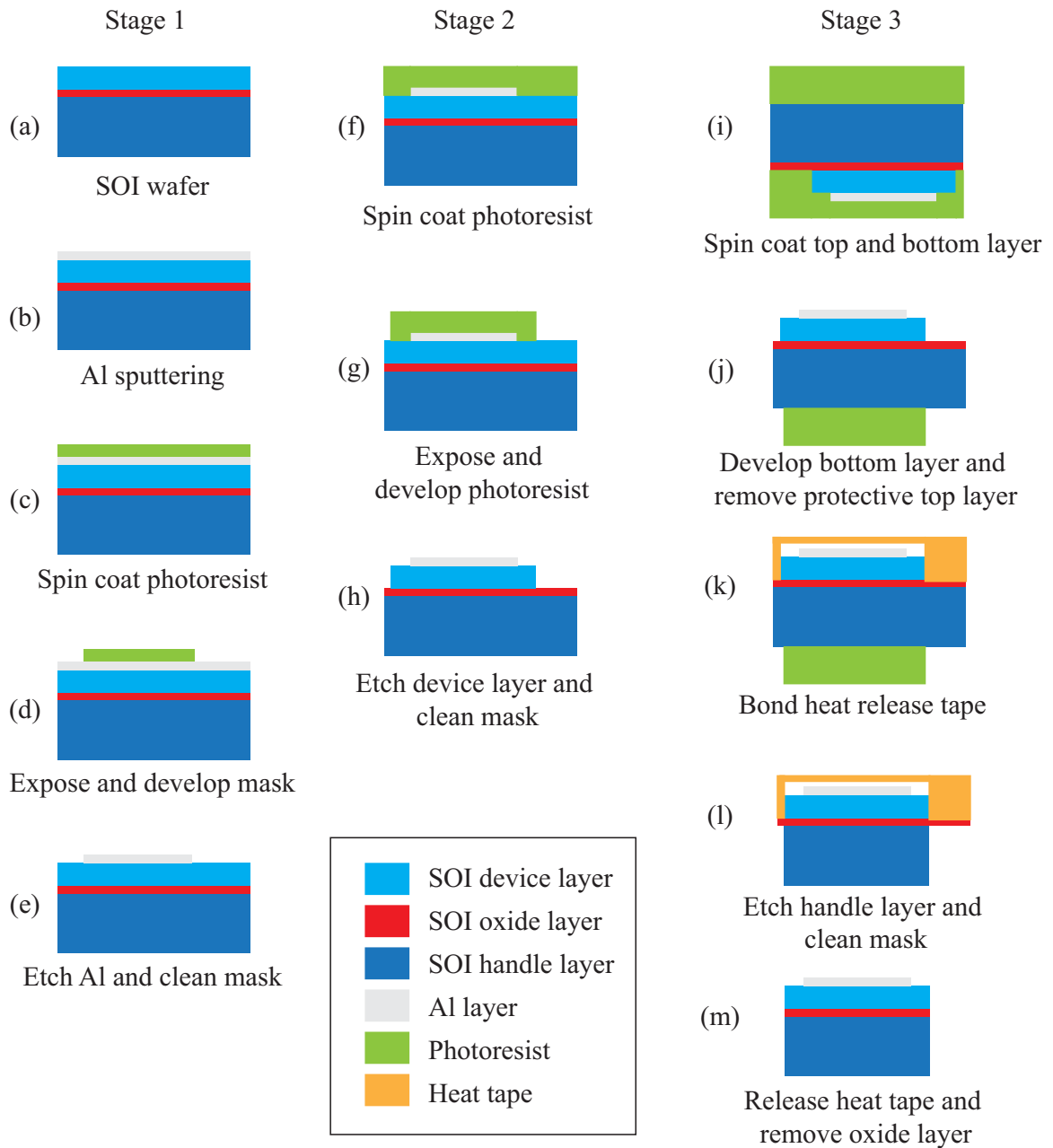


Figure 4.9: Fabrication process for multifunctional probe.

the wafer, it is transferred to the vacuum chamber located in the center of the machine where the sputter process occurs. Figure 4.10(c) presents the spin coating area where the photoresist liquid is coated onto the wafer. A more detailed photo is presented in Fig. 4.10(d) where the photoresist (red liquid) is placed on the wafer, which is held

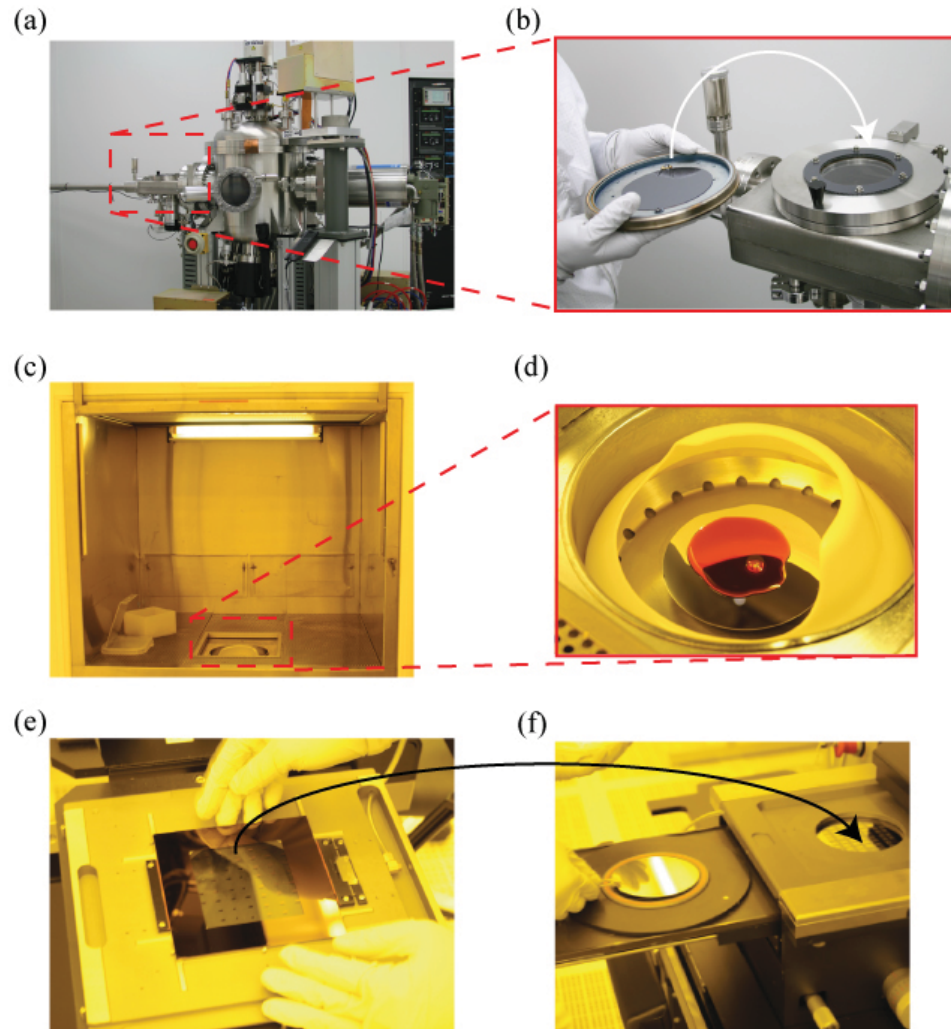


Figure 4.10: Fabrication photos for photolithography process (mask): (a) and (b) Al sputter coating, (c) and (d) Photoresist spin coating, and (e) and (f) mask transfer.

down using a vacuum platform, and rotated to evenly distribute the liquid over the wafer. Rotation speed, photoresist liquid selection, and rotation duration all play factors into the thickness of the photoresist layer. Lastly in Fig. 4.10(e) and 4.10(f), the mask is transferred to the photoresist layer using the mask aligner pictured. The mask is placed onto a transparent vacuum table as shown in Fig. 4.10(e). The vacuum table is then placed onto the mask aligner, where the wafer with a photoresist layer is slid in underneath the mask. The mask is then expose to light and the mask transfers

the image onto the photoresist layer, where areas are either hardened or softened under exposure to the light.

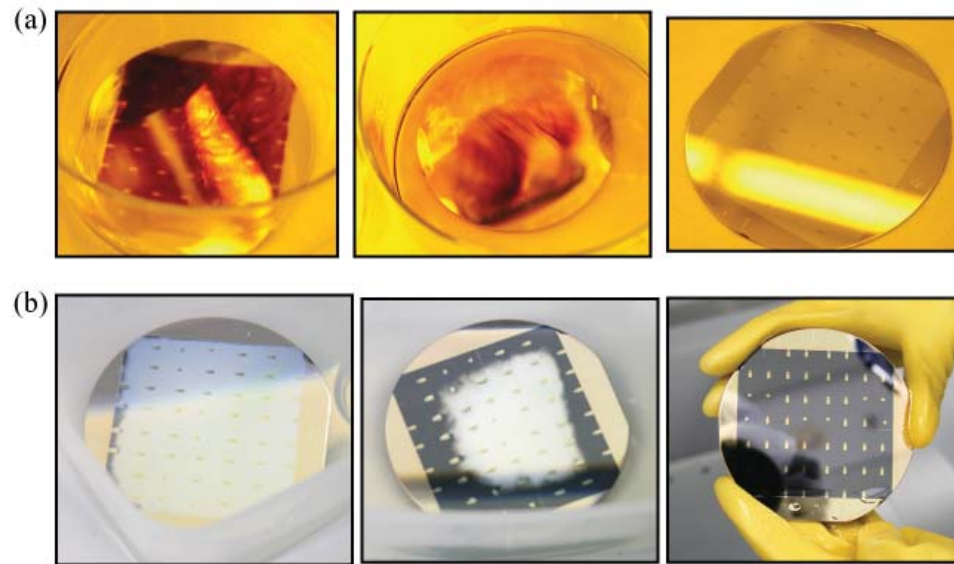


Figure 4.11: Fabrication photos for photolithography process (etching): (a) and (b) photoresist layer is developed and (c) and (d) aluminum layer is etched.

Figure 4.11(a) shows the progression of the mask development from left to right. The developer (AZ 300 MIF) removes the photoresist that was uncovered by the mask leaving behind the covered areas where aluminum is not to be removed. Figure 4.11(b) shows the aluminum etching progression from left to right as the wafer with the developed mask (Fig. 4.11(a)) is placed into the aluminum etching solution (aluminum etchant 80-15-3-2). After the process is completed, the silver-metallic areas are the aluminum contact pads, while the dark areas are the exposed silicon wafer (device layer).

The same photolithography steps are repeated to define the multifunctional probe and probe support patterns on the device layer (Fig. 4.9(f)-(g)). The device layer is etched by deep reactive ion etching (DRIE) using a STS DRIE system until the buried oxide layer is exposed (Fig. 4.9(h)). The photoresist is removed using the

same procedure as previously discussed. Then, the wafer is cleaned in oxygen plasma (O_2 gas flow = 300 sccm at 600 W) in a Anatech Barrel SCE600 asher for 15 min. This concludes the processes for stage 2, but before proceeding to the handle layer processing the device-side is protected with a $1.86 \mu\text{m}$ thick S1813 positive photoresist layer that is soft baked at 110°C for 2 min followed by a flood exposure in Karl Suss MA6 mask aligner for 4 min.

For stage 3 processes, the wafer is rotated, such that the back-side is now upward. A $12 \mu\text{m}$ thick positive photoresist AZ 9260 is spun on the back-side and then soft baked at 110°C for 3 min. An EVG model 620 aligner is used to align the top-side features to the back-side features and exposure is carried out at $1850 \text{ mJ}/\text{cm}^2$. The photoresist is then placed in AZ 300 MIF developer for 400 s followed by a post bake at 105°C for 30 min. During this processes, the top-side protective photoresist layer is removed. Next, the SOI wafer is bonded to a $500 \mu\text{m}$ thick support wafer using a Nitto Denko Revalpha heat release tape with the heat-sensitive side of the tap bonded to the device layer of the SOI wafer. Then, the handle layer is etched in the STS DRIE system until the buried oxide layer is exposed.

Now, the SOI wafer along with the support wafer is diced in an Advanced Dicing Technologies (ADT) dicer for separating the individual devices.

Figure 4.12 provides photos for the DRIE and dicing fabrication processes completed at UFL. Figure 4.12(a) shows the carrier structure that transports the wafer into the DRIE chamber, while Fig. 4.12(b) is a partial photo of the DRIE machine because the remainder of the machine is enclosed behind the wall in the back. Figure 4.12(c) shows the etching completed by the DRIE machine, where the green color is the oxide layer of the SOI wafer. Figure 4.12(d) shows the wafer mounted onto a larger support for the dicing machine (Fig. 4.12(e)). The dicing machine creates cutting trajectories from user provided coordinates to cut the wafer into smaller pieces

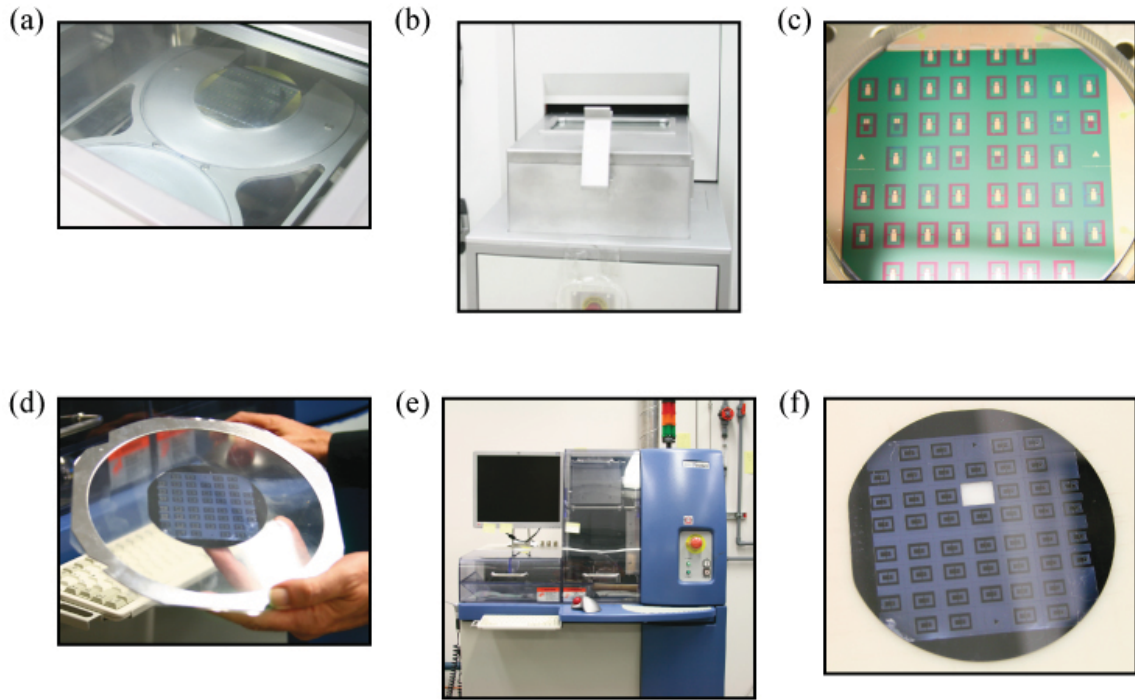


Figure 4.12: Fabrication photos for: (a)-(c) deep reactive ion etching and (d)-(f) dicing

that have only a single multifunctional probe. An example of a cut wafer is shown in Fig. 4.12(f), where a single probe is removed from the wafer. The individual devices are heated on a hot plate at 170°C in order to release the SOI wafer from the support wafer that was bonded with the heat release tape. The photoresist on the handle layer is removed in PG remover (Micro Chem) followed by iso-propanol and DI water. Next, the individual probe chips are released by etching the buried oxide layer in 777 Etch (Fujifilm) for 40-60 min. The 777 Etch is chosen to reduce the etching effect on the aluminum contact pads as well as reduce the contamination and staining on the probes. Scanning electron microscopy (SEM) images of the fabricated probes is presented in Fig. 4.13.

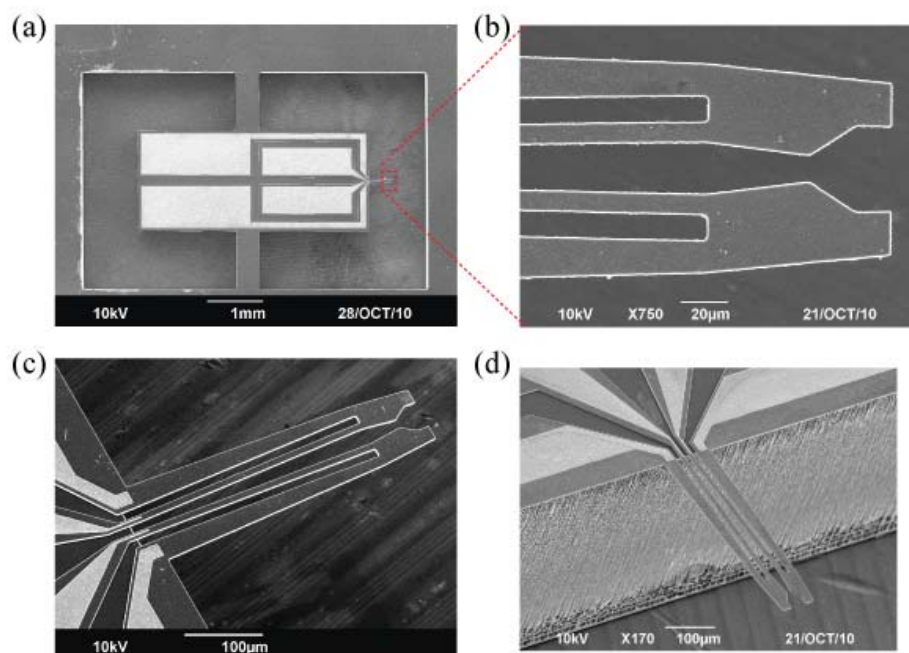


Figure 4.13: Scanning electron microscopy images of fabricated multifunctional probes with the following views: (a) overview of released probe with support structure, (b) zoomed in on probe gripper end, (c) angled view 1, and (d) angled view 2.

4.4.1 Fabrication Challenges

Fabricating the multifunctional probes is a time consuming and learning experience. All fabrication processes required characterizing each piece of equipment to ensure proper feature tolerances. General process recipes were provided by the engineers at the nanofabrication facility; however, many adjustments had to be made to the final process recipes. The first few iterations of the fabrication plan only produced inoperable probes and the processes needed more refinement. After several months and numerous trials, the fabrication processes were dialed in and produced functional probes. The final fabrication process was presented above and is the result of a lengthy characterization process, experienced staff knowledge of the nanofabrication system, and the fabrication efforts of Bijoyraj Sahu at UFL.

Chapter 5

ETM Actuator Characterization

This section will present experimental results that characterize the ETM actuator's dynamic response as well as its electrical response. The dynamic response results will provide information on the probe's modal frequencies. The electrical response results provide the operating range that should be used for consistent results. The electrical response also suggest how fast the probe can actuate given its input. Lastly, displacement measurements are provided to characterize the deflection of the actuator under various inputs.

5.1 Dynamic Response

The dynamic response is performed on the custom AFM platform that was developed earlier. The probe is fixed to the cantilever mount on the AFM and actuated using the piezoelectric actuator on the vertical axis (z -axis). The change in tip displacement is monitored using the AFM's photodetector. A Stanford Research Systems SR785 dynamic signal analyzer (DSA) performs a swept sine analysis of the cantilever from 1 kHz to 100 kHz using a 5-mV amplitude input signal to the piezoelectric amplifier. Results from the analysis is presented in Fig. 5.1.

Frequency response data for the AFM stage (G1) and the multifunctional probe (G3) are gathered; however the multifunctional probe response data has the AFM

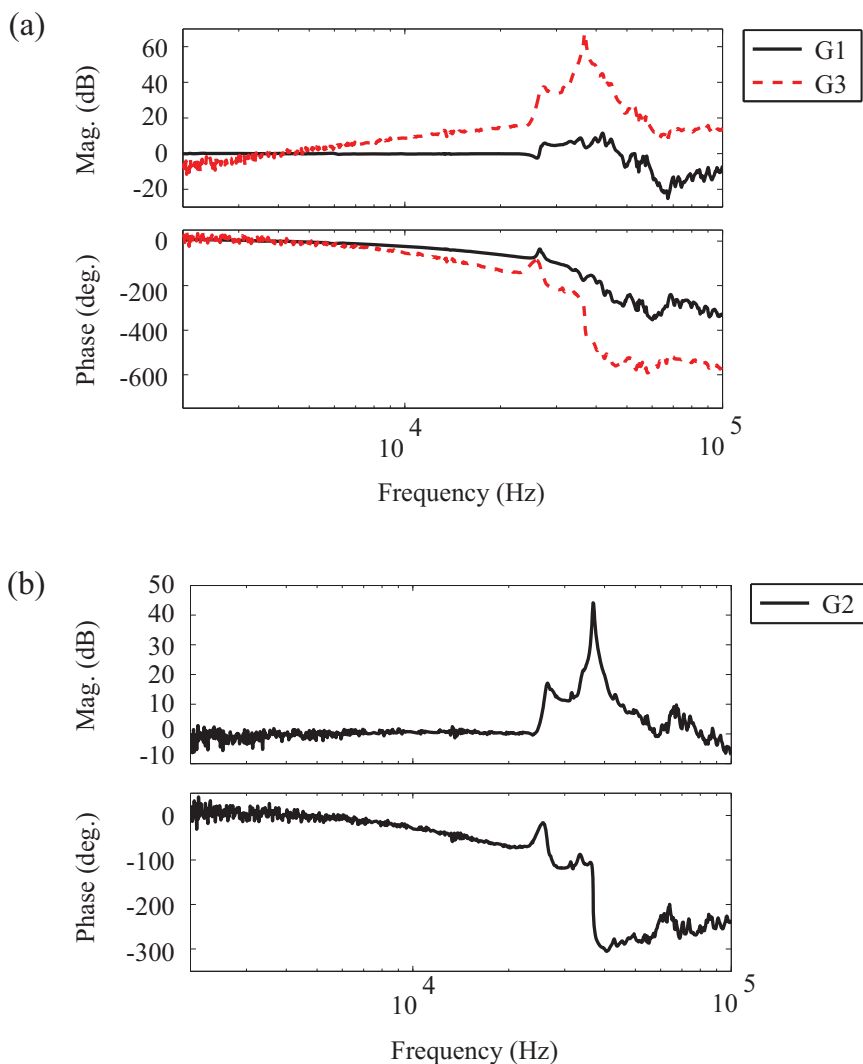


Figure 5.1: Dynamic response data for: (a) AFM stage using a laser vibrometer (G1) and multifunctional probe using the AFM's photodetector (G3) and (b) the calculated multifunctional probe response.

stage's dynamics coupled inside of the signal because the probe is mounted on top of the AFM stage, which means that the stage dynamics have a direct impact on the probe's dynamics. To decouple the two systems, the AFM stage dynamics is subtracted from the probe's dynamics. This is accomplished by using the frequency response data, which contains both magnitude and phase information by utilizing complex numbers. The data is recorded in the following format

$$\begin{aligned}
a_1 + b_1 i \\
a_2 + b_2 i \\
a_3 + b_3 i
\end{aligned}
\tag{5.1}$$

where a 's and b 's subscripts correspond to the data shown in Fig. 5.1. The $G2$ frequency response is calculated by the following

$$\begin{aligned}
a_2 &= \frac{b_3 - a_1 b_2}{b_1} \\
b_2 &= \frac{a_1 b_3 - a_3 b_1}{b_1^2 + a_1^2}
\end{aligned}
\tag{5.2}$$

where a_2 and b_2 are calculated for Fig. 5.1(b). The figure shows a resonant peak at 36.8 kHz, which is 5 kHz below the simplified model's results and 10 kHz below the FEA predicted value of 47.0 kHz. It is also noted that before the resonant peak, a smaller peak is evident around 27 kHz, which is also seen in the frequency response of the stage. An explanation for this peak to occur even when removing the stage dynamics from the probe's dynamics is that because the multifunctional probe is a cantilevered beam, the displacement amplitude of the base is amplified down the length of the beam. This leads to a greater displacement at the distal end of the probe compared to the base of the probe. The difference between predicted and experimental resonant peak value is addressed in Chapter 6.

5.2 Electrical Characterization

The electrical characterization process includes the following tasks:

1. Provide mean and standard deviation of peak current consumption
2. Investigate time response trends of current consumption for actuation
3. Determine current response repeatability over 10 actuations
4. Determine steady state actuation displacements and provide a linear operating range
5. Demonstrate pick and place capability of the multifunctional probe

Electrical characterization is carried out using custom circuitry along with a LabVIEW data acquisition program coupled with a National Instruments PCI-6221 data acquisition board and custom multifunctional probe power circuitry. The custom circuitry utilizes OPA211 operational amplifiers that are selected for their low noise, wide bandwidth, low offset voltage, and small package size. The operational amplifiers are used as buffers to take the output from the data acquisition card and power the multifunctional probe as well as transmit current flow information. The custom circuitry is used for the input to the probe in order to ensure that only a limited amount of current will flow to the probe thus eliminating possible stray currents from the data acquisition system. To measure the current flow through the probe a resistor is connected to the end of the probe circuit as well as to ground. This provides a voltage drop across a known resistance, where current calculations can be made (voltage divider circuit). Similar noise reducing techniques as in the photodetector (PSD) circuit are used here along with additional capacitors and large circuit traces. The probe powering and current measuring circuitry is shown in Fig. 5.2.

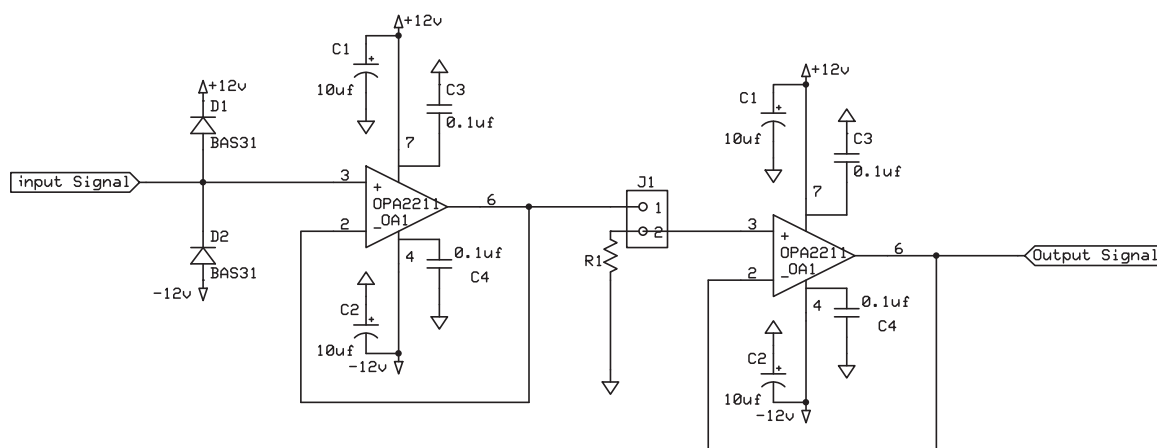


Figure 5.2: Multifunctional probe power and current measuring circuit.

Experiments are conducted with a 10 kHz sampling rate, which is greater than 10 times faster than the 5% settling time of the multifunctional probe's electrical response for a 10 V input. The fast sampling time is chosen to capture the fast current rise during the start of the test when the probe has the lowest resistance (no thermal resistance changes). Faster sampling times are not consistent using the capabilities of the current desktop computer. The results shown in this section will include time response data for current consumption and maximum operational frequency calculation using settling time measurements. For electrical connections to the probe, gold wire bonds connected to the probe's aluminum pads using silver die attach epoxy as shown in Fig. 5.3. To cure the epoxy, the probe with bonded wires is placed in an oven at 320°F for 2 hours. The gold wire (0.002-in. diameter) provides a low resistance, high flexible interface to the circuit, where vibrations can be mitigated. The gold wire is then soldered to solid-core hookup wire before being connected to the custom powering circuitry.

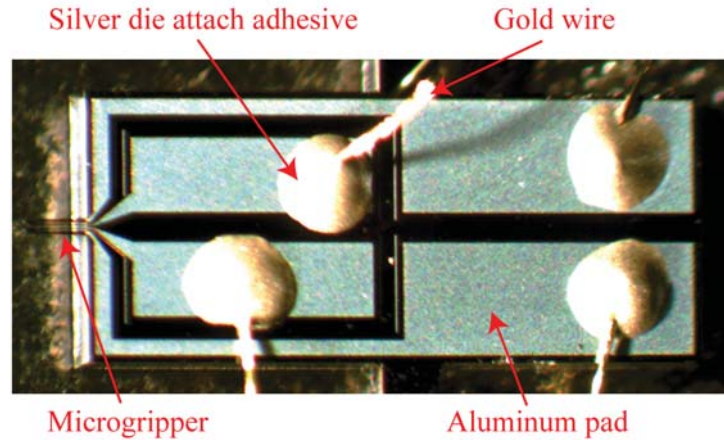


Figure 5.3: Gold wire bonds from multifunctional probe chip out to circuit.

Figure 5.4 provides an overview to the probe's operational characteristics. Actuator 1 has a measured resistance of 840Ω , while actuator 2 has a measured resistance of 780Ω . Resistance measurements are taken with a Hewlett Packard 34401A multi-meter at room temperature. It is shown that for low inputs ($< 5 \text{ V}$) the two gripper arms operate very closely to one another; however, above 5 V the time responses start to vary. Above 10 V input, consistency between actuation runs vary widely as seen by the increase in standard deviation. The plots suggest that if the two gripping arms have similar resistance (within 10%) the current time response will be similar, but operating above a 5 V input will result in inconsistency between the two actuators. Furthermore if the grippers are driven above 10 V , the actuators' electrical response will vary greatly.

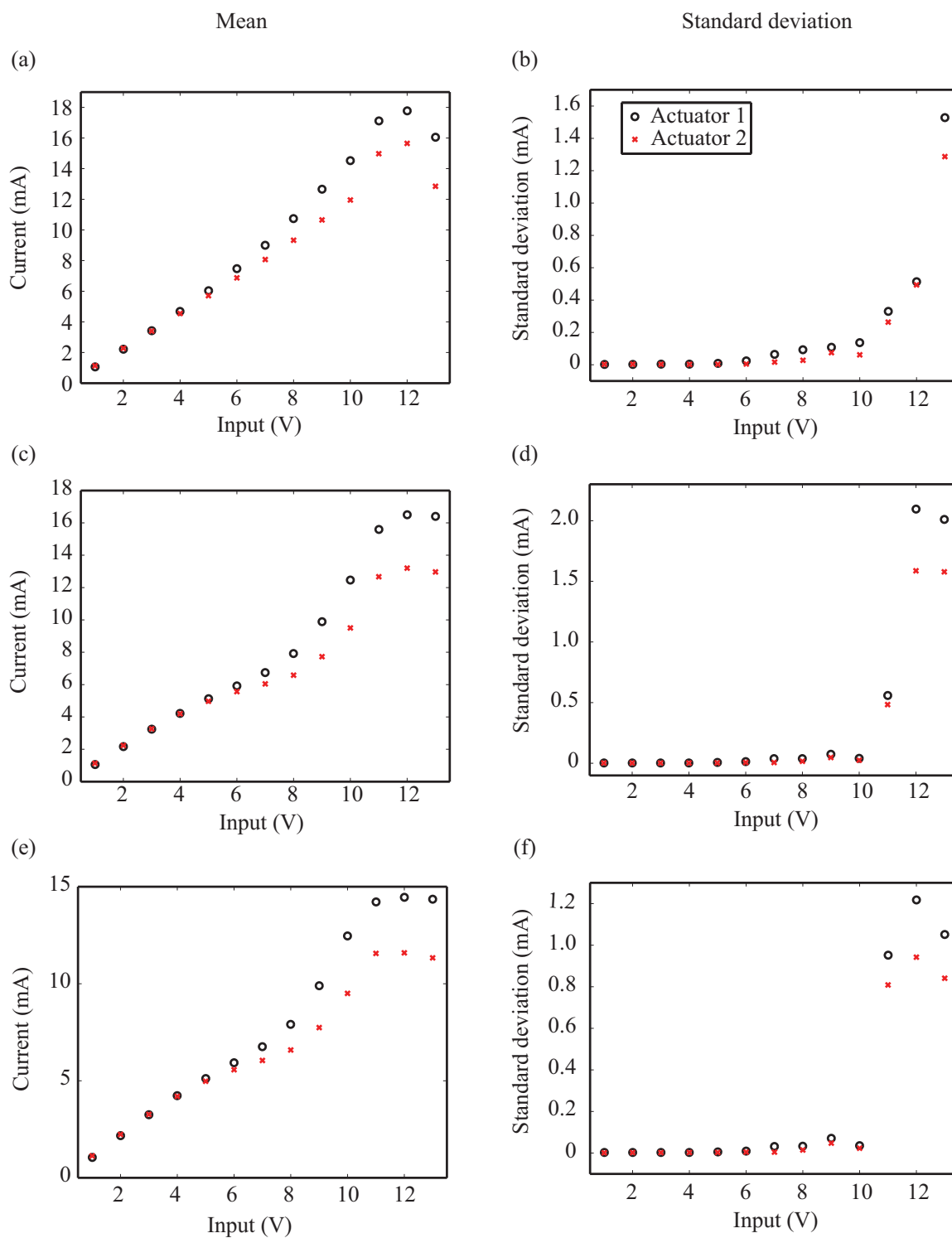


Figure 5.4: Multifunctional probe mean current flow throughout and standard deviation from 1 to 13 V input voltages during: (a) and (b) 1st actuation, (c) and (d) 5th actuation, and (e) and (f) 10th actuation. Tests are performed with a 1-Hz square wave.

Figure 5.5 provides current consumption information with respect to time. The plots show that with the exception of the Fig. 5.5(a) and 5.5(b), an initial spike in current is observed, which quickly settles to a steady state value. In Fig. 5.5(a) and 5.5(b), the resolution of the data acquisition system prevent capturing the effect as seen in Fig. 5.5(c)-(l). It is also observed that in Fig. 5.5(i)-(l) a sharp drop is seen after the initial current spike and before reaching a steady state current value. The sharp drop along with the initial current spike can be explained by the heating of the multifunctional probe as current flows through it. Initially the probe is at room temperature and current flows through at a high rate (the spike in current flow). This high density flow rate through the hot arm causes it to heat up and thereby increase its resistance, which results in a sharp decreasing current when the voltage input is held constant (sharp decrease after the current spike). The current decrease below steady state in Fig. 5.5(i)-(l) is due to the probe's arm being heated above the steady state temperature that causes a below steady state current value. As the probe cools due to the decrease in resistance, the probe's arm is able to slowly increase current flow back up to a steady state value. The 5% settling time for 10 V input is 0.0034 s, which translates to a 294 Hz maximum operating frequency. On the other hand, operating at a conservative 5 V results in a 0.0015 s 5% settling time (667 Hz maximum operating frequency).

Next, the electrical current time response data across ten actuations is plotted to show the variations in current with respect to time. Ten time locations are chosen throughout the actuation duration, where the first actuation takes place when the input signal is sent to the probe up to 0.45 s into the constant voltage input actuation. The plots show that the data remains tightly distributed around the mean value throughout the trials and the total variation remains under 1% of current mean value.

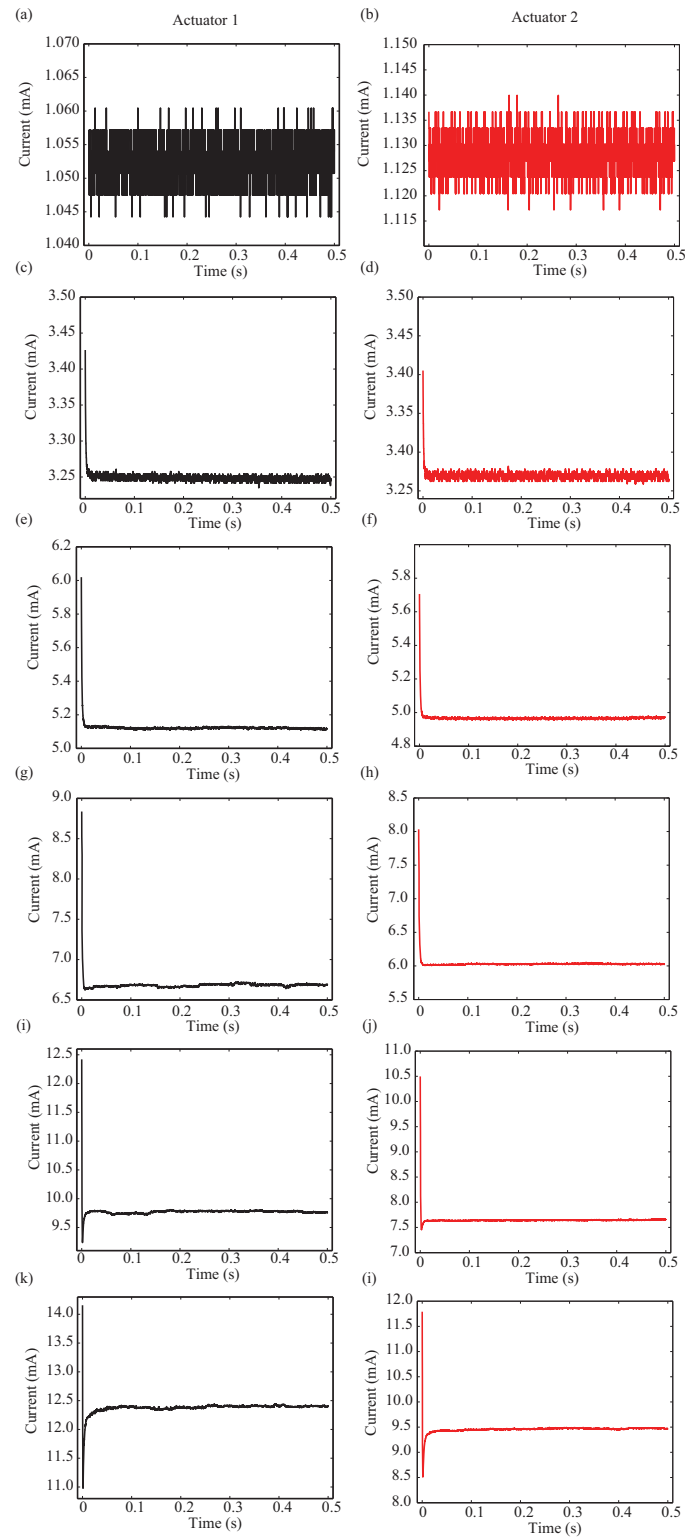


Figure 5.5: Current time response data for the following input voltages: (a) and (b) 1 V, (c) and (d) 3 V, (e) and (f) 5 V, (g) and (h) 7 V, (i) and (j) 9 V, and (k) and (l) 10 V. Tests are performed with a 1 Hz square wave.

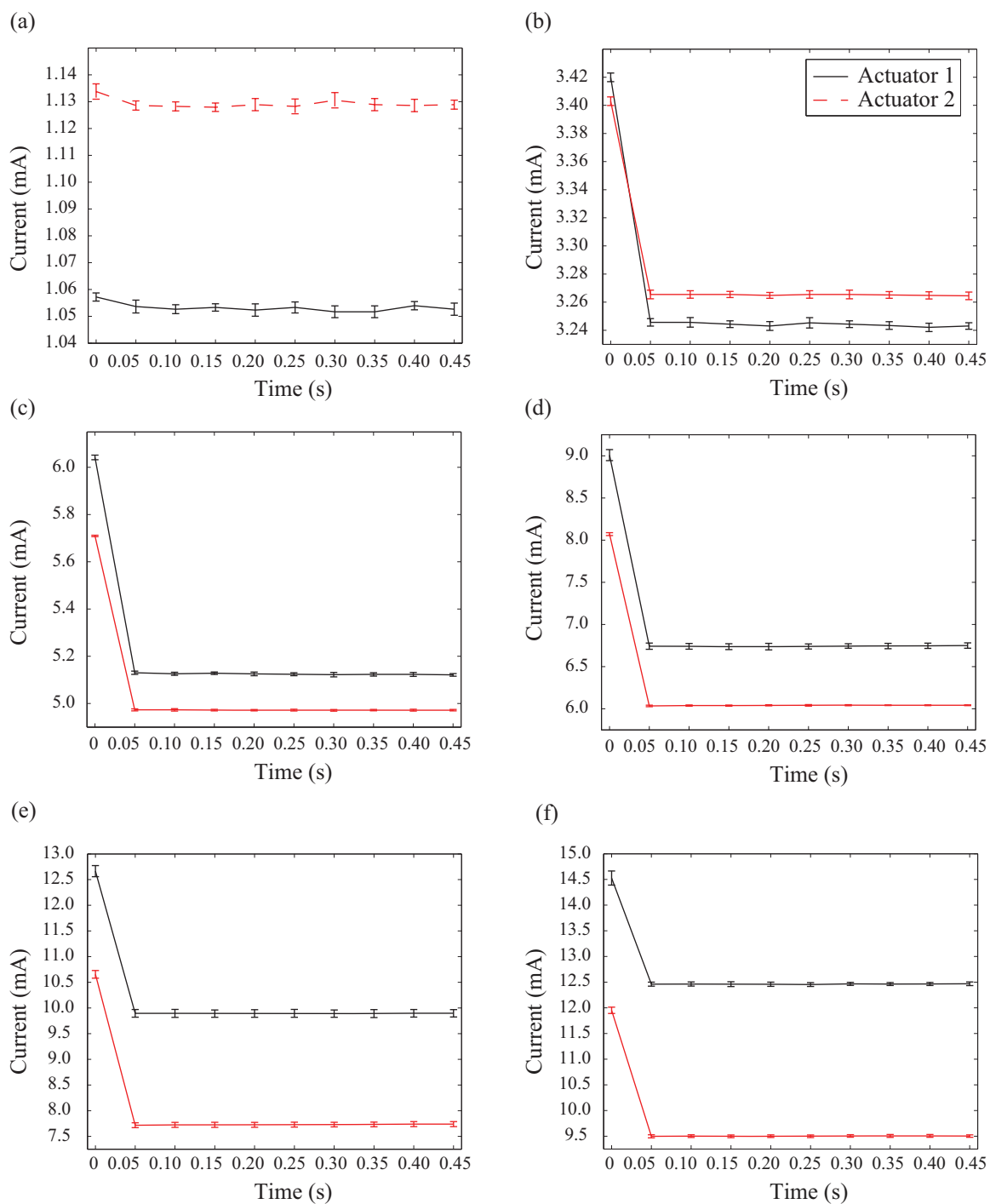


Figure 5.6: Time response current data with standard deviation bars plotted for the following input voltages: (a) 1 V, (b) 3 V, (c) 5 V, (d) 7 V, (e) 9 V, and (f) 10 V. Tests are performed with a 1-Hz square wave.

Finally by using the time response data and known input values, probe resistance changes throughout time are found as shown in Fig. 5.7.

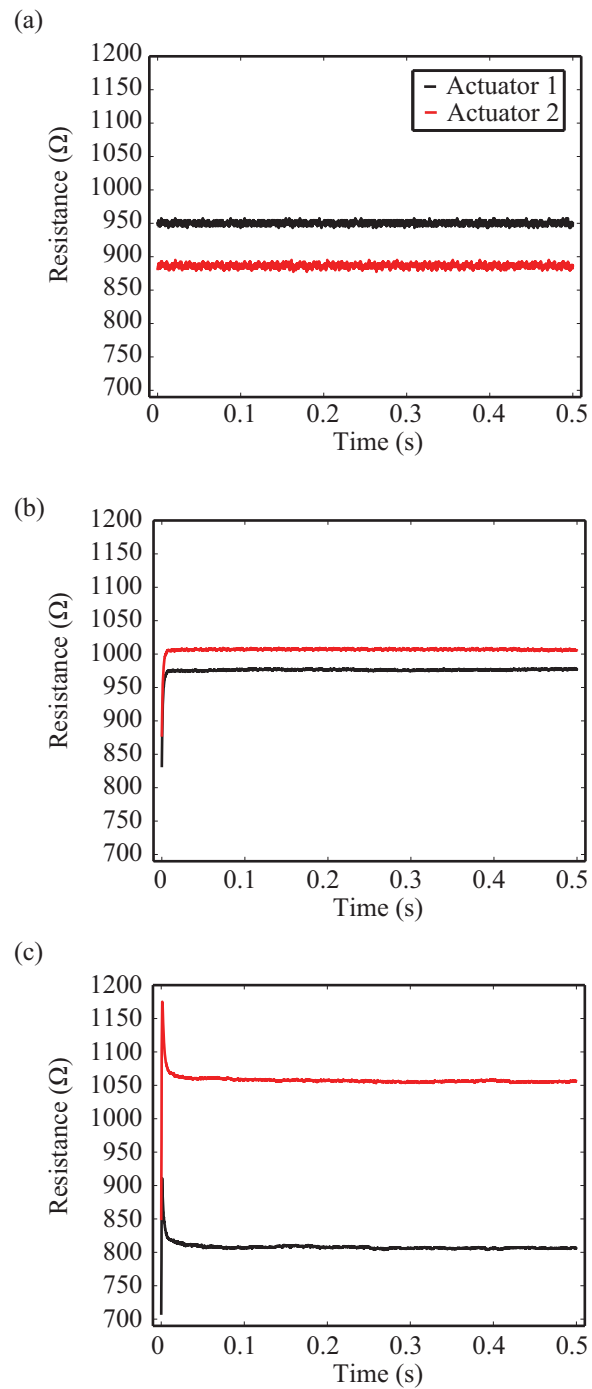


Figure 5.7: Time response resistance changes for the multifunctional probe for: (a) 1 V input, (b) 5 V input, and (c) 10 V input.

5.3 Displacement Characterization

Displacement measurements are gathered from optical microscope images (Nikon Optiphot). The images are taken with an Allied Technologies Guppy GF146C digital video camera with a 1392×1040 pixel resolution. Using optical microscope calibration grids, relative displacement measurements utilized by pixel counting and approximations to the total displacement of the multifunctional probe can be achieved. Approximate pixel count for a $10 \mu\text{m}$ displacement under 20-times optical magnification is 45 pixels. This is the basis for all of the displacement measurements. Figure 5.8 are frames taken from the digital video camera with the background removed and superimposed onto one another. The displacement is calculated by using the same pixel counting technique used for the calibration sample. In Fig. 5.8(a), the multifunctional probe is driven with a 5 V input (approximately 5-mA steady state current), which results in a $2.0 \mu\text{m}$ displacement.

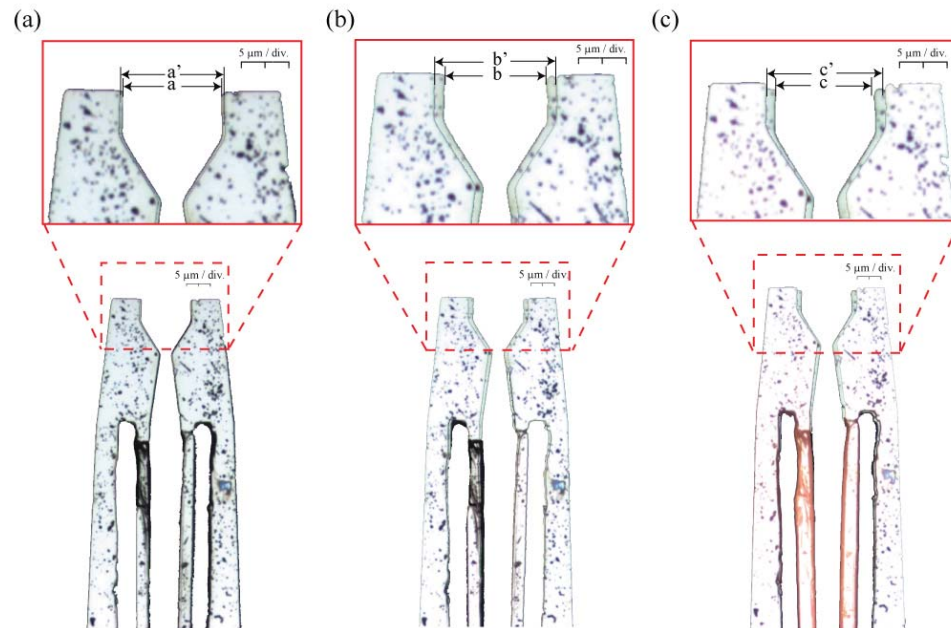


Figure 5.8: Multifunctional probe actuation under various driving voltages: (a) 5 V, (b) 10 V, and (c) 13 V.

This is close to the calculated $2.28\mu\text{m}$ displacement (5.5-mA input) calculated using the ETM model in section 4.1. Increasing the voltage up to 10 V, the gripper produces $6.4\mu\text{m}$ of displacement and is shown in Fig. 5.8(b). The reported values are steady state displacements due to the slow capture frame rate of the video recording system (approximately 4 frames per second at highest resolution). Apply too much voltage results in what is shown in Fig. 5.8(c). While the displacement remains comparable to a 10V driving voltage, the hot arms of both actuators are seen glowing red. Note that no color enhancements or photo post-processing is used on this figure. Also note that the dark spots on the probe's arms is debris from operating the probes in a academic research lab (not a cleanroom).

Additional tests are conducted from 0.5 V input to 13 V inputs. From 0.5 V to 2.0 V, the results are discarded due the optical resolution limit of an optical microscope. In such cases, the measurement errors are greater than the perceived displacements and are therefore unreliable. Data from these additional tests are presented in Fig. 5.9(a).

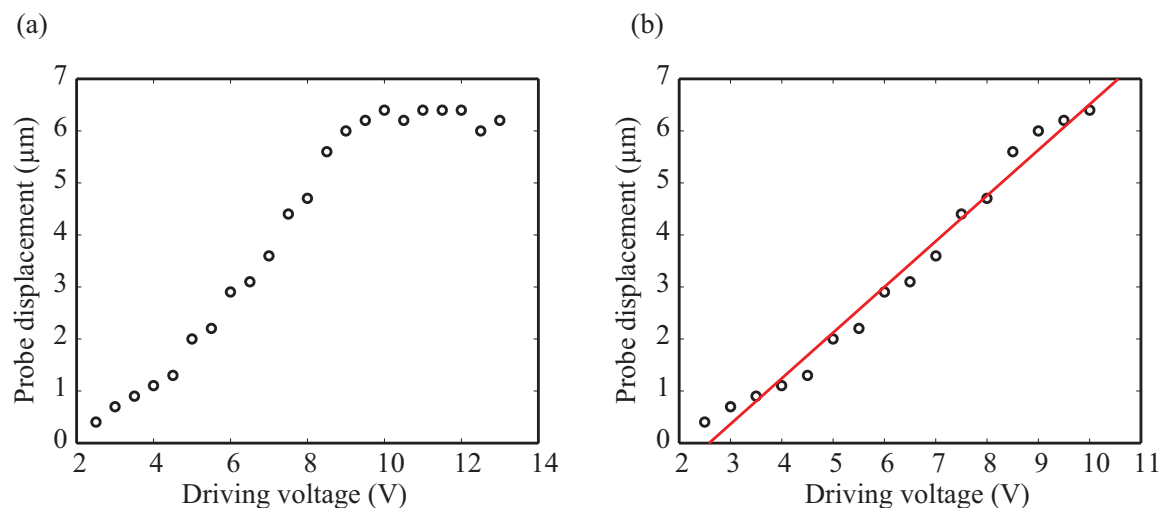


Figure 5.9: Plot of probe actuation displacements under various input voltages: (a) measured data and (b) 'linear' operating range with linear fit.

Above 10 V input, the driving circuitry can not supply enough current (30 mA max.) to actuated the multifunctional probe while maintaining a constant input voltage resulting in decreasing input voltages with time. For the range from 2.5 V to 10 V, the data shows a linearly increasing trend with increasing input voltages. Figure 5.9(b) provides a linear fit line in red and shows that most of the data follows the general increasing trend described by the equation below

$$y = 0.877x - 2.26 \quad (5.3)$$

where x is the driving voltage and y is the gripper displacement in microns. By driving the gripper under excessive currents/voltages (> 10 V), physical deformation occurs and gripper discoloration becomes apparent. Over time, the excessive loads lead to gripper actuation failure by creating an open circuit condition of the gripper arm circuit due to separation of gripper hot arm.

5.4 Application

This section demonstrates the multifunctional probe's ability to grasp an object (wire), move it, and release it. The experimental setup for this section is shown in Fig. 5.10.

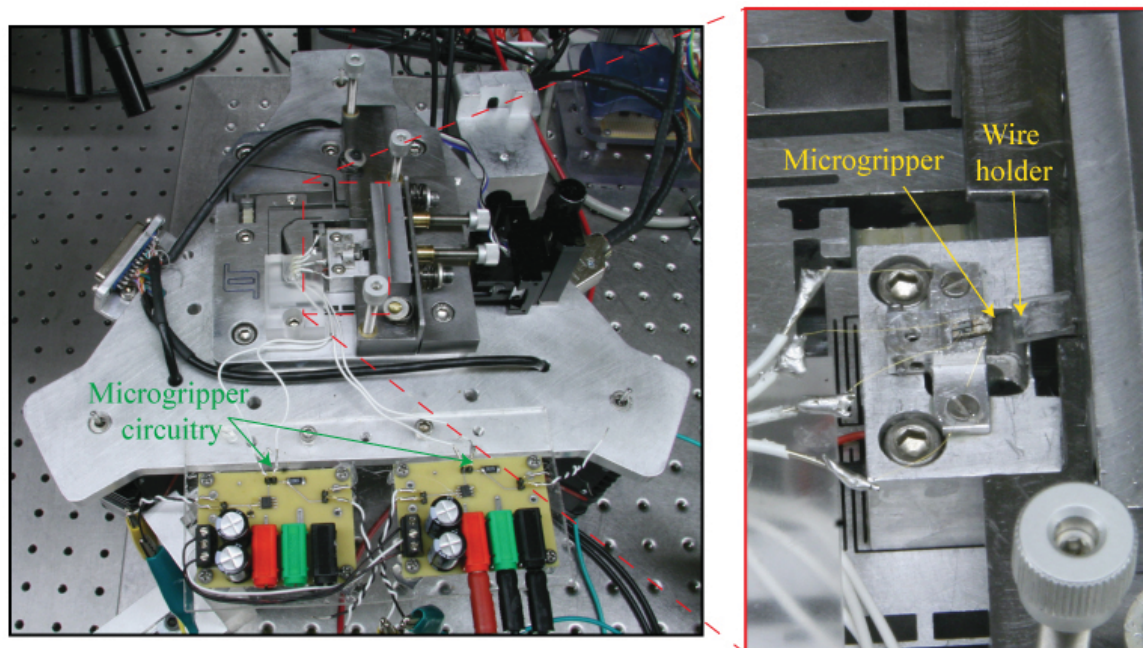


Figure 5.10: Experimental setup for demonstrating the multifunctional probe's gripping ability.

The setup utilizes the AFM platform's nanopositioner for precise x , y , and z translation, while coarse translation is accomplished using a coarse translational stage that is shown mounted on top of the AFM's nanopositioner. Translation on the coarse stage is achieved using fine-pitch adjustment screws that provide 0.254 mm of displacement per revolution. Using five adjustment screws, six degrees of freedom is accomplished by placing three screws on the top for z -axis displacement along with x and y -axis rotation. The two screws on the right side of the coarse translation stage provide x and y displacement with z -axis rotation. The adjustment screws are adjusted by hand and provides large, coarse movements to bring the object within the multifunctional probe's reach. Using the nanopositioning stage with LabVIEW interface along with the coarse adjustment stage, an optical microscope, and custom probe circuitry, Figure 5.11 demonstrates the probe's ability to grasp a section of wire at various angles.

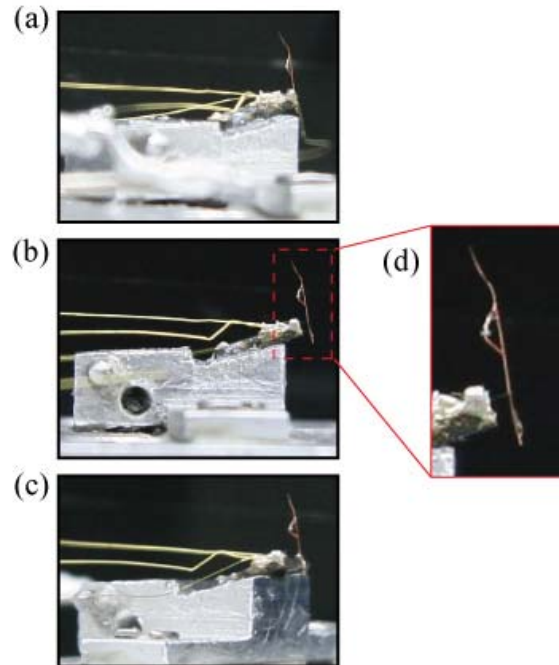


Figure 5.11: Demonstration of wire gripping ability at various angles: (a) back angled side view, (b) side view, (c) front angled side view, and (d) zoomed in side view.

The wire in the figure is composed of two wires that are bonded together using adhesive. The reason behind this is that the top wire is etched to a fine point and the wire on the bottom is a non-modified 47 AWG enamel coated wire. The wire is approximately $37 \mu\text{m}$ in diameter, which is larger than the non-actuated gripper dimension yet small enough to fit in between the actuated gripper arms. Pick and place results are shown in Fig. 5.12, where a wire is picked up, translated to a new location, and released.

Figure 5.12(a) shows the probe being moved into place to grasp the wire with time progressing from top to bottom. The first photo shows a zoomed out view that shows the probe (left), wire (center), and wire base (right). The second photo down shows a zoomed in view of the first photo. From the second to third photo, the wire is moved using the coarse translation platform shown in Figure 5.10. From the third to

last photo in Fig. 5.12(a), the probe is moved using the nanopositioning stage on the AFM to precisely orient the gripper's arms in order to grasp the wire. Figure 5.12(b) shows the probe's fully supporting the wire and releasing the wire. The first photo on the top is a zoomed out photo showing the gripper fully supporting the wire with the coarse translation platform fully retracted. The second photo is a zoomed in picture showing the probe's actuating arms grasping the wire and supporting the wire. In the third photo down, the probe is actuated to release the wire along with moving the nanopositioning stage quickly to facilitate the wire's release. The last photo shows the multifunctional probe after releasing the wire, where no physical damage is evident through the above process. This verifies the system's ability to grasp an object (wire), translate it, and release it at a new location.

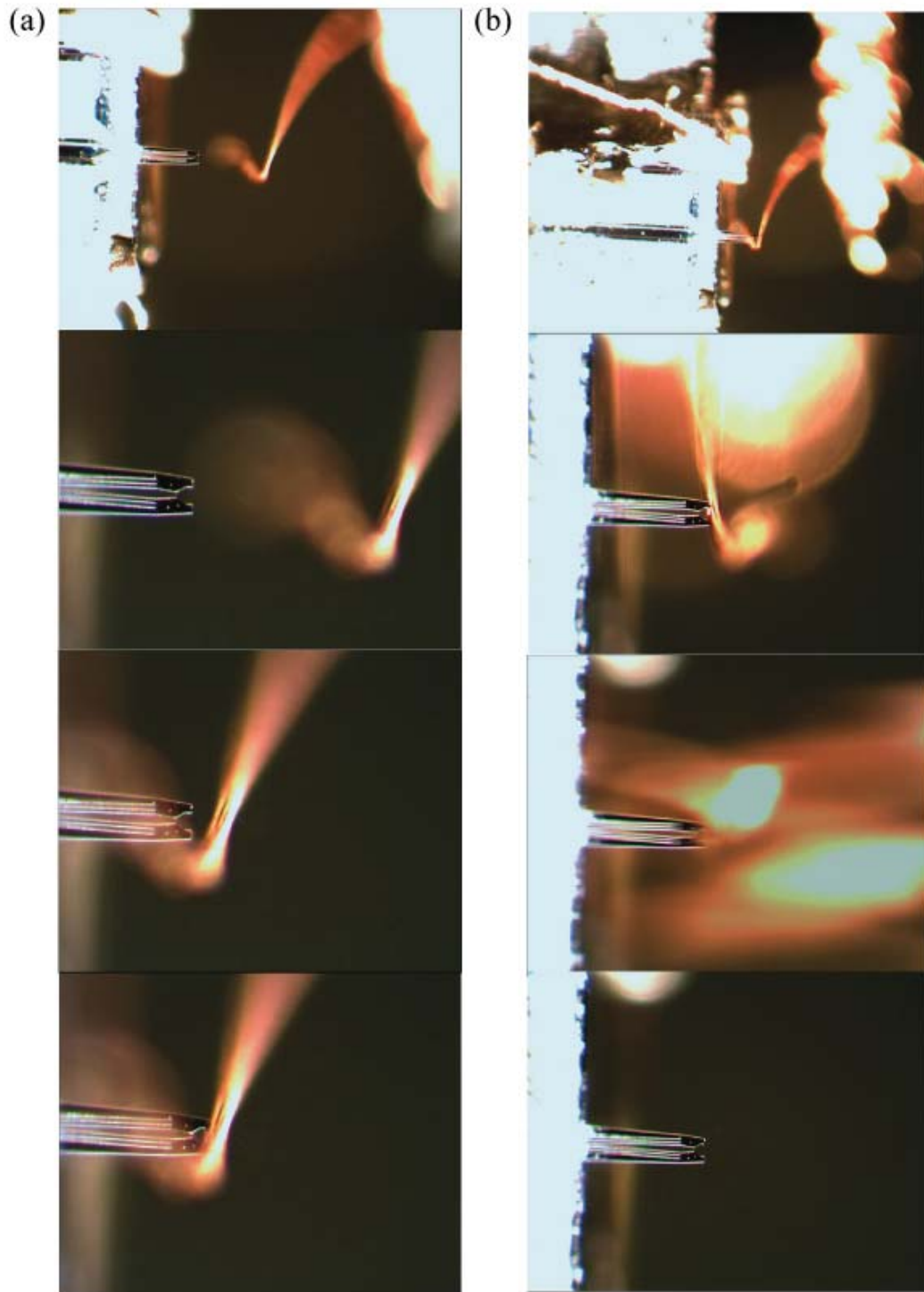


Figure 5.12: Demonstration of probe's pick and place capability with time progression from top to bottom of: (a) probe's grasping capability and (b) probe's translation and releasing capability.

Chapter 6

Discussion

AFM is a powerful tool at the nanoscale; however, throughput greatly hinders the effectiveness of its strengths. The AFM probe is the only consumable part of the system, yet it has the greatest impact on image quality as well as fabrication capability. The process of discarding a worn or fouled tip takes only seconds, but to replace the probe with associated recalibration tasks result in several minutes of down time for an experienced AFM operator. In an effort to streamline the process, the cantilevered beam support structure of the AFM probe is reused and only the worn or fouled tip is replaced. This drastically reduces the down time associated with replacing an entire AFM probe (cantilever beam and tip) by eliminating the recalibration process. A multifunctional probe is designed, fabricated, and characterized to facilitate the implementation of it into a automated system that will greatly increase throughput in both AFM-based imaging and nanofabrication. The designed probe exploits the thermal expansion mismatch between two cantilevered beam joined at the distal end for actuation displacement. Thermal expansion actuation is chosen for its low power requirements, since the probe will be used in conjunction with electrically sensitive equipment. The multifunctional probe utilizes a passive gripping mechanism to grasp the interchangeable tip for imaging or fabrication. The probe will maintain a gripping force on the tip to properly secure it when operating; however it will not need to be powered during this process due to the passive gripping mechanism. Using

an active gripper mechanism would require continuously driving current through the probe, which could create an electrical short circuit when the tip comes into contact with a conductive sample, but the effectiveness of the probe (actuation displacement) decreases with increasing actuation duration, which limits long duration activation. The probe is able to achieve up to $6.4\ \mu\text{m}$ of total displacement (using both actuators), which is more than sufficient for grasping objects as shown in Fig. 5.11 and 5.12.

Electrical characterization is conducted to investigate the consistency of the probe's electrical response under various inputs and explore actuation repeatability. A 5 V maximum driving voltage is suggested to maintain actuator displacement consistency among actuations as shown in Fig. 5.5. On the other hand if a single large actuation displacement is desired, applying a 10 V driving voltage will result in the greatest displacement and increasing the driving voltage beyond 10 V will only result in decrease the probe's actuation ability as shown in Fig. 5.9. An ETM actuation model is created to estimate the anticipated probe displacement under 5.5 mA of current (reaches maximum temperature at this current). Two models are created: one model with an averaged temperature throughout and another model utilizing the estimated temperature distribution. The averaged temperature model over predicted the displacement of the probe by approximately $0.28\ \mu\text{m}$; however, the temperature distributed model underestimated the probe deflection by $0.66\ \mu\text{m}$. The averaged temperature model is less valid since it assumes an constant temperature throughout the hot arm and another constant temperature throughout the cold arm which is not possible given the boundary conditions. The temperature distributed model provides a more realistic model even though the deflection is less accurate because it utilizes the boundary conditions. The increase in deflection approximation error can be attributed to several parameters that incorporated averaged values throughout the modeled 300 K to 800 K range.

To ensure that the designed multifunctional probe will operate similarly to a traditional AFM probe, design and characterization also focused on its dynamic response. The geometric layout of the designed probe incorporates a taper beam design with a larger cross-sectional area at the base that tapers to a smaller cross-sectional area at the distal tip end. By widening the width of the base and still maintaining a narrow tip width, the lateral stiffness is increased resulting in traditional cantilever beam mode shapes for the first two modal shapes. FEA predicted a first modal frequency of 47.0 kHz, which is 10.2 kHz higher than the measured 36.8 kHz first modal frequency. A reasonable explanation for the error is that the frequency response tests have been performed on a probe that has actuated many times at high driving voltages ($> 10 V$). The actuation of the probe reduces the stiffness (modulus of elasticity) of the silicon by possibly fracturing the material decreases the resonant frequency of a beam as shown in Eq. (4.26). Another reason for the lower measured frequency could be the added layer of debris on the cantilever, which will add to the mass and ultimately lower increase its effective mass. This added layer of debris is due to the non-clean room environment it was operated in. However, the measured first modal frequency is still higher than a typical contact mode AFM probe, so the imaging capability of the probe is still promising.

The custom AFM platform utilizes a nanopositioner [50] that provides over $40 \mu\text{m}$ of scan range in both the x and y -axis, while keeping cross-coupling effects below 2% from x to y and y to x as shown in Fig. 3.21. A custom z -axis probe holder is also fabricated to provide z -axis control with over $7 \mu\text{m}$ of actuation displacement while imaging. The z -axis controller is a microcontroller that performs PI control and allows the AFM to be operated in constant force and constant height contact mode imaging. Fig. 3.24, 3.25, and 3.26 provide verification of imaging capabilities of the system. Models of the x , y , and z axes (Eqs. (3.7), (3.8), and (3.9)) are created

and compared to measured frequency response data (Fig. 3.20 and 3.23) for future reference. The custom AFM operation is validated and is ready to serve as a platform for the future nanofabrication system.

Chapter 7

Conclusions and Future Work

In conclusion, this thesis presented the design, model, analysis, and fabrication of an active electro-thermal microcantilever along with the design, fabrication, characterization, and validation of a scanning probe microscopy platform. The custom AFM provides a platform to facilitate cantilever characterization as well as a vehicle for future system integration. By incorporating cantilever holder with z -axis control, the platform can fully function as an AFM for imaging as well nanomachining processes. The microcantilever test results presented in this document show that while large displacements ($6.4 \mu\text{m}$ at 10 V input) are desirable, the irreversible damage caused by high current densities and inconsistencies between actuations leads to limiting the operating voltages to maximum of 5 V , where $2 \mu\text{m}$ of actuation displacement is achievable. Traditional cantilever beam dynamics are mimicked using a tapered-beam design structure for the multifunctional probe and a dynamic response similar to a traditional AFM probe is attained, which allows the designed probe to be utilized in the same manner as a AFM probe (*i.e.*, imaging, machining, etc...). Future work includes design and fabrication of specialized tips for the designed multifunctional probe. With custom tips, the probe will be able to more securely grasp and maintain control of the tip throughout various tasks. Sensing will also need to be addressed for the automated nanofabrication system along with custom programming modifications for the AFM program. Additional work can also include incorporating control for the

x and y axes to increase AFM's throughput and precision by compensating for the piezoelectric actuator nonlinearities.

Bibliography

- [1] “Nanosurf - basic afm package,” <http://www.nanosurf.com/>.
- [2] “Schaefer group,” <http://www.schaefer-tec.com/>.
- [3] K. Andersen, D. Petersen, K. Carlson, K. Molhave, O. Sardan, A. Horsewell, V. Eichhorn, S. Fatikow, and P. Boggild, “Multimodal electrothermal silicon microgrippers for nanotube manipulation,” *Nanotechnology, IEEE Transactions on*, vol. 8, no. 1, pp. 76–85, 2009.
- [4] O. Sardan, V. Eichhorn, D. Petersen, S. Fatikow, O. Sigmund, and P. Boggild, “Rapid prototyping of nanotube-based devices using topology-optimized microgrippers,” *Nanotechnology*, vol. 19, no. 49, p. 495503, 2008.
- [5] T. C. Duc, G.-K. Lau, and P. M. Sarro, “Polymeric thermal microactuator with embedded silicon skeleton: Part ii;fabrication, characterization, and application for 2-dof microgripper,” *Microelectromechanical Systems, Journal of*, vol. 17, no. 4, pp. 823–831, 2008.
- [6] F. Krecinic, T. Duc, G. Lau, and P. Sarro, “Finite element modelling and experimental characterization of an electro-thermally actuated silicon-polymer micro gripper,” *Journal of Micromechanics and Microengineering*, vol. 18, no. 6, 2008.
- [7] C. Thelander and L. Samuelson, “Afm manipulation of carbon nanotubes: realization of ultra-fine nanoelectrodes,” *Nanotechnology*, vol. 13, no. 1, pp. 108–113, 2002.
- [8] F. Te-Hua and et al., “Machining characterization of the nano-lithography process using atomic force microscopy,” *Nanotechnology*, vol. 11, no. 3, p. 181, 2000.
- [9] B. Bhushan, “Nano- to microscale wear and mechanical characterization using scanning probe microscopy,” *Wear*, vol. 251, no. 1-12, pp. 1105–1123, 2001.
- [10] E. Delawski and B. Parkinson, “Layer-by-layer etching of 2-dimensional metal chalcogenides with the atomic force microscope,” *Journal of the American Chemical Society*, vol. 114, no. 5, pp. 1661–1667, 1992.

- [11] D. Croft, G. Shed, and S. Devasia, “Creep, hysteresis, and vibration compensation for piezoactuators: Atomic force microscopy application,” *Journal of Dynamic Systems, Measurement, and Control*, vol. 123, no. 1, pp. 35–43, 2001.
- [12] S. Devasia, E. Eleftheriou, and S. O. R. Moheimani, “A survey of control issues in nanopositioning,” *IEEE Transactions on Control Systems Technology*, vol. 15, no. 5, pp. 802–823, 2007.
- [13] G. M. Clayton, S. Tien, K. K. Leang, Q. Z. Zou, and S. Devasia, “A review of feedforward control approaches in nanopositioning for high-speed spm,” *Journal of Dynamic Systems Measurement and Control-Transactions of the Asme*, vol. 131, no. 6, 2009.
- [14] K. Nakano, “Three-dimensional beam tracking for optical lever detection in atomic force microscopy,” *Review of Scientific Instruments*, vol. 71, no. 1, pp. 137–141, 2000.
- [15] S. K. Hung and L. C. Fu, “Novel three-dimensional beam tracking system for stationary-sample-type atomic force microscopy,” *Instrumentation and Measurement, IEEE Transactions on*, vol. 55, no. 5, pp. 1648–1654, 2006.
- [16] P. K. Hansma, B. Drake, D. Grigg, C. B. Prater, F. Yashar, G. Gurley, V. Elings, S. Feinstein, and R. Lal, “A new, optical-lever based atomic force microscope,” *Journal of Applied Physics*, vol. 76, no. 2, pp. 796–799, 1994.
- [17] P. S. Jung and D. R. Yaniv, “Novel stationary-sample atomic force microscope with beam-tracking lens,” *Electronics Letters*, vol. 29, no. 3, pp. 264–266, 1993.
- [18] K. Carlson, K. Andersen, V. Eichhorn, D. Petersen, K. Molhave, I. Bu, K. Teo, W. Milne, S. Fatikow, and P. Boggild, “A carbon nanofibre scanning probe assembled using an electrothermal microgripper,” *Nanotechnology*, vol. 18, no. 34, p. 345501, 2007.
- [19] R. T. R. Kumar, S. Hassan, O. S. Sukas, V. Eichhorn, F. Krohs, S. Fatkow, and P. Boggild, “Nanobits: customizable scanning probe tips,” *Nanotechnology*, vol. 20, no. 39, p. 395703, 2009.
- [20] A. Ivanisevic and C. Mirkin, ““dip-pen” nanolithography on semiconductor surfaces,” *Journal of the American Chemical Society*, vol. 123, no. 32, pp. 7887–7889, 2001.
- [21] B. Cappella and G. Dietler, “Force-distance curves by atomic force microscopy,” *Surface Science Reports*, vol. 34, no. 1-3, pp. 1–104, 1999.
- [22] H. G. Hansma, D. E. Laney, M. Bezanilla, R. Sinsheimer, and P. Hansma, “Applications for atomic-force microscopy of dna,” *Biophysical Journal*, vol. 68, no. 5, pp. 1672–1677, 1995.

- [23] Q. Tang, S. Shi, and L. Zhou, "Nanofabrication with atomic force microscopy," *Journal of Nanoscience and Nanotechnology*, vol. 4, no. 8, pp. 948–963, 2004.
- [24] M. Tello and R. Garcia, "Nano-oxidation of silicon surfaces: Comparison of non-contact and contact atomic-force microscopy methods," *Applied Physics Letters*, vol. 79, no. 3, pp. 424–426, 2001.
- [25] R. Barrett and C. F. Quate, "High-speed, large-scale imaging with the atomic force microscope," *Journal of Vacuum Science and Technology B*, vol. 9, no. 2, pp. 302–306, 1991.
- [26] S. Decossas, F. Mazen, T. Baron, G. Bremond, and A. Souifi, "Atomic force microscopy nanomanipulation of silicon nanocrystals for nanodevice fabrication," *Nanotechnology*, vol. 14, no. 12, pp. 1272–1278, 2003.
- [27] C. R. Taylor, E. A. Stach, G. Salamo, and A. P. Malshe, "Nanoscale dislocation patterning by ultralow load indentation," *Applied Physics Letters*, vol. 87, no. 7, pp. 073 108–073 108–3, 2005.
- [28] H. Hansma, "Atomic force microscopy of biomolecules," *Journal of Vacuum Science and Technology B*, vol. 14, no. 2, pp. 1390–1394, 1996.
- [29] Y. L. Lyubchenko and L. S. Shlyakhtenko, "Visualization of supercoiled dna with atomic force microscopy in situ," *Proceedings of the National Academy of Sciences of the United States of America*, vol. 94, no. 2, pp. 496–501, 1997.
- [30] U. Kunze, "Nanoscale devices fabricated by dynamic ploughing with an atomic force microscope," *Superlattices and Microstructures*, vol. 31, no. 1, pp. 3–17, 2002.
- [31] J. Zhang, G. Li, and N. Xi, "Modeling and control of active end effector for the afm based nano robotic manipulators," in *Robotics and Automation, 2005. ICRA 2005. Proceedings of the 2005 IEEE International Conference on*, 2005, pp. 163–168.
- [32] S. Li and C. Liu, "Mems arrayed scanning probes for soft nanolithography," in *Chemical Sensors 7 -and- MEMS/NEMS 7 - 210th Electrochemical Society Meeting, October 29, 2006 - November 3, 2006*, ser. ECS Transactions, vol. 3. Electrochemical Society Inc., 2006, pp. 463–472.
- [33] Y.-S. Kim, H.-J. Nam, S.-M. Cho, J.-W. Hong, D.-C. Kim, and J. U. Bu, "Pzt cantilever array integrated with piezoresistor sensor for high speed parallel operation of afm," ser. Sensors and Actuators, A: Physical, vol. 103. Elsevier, 2003, pp. 122–129.
- [34] S. Minne, G. Yaralioglu, S. Manalis, J. Adams, J. Zesch, A. Atalar, and C. Quate, "Automated parallel high-speed atomic force microscopy," *Applied Physics Letters*, vol. 72, no. Compendex, pp. 2340–2340, 1998.

- [35] K. Salaita, Y. Wang, J. Fragala, R. A. Vega, C. Liu, and C. A. Mirkin, "Massively parallel dippen nanolithography with 55000-pen two-dimensional arrays," *Angewandte Chemie International Edition*, vol. 45, no. 43, pp. 7220–7223, 2006.
- [36] P. Vettiger, G. Cross, M. Despont, U. Drechsler, U. Durig, B. Gotsmann, W. Haberle, M. Lantz, H. Rothuizen, R. Stutz, and G. Binnig, "The "millipede"-nanotechnology entering data storage," *IEEE Transactions on Nanotechnology*, vol. 1, no. Compendex, pp. 39–54, 2002.
- [37] C. Huh and S. Park, "Atomic force microscope tip-induced anodization of titanium film for nanofabrication of oxide patterns," *Journal of Vacuum Science and Technology B*, vol. 18, no. 1, pp. 55–59, 2000.
- [38] S. Manalis, S. Minne, A. Atalar, and C. Quate, "High-speed atomic force microscopy using an integrated actuator and optical lever detection," *Review of Scientific Instruments*, vol. 67, no. 9, pp. 3294–3297, 1996.
- [39] R. Piner, J. Zhu, F. Xu, S. Hong, and C. Mirkin, "'dip-pen" nanolithography," *Science*, vol. 283, no. 5402, pp. 661–663, 1999.
- [40] I. Rangelow, "Scanning proximity probes for nanoscience and nanofabrication," *Microelectronic Engineering*, vol. 83, no. 4-9, pp. 1449–1455, 2006.
- [41] E. Snow, P. Campbell, and F. K. Perkins, "Nanofabrication with proximal probes," *Proceedings of the IEEE*, vol. 85, no. 4, pp. 601–611, 1997.
- [42] S. Minne, S. Manalis, and C. Quate, "Parallel atomic force microscopy using cantilevers with integrated piezoresistive sensors and integrated piezoelectric actuators," *Applied Physics Letters*, vol. 67, no. 26, pp. 3918–3920, 1995.
- [43] C. Kim, A. Pisano, and R. Muller, "Silicon-processed overhanging microgripper," *Microelectromechanical Systems, Journal of*, vol. 1, no. 1, pp. 31–36, 1992.
- [44] J. Jonsmann, O. Sigmund, and S. Bouwstra, "Compliant electro-thermal microactuators," in *Proceedings of the 1999 12th IEEE International Conference on Micro Electro Mechanical Systems, MEMS, January 17, 1999 - January 21, 1999*, ser. Proceedings of the IEEE Micro Electro Mechanical Systems (MEMS). IEEE, 1999, pp. 588–593.
- [45] K. Kakushima, M. Mita, D. Kobayashi, G. Hashiguchi, J. Endo, Y. Wada, and H. Fujita, "Micromachined tools for nano technology -twin nano-probes and nano-scale gap control by integrated microactuators," in *14th IEEE International Conference on Micro Electro Mechanical Systems (MEMS 2001), January 21, 2001 - January 25, 2001*, ser. Proceedings of the IEEE Micro Electro Mechanical Systems (MEMS). Institute of Electrical and Electronics Engineers Inc., 2001, pp. 294–297.

- [46] S. Takeuchi and I. Shimoyama, "Three dimensional sma microelectrodes with clipping structure for insect neural recording," in *Proceedings of the 1999 12th IEEE International Conference on Micro Electro Mechanical Systems, MEMS, January 17, 1999 - January 21, 1999*, ser. Proceedings of the IEEE Micro Electro Mechanical Systems (MEMS). IEEE, 1999, pp. 464–469.
- [47] K. Molhave, T. Wich, A. Kortschack, and P. Boggild, "Pick-and-place nanomanipulation using microfabricated grippers," *Nanotechnology*, vol. 17, no. 10, pp. 2434–2441, 2006.
- [48] C. Liu, *Foundations of MEMS*. Upper Saddle River, New Jersey: Prentice Hall, 2006.
- [49] C. Keller and R. Howe, "Hexsil tweezers for teleoperated micro-assembly," in *Micro Electro Mechanical Systems, 1997. MEMS '97, Proceedings, IEEE., Tenth Annual International Workshop on*, 1997, pp. 72–77.
- [50] B. J. Kenton, "Design, characterization, and control of a high-bandwidth serial-kinematic nanopositioning stage for scanning probe microscopy applications," Master's thesis, University of Nevada, Reno, 2010.
- [51] G. Binnig, H. Rohrer, C. Gerber, and E. Weibel, "Surface studies by scanning tunneling microscopy," *Physical Review Letters*, vol. 49, no. 1, pp. 57–61, 1982.
- [52] G. Binnig, C. F. Quate, and C. Gerber, "Atomic force microscope," *Physical Review Letters*, vol. 56, no. 9, p. 930, 1986.
- [53] G. Meyer and N. M. Amer, "Novel optical approach to atomic force microscopy," *Applied Physics Letters*, vol. 53, no. 12, pp. 1045–1047, 1988.
- [54] J. Ruan and B. Bhushan, "Atomic-scale friction measurements using friction force microscopy .1. general-principles and new measurement techniques," *Journal of Tribology-Transactions of the Asme*, vol. 116, no. 2, pp. 378–388, 1994.
- [55] M. Shusteff, T. P. Burg, and S. R. Manalis, "Measuring boltzmann's constant with a low-cost atomic force microscope: An undergraduate experiment," *American Journal of Physics*, vol. 74, no. 10, pp. 873–879, 2006.
- [56] C. N. Jones and J. Goncalves, "A cost-effective atomic force microscope for undergraduate control laboratories," *IEEE Transactions on Education*, vol. 53, no. 2, pp. 328–334, 2010.
- [57] F. Kuhner, R. A. Lugmaier, S. Mihatsch, and H. E. Gaub, "Print your atomic force microscope," *Review of Scientific Instruments*, vol. 78, no. 7, p. 075105, 2007.

- [58] Y. K. Yong, B. Ahmed, and S. O. R. Moheimani, "Atomic force microscopy with a 12-electrode piezoelectric tube scanner," *Review of Scientific Instruments*, vol. 81, no. 3, pp. 033701–10, 2010.
- [59] B. J. Furman, J. Christman, M. Kearny, F. Wojcik, and M. Tortonese, "Battery-operated atomic force microscope," *Review of Scientific Instruments*, vol. 69, no. 1, pp. 215–220, 1998.
- [60] F. G. Bosco, E. T. Hwu, S. Keller, A. Greve, and A. Boisen, "Self-aligned cantilever positioning for on-substrate measurements using dvd pickup head," *Microelectronic Engineering*, vol. 87, no. 5–8, pp. 708–711, 2010.
- [61] T. Albrecht, S. Akamine, T. Carver, and C. F. Quate, "Microfabrication of cantilever styli for the atomic force microscope," *Journal of Vacuum Science and Technology A: Vacuum, Surfaces, and Films*, vol. 8, no. 4, pp. 3386–3396, 1990.
- [62] O. Wolter, T. Bayer, and J. Greschner, "Micromachined silicon sensors for scanning force microscopy," *Journal of Vacuum Science and Technology B: Microelectronics and Nanometer Structures*, vol. 9, no. 2, pp. 1353–1357, 1991.
- [63] R. Lthi, E. Meyer, H. Haefke, L. Howald, W. Gutmannsbauer, and H. Gntherodt, "Sled-type motion on the nanometer scale: Determination of dissipation and cohesive energies of c_{60} ," *Science*, vol. 266, no. 5193, pp. 1979–1981, 1994.
- [64] T. Junno, K. Deppert, L. Montelius, and L. Samuelson, *Controlled manipulation of nanoparticles with an atomic force microscope*. AIP, 1995, vol. 66.
- [65] C. Baur and et al., "Nanoparticle manipulation by mechanical pushing: underlying phenomena and real-time monitoring," *Nanotechnology*, vol. 9, no. 4, p. 360, 1998.
- [66] S. Brandow, W. Dressick, C. Dulcey, T. Koloski, L. Shirey, J. Schmidt, and J. Calvert, "Nanolithography by displacement of catalytic metal clusters using an atomic force microscope tip," *Journal of Vacuum Science and Technology B: Microelectronics and Nanometer Structures*, vol. 15, no. 5, pp. 1818–1824, 1997.
- [67] T. Junno, S. Anand, K. Deppert, L. Montelius, and L. Samuelson, *Contact mode atomic force microscopy imaging of nanometer sized particles*. AIP, 1995, vol. 66.
- [68] D. Yang and E. Sacher, "Local surface cleaning and cluster assembly using contact mode atomic force microscopy," *Applied Surface Science*, vol. 210, no. 3–4, pp. 158–164, 2003.

- [69] Y. Kim and C. M. Lieber, "Machining oxide thin films with an atomic force microscope: Pattern and object formation on the nanometer scale," *Science*, vol. 257, no. 5068, pp. 375–377, 1992.
- [70] P. Sheehan and C. Lieber, "Nanotribology and nanofabrication of moo_3 structures by atomic force microscopy," *Science*, vol. 272, no. 5265, pp. 1158–1161, 1996.
- [71] C. Baur, B. Gazen, B. Koel, T. Ramachandran, A. Requicha, and L. Zini, "Robotic nanomanipulation with a scanning probe microscope in a networked computing environment," *Journal of Vacuum Science and Technology B*, vol. 15, no. 4, pp. 1577–1580, 1997.
- [72] G. Blackman, C. Mate, and M. Philpott, "Interaction forces of a sharp tungsten tip with molecular films on silicon surfaces," *Physical Review Letters*, vol. 65, no. 18, p. 2270, 1990.
- [73] H. Hansma, S. Gould, P. Hansma, H. Gaub, M. Longo, and J. Zasadzinski, "Imaging nanometer scale defects in langmuir-blodgett films with the atomic force microscope," *Langmuir*, vol. 7, no. 6, pp. 1051–1054, 1991.
- [74] J. Garnaes, T. Bjornholm, and J. Zasadzinski, "Nanoscale lithography on langmuir-blodgett films of behinic acid," *Journal of Vacuum Science and Technology B: Microelectronics and Nanometer Structures*, vol. 12, no. 3, pp. 1839–1842, 1994.
- [75] T. Sumomogi, T. Endo, K. Kuwahara, R. Kaneko, and T. Miyamoto, "Micro-machining of metal-surfaces by scanning probe microscope," *Journal of Vacuum Science and Technology B*, vol. 12, no. 3, pp. 1876–1880, 1994.
- [76] O. Leung and M. Goh, "Orientational ordering of polymers by atomic force microscope tip-surface interaction," *Science*, vol. 255, no. 5040, pp. 64–66, 1992.
- [77] Y. Kim, J. Huang, and C. Lieber, "Characterization of nanometer scale wear and oxidation of transition-metal dichalcogenide lubricants by atomic force microscopy," *Applied Physics Letters*, vol. 59, no. 26, pp. 3404–3406, 1991.
- [78] L. Sohn and R. Willett, *Fabrication of nanostructures using atomic force microscope based lithography*. AIP, 1995, vol. 67.
- [79] U. Kunze and B. Klehn, "Plowing on the sub-50 nm scale: Nanolithography using scanning force microscopy," *Advanced Materials*, vol. 11, no. 17, pp. 1473–1475, 1999.
- [80] A. Notargiacomo and et al., "Atomic force microscopy lithography as a nanodevice development technique *," *Nanotechnology*, vol. 10, no. 4, p. 458, 1999.

- [81] S. Hu, A. Hamidi, S. Altmeyer, T. Koster, B. Spangenberg, and H. Kurz, "Fabrication of silicon and metal nanowires and dots using mechanical atomic force lithography," *Journal of Vacuum Science and Technology B*, vol. 16, no. 5, pp. 2822–2824, 1998.
- [82] B. Klehn, S. Skaberna, and U. Kunze, "Wet chemical nanoscale patterning of gaas surfaces using atomic force microscope lithography," *Superlattices and Microstructures*, vol. 25, no. 1-2, pp. 473–476, 1999.
- [83] B. Klehn and U. Kunze, "Nanolithography with an atomic force microscope by means of vector scan controlled dynamic plowing," *Journal of Applied Physics*, vol. 85, no. 7, pp. 3897–3903, 1999.
- [84] R. Magno and B. Bennett, *Nanostructure patterns written in III-V semiconductors by an atomic force microscope*. AIP, 1997, vol. 70.
- [85] A. Avramescu, K. Uesugi, and I. Suemune, "Atomic force microscope nanolithography on sio₂/semiconductor surfaces," *Japanese Journal of Applied Physics Part 1-Regular Papers Short Notes and Review Papers*, vol. 36, no. 6B, pp. 4057–4060, 1997.
- [86] S. Xu and G. Liu, "Nanometer-scale fabrication by simultaneous nanoshaving and molecular self-assembly," *Langmuir*, vol. 13, no. 2, pp. 127–129, 1997.
- [87] N. Amro, S. Xu, and G. Liu, "Patterning surfaces using tip-directed displacement and self-assembly," *Langmuir*, vol. 16, no. 7, pp. 3006–3009, 2000.
- [88] P. Schwartz, "Meniscus force nanografting: nanoscopic patterning of dna," *Langmuir*, vol. 17, no. 19, pp. 5971–5977, 2001.
- [89] M. Liu, N. Amro, C. Chow, and G. Liu, "Production of nanostructures of dna on surfaces," *Nano Letters*, vol. 2, no. 8, pp. 863–867, 2002.
- [90] M. Case, G. McLendon, Y. Hu, T. Vanderlick, and G. Scoles, "Using nanografting to achieve directed assembly of de novo designed metalloproteins on gold," *Nano Letters*, vol. 3, no. 4, pp. 425–429, 2002.
- [91] K. Wadu-Mesthrige, S. Xu, N. Amro, and G. Liu, "Fabrication and imaging of nanometer-sized protein patterns," *Langmuir*, vol. 15, no. 25, pp. 8580–8583, 1999.
- [92] G. Y. Liu, S. Xu, and Y. L. Qian, "Nanofabrication of self-assembled monolayers using scanning probe lithography," *Accounts of Chemical Research*, vol. 33, no. 7, pp. 457–466, 2000.
- [93] J. Kenseth, J. Harnisch, V. Jones, and M. Porter, "Investigation of approaches for the fabrication of protein patterns by scanning probe lithography," *Langmuir*, vol. 17, no. 13, pp. 4105–4112, 2001.

- [94] D. Weinberger, S. Hong, C. Mirkin, B. Wessels, and T. Higgins, "Combinatorial generation and analysis of nanometer- and micrometer-scale silicon features via dip-pen nanolithography and wet chemical etching," *Advanced Materials*, vol. 12, no. 21, pp. 1600–1603, 2000.
- [95] H. Zhang, S. Chung, and C. Mirkin, "Fabrication of sub-50-nm solid-state nanostructures on the basis of dip-pen nanolithography," *Nano Letters*, vol. 3, no. 1, pp. 43–45, 2002.
- [96] H. Chen, N. Xi, and G. Li, "CAD-guided automated nanoassembly using atomic force microscopy-based nonrobotics," *Automation Science and Engineering, IEEE Transactions on*, vol. 3, no. 3, pp. 208–217, 2006.
- [97] M. S. Johannes, D. G. Cole, and R. L. Clark, "Three-dimensional design and replication of silicon oxide nanostructures using an atomic force microscope," *Nanotechnology*, vol. 18, no. 34, p. 345304, 2007.
- [98] M. Versen, B. Klehn, U. Kunze, D. Reuter, and A. D. Wieck, "Nanoscale devices fabricated by direct machining of GaAs with an atomic force microscope," *Ultramicroscopy*, vol. 82, no. 1-4, pp. 159–163, 2000.
- [99] C. R. Rothe and H. "A concept for automated nanoscale atomic force microscope (afm) measurements using a priori knowledge," *Measurement Science and Technology*, vol. 20, no. 8, p. 084026, 2009.
- [100] S. Cruchon-Dupeyrat, S. Porthun, and G. Y. Liu, "Nanofabrication using computer-assisted design and automated vector-scanning probe lithography," *Applied Surface Science*, vol. 175-176, pp. 636–642, 2001.
- [101] Q. A. Huang and N. K. S. Lee, "Analysis and design of polysilicon thermal flexure actuator," *Journal of Micromechanics and Microengineering*, vol. 9, no. 1, p. 64, 1999.
- [102] K. Ivanova, T. Ivanov, A. Badar, B. Volland, I. Rangelow, D. Andrijasevic, F. Smecz, S. Fischer, M. Spitzbart, W. Brenner, and I. Kostic, "Thermally driven microgripper as a tool for micro assembly," *Microelectronic Engineering*, vol. 83, no. 4-9, pp. 1393–1395, 2006.
- [103] P. Boggild, T. Hansen, C. Tanasa, and F. Grey, "Fabrication and actuation of customized nanotweezers with a 25 nm gap," *Nanotechnology*, vol. 12, no. 3, p. 331, 2001.
- [104] J. H. Comtois, M. A. Michalicek, and C. C. Barron, "Electrothermal actuators fabricated in four-level planarized surface micromachined polycrystalline silicon," *Sensors and Actuators A: Physical*, vol. 70, no. 1-2, pp. 23–31, 1998.

- [105] M. F. Zeman, E. Bordatchev, and G. Knopf, "Design, kinematic modeling and performance testing of an electro-thermally driven microgripper for micro-manipulation applications," *Journal of Micromechanics and Microengineering*, vol. 16, no. 8, p. 1540, 2006.
- [106] K. Holhave and O. Hansen, "Electro-thermally actuated microgrippers with integrated force-feedback," *Journal of Micromechanics and Microengineering*, vol. 15, no. 6, p. 1265, 2005.
- [107] W. Rubio, E. Silva, E. Bordatchev, and M. Zeman, "Topology optimized design, microfabrication and characterization of electro-thermally driven microgripper," *Journal of Intelligent Material Systems and Structures*, vol. 20, no. 6, pp. 669–681, 2009.
- [108] B. Solano, S. Rolt, and D. Wood, "Thermal and mechanical analysis of an su8 polymeric actuator using infrared thermography," *Proceedings of the Institution of Mechanical Engineers – Part C – Journal of Mechanical Engineering Science*, vol. 222, no. 1, pp. 73–86, 2008.
- [109] M. Lu, Z. Wu, C. Huang, S. Hung, M. Chen, and Y. King, "Cmos micromachined grippers with on-chip optical detection," *Journal of Micromechanics and Microengineering*, vol. 17, no. 3, p. 482, 2007.
- [110] N. Chronis and L. Lee, "Electrothermally activated su-8 microgripper for single cell manipulation in solution," *Microelectromechanical Systems, Journal of*, vol. 14, no. 4, pp. 857–863, 2005.
- [111] G. Lau, J. Goosen, F. Keulen, T. Duc, and P. Sarro, "Polymeric thermal microactuator with embedded silicon skeleton: Part i; design and analysis," *Microelectromechanical Systems, Journal of*, vol. 17, no. 4, pp. 809–822, 2008.
- [112] G. Fedder and R. Howe, "Thermal assembly of polysilicon microstructures," in *Micro Electro Mechanical Systems, 1991, MEMS '91, Proceedings. An Investigation of Micro Structures, Sensors, Actuators, Machines and Robots. IEEE*, 1991, pp. 63–68.
- [113] L. Lin and M. Chiao, "Electrothermal responses of lineshape microstructures," *Sensors and Actuators a-Physical*, vol. 55, no. 1, pp. 35–41, 1996.
- [114] W. Fulkerson, J. P. Moore, R. K. Williams, R. S. Graves, and D. L. McElroy, "Thermal conductivity, electrical resistivity, and seebeck coefficient of silicon from 100 to 1300k," *Physical Review*, vol. 167, no. 3, p. 765, 1968.
- [115] F. Incropera, D. Dewitt, T. Bergman, and A. Lavine, *Fundamentals of Heat and Mass Transfer*, 6th ed. John Wiley and Sons, 2007.
- [116] J. M. Gere, *Mechanics of Materials, Sixth Edition*. Thomson Brooks/Cole, 2004.

- [117] D. J. Gorman, *Free Vibration Analysis of Beams and Shafts*. New York: John Wiley and Sons, 1975.
- [118] J. W. Judy, “Microelectromechanical systems (mems): fabrication, design and applications,” *Smart Materials and Structures*, vol. 10, no. 6, pp. 1115–1134, 2001.

Appendix A

MATLAB ETM Model Code

1 of 2

```

% Multifunctional Probe ETM Model
% Robert Riddle
%-----
close all
clear all
syms mh L mc lamda g Ts TH TC zero c1 c2 c3 c4
[c1,c2,c3,c4] = solve(c1+c2+TH-Ts,c3*exp(mc*(2*L))+c4*exp(mc*(2*L))+TC-Ts,-c1*exp(mh*L)-
c2*exp(-mh*L)+c3*exp(mc*L)+c4*exp(-mc*L)-TH+TC,c1*exp(mh*L)-c2*exp(-mh*L)-c3*lamda*exp
(mc*L)+c4*lamda*exp(-mc*L),c1,c2,c3,c4)
h=1101.7;
t=5e-6;
wc=23e-6;
wh=10e-6;
I=5.5e-3;
Jc=(I)/(wc*t);
Jh=(I)/(wh*t);
rho_0=3.2e-5;
xi=0.0019;
k_p=30;
Ts=27;
mc=sqrt((h-((Jc^2)*rho_0*xi*t))/(k_p*t))
mh=sqrt((h-((Jh^2)*rho_0*xi*t))/(k_p*t))
lamda=(wc*mc)/(wh*mh)
ah_2=(h-Jh^2*rho_0*xi*t)/(k_p*t)
ah_1=sqrt(ah_2)
ac_2=(h-Jc^2*rho_0*xi*t)/(k_p*t)
ac_1=sqrt(ac_2)
TH=Ts+((Jh^2*rho_0)/(k_p*ah_2))
TC=Ts+((Jc^2*rho_0)/(k_p*ac_2))
L=320e-6;
g=10e-6;
c1 = -(2*TC*lamda - 2*Ts*lamda - TC*lamda*exp(L*mc) - TC*lamda*exp(3*L*mc) +
TH*lamda*exp(L*mc) + TH*lamda*exp(3*L*mc) + (TH*exp(L*mc))/exp(L*mh) - (TH*exp(3*L*mc))/
/exp(L*mh) - (Ts*exp(L*mc))/exp(L*mh) + (Ts*exp(3*L*mc))/exp(L*mh) - (TH*lamda*exp
(L*mc))/exp(L*mh) - (TH*lamda*exp(3*L*mc))/exp(L*mh) + (Ts*lamda*exp(L*mc))/exp(L*mh) +
(Ts*lamda*exp(3*L*mc))/exp(L*mh))/ (exp(L*mc)*exp(L*mh) + exp(L*mc)/exp(L*mh) - exp
(3*L*mc)*exp(L*mh) - exp(3*L*mc)/exp(L*mh) + lamda*exp(L*mc)*exp(L*mh) - (lamda*exp
(L*mc))/exp(L*mh) + lamda*exp(3*L*mc)*exp(L*mh) - (lamda*exp(3*L*mc))/exp(L*mh))

```

```

c2=(2*TC*lamda - 2*Ts*lamda - TC*lamda*exp(L*mc) - TC*lamda*exp(3*L*mc) + TH*lamda*exp(L*mc) + TH*lamda*exp(3*L*mc) - TH*exp(L*mc)*exp(L*mh) + TH*exp(3*L*mc)*exp(L*mh) + Ts*exp(L*mc)*exp(L*mh) - Ts*exp(3*L*mc)*exp(L*mh) - TH*lamda*exp(L*mc)*exp(L*mh) - TH*lamda*exp(3*L*mc)*exp(L*mh) + Ts*lamda*exp(L*mc)*exp(L*mh) + Ts*lamda*exp(3*L*mc)*exp(L*mh))/ (exp(L*mc)*exp(L*mh) + exp(L*mc)/exp(L*mh) - exp(3*L*mc)*exp(L*mh) - exp(3*L*mc)/exp(L*mh) + lamda*exp(L*mc)*exp(L*mh) - (lamda*exp(3*L*mc))/exp(L*mh) + lamda*exp(3*L*mc)*exp(L*mh) - (lamda*exp(3*L*mc))/exp(L*mh))
c3=(2*TH*exp(2*L*mc) - 2*Ts*exp(2*L*mc) - (TC*exp(L*mh))/exp(L*mc) - TC/(exp(L*mc)*exp(L*mh)) + TC*exp(2*L*mc)*exp(L*mh) + (TC*exp(2*L*mc))/exp(L*mh) - TH*exp(2*L*mc)*exp(L*mh) - (TH*exp(2*L*mc))/exp(L*mh) + (Ts*exp(L*mh))/exp(L*mc) + Ts/(exp(L*mc)*exp(L*mh)) - (TC*lamda*exp(L*mh))/exp(L*mc) + (TC*lamda)/(exp(L*mc)*exp(L*mh)) + (Ts*lamda*exp(L*mh))/exp(L*mc) - (Ts*lamda)/(exp(L*mc)*exp(L*mh)))/(exp(L*mc)*exp(L*mh) + exp(L*mc)/exp(L*mh) - exp(3*L*mc)*exp(L*mh) - exp(3*L*mc)/exp(L*mh) + lamda*exp(L*mc)*exp(L*mh) - (lamda*exp(3*L*mc))/exp(L*mh) + lamda*exp(3*L*mc)*exp(L*mh) - (lamda*exp(3*L*mc))/exp(L*mh))
c4 = -(2*TH*exp(2*L*mc) - 2*Ts*exp(2*L*mc) - TC*exp(L*mc)*exp(L*mh) - (TC*exp(L*mc))/exp(L*mh) + TC*exp(2*L*mc)*exp(L*mh) + (TC*exp(2*L*mc))/exp(L*mh) - TH*exp(2*L*mc)*exp(L*mh) - (TH*exp(2*L*mc))/exp(L*mh) + Ts*exp(L*mc)*exp(L*mh) + (Ts*exp(L*mc))/exp(L*mh) + TC*lamda*exp(L*mc)*exp(L*mh) - (TC*lamda*exp(L*mc))/exp(L*mh) - Ts*lamda*exp(L*mc)*exp(L*mh) + (Ts*lamda*exp(L*mc))/exp(L*mh))/(exp(L*mc)*exp(L*mh) + exp(L*mc)/exp(L*mh) - exp(3*L*mc)*exp(L*mh) - exp(3*L*mc)/exp(L*mh) + lamda*exp(L*mc)*exp(L*mh) - (lamda*exp(3*L*mc))/exp(L*mh) + lamda*exp(3*L*mc)*exp(L*mh) - (lamda*exp(3*L*mc))/exp(L*mh))
xh=0:1e-6:320e-6;
xc=320e-6:1e-6:640e-6;
Th=TH+c1.*exp(mh.*xh)+c2.*exp(-mh.*xh);
Tc=TC+c3.*exp(mc.*xc)+c4.*exp(-mc.*xc);
figure(1);
plot(Th);
figure(2);
plot(Tc);
i=1;
T1=Th(321);
T2=Ts;
for x=320e-6:1e-6:640e-6
    T(i)=((T2-T1)*(x-320e-6))/(640e-6-320e-6)+T1;
    i=i+1;
end
figure(3)
plot(T)
TempMG_x=0:1:640;
TempMG_y=[Th T(2:321)];
figure(4)
plot(TempMG_x,TempMG_y)
axis([-10 650 0 550])
xlabel('Location on probe (\num)');
ylabel('Temperature (^o C)');
alpha=2.7e-6;
Th_mean=mean(Th)
T_mean=mean(T)
Th_disp=alpha*320e-6*(Th_mean-Ts)
T_disp=alpha*320e-6*(T_mean-Ts)
Delta_disp=Th_disp-T_disp
theta_disp=asind(Delta_disp/10e-6)
x_disp=80e-6*sind(theta_disp)
for i=1:321
    T_rev(i)=T(322-i);
end
Disp_sum(1)=0;
for i=2:322
    Disp(i)=alpha*(i-1)*10^(-6)*(Th(i-1)-T_rev(i-1));
    Disp_sum(i)=Disp(i)+Disp_sum(i-1);
end
for i=1:321
    Disp_sum2(i)=Disp_sum(i+1)/320;
end
h=1e-6:1e-6:80e-6;
x=sind(0.42)*h;
X=x+Disp_sum2(321);
Disp_total=[Disp_sum2 X];

figure(5)
plot(Disp_sum)
figure(6)
plot(Disp_sum2./1e-6)
xlabel('Location along probe (um)');
ylabel('Lateral displacement (um)')

figure(7)
plot(Disp_total./1e-6)
xlabel('Location along probe (um)');
ylabel('Lateral displacement (um)')

```

Appendix B

Microcontroller Code

```
#include <avr/io.h>
#include <avr/interrupt.h>
#include <stdint.h>
#include "clksys_driver.c"
#include <math.h>
float x0,x2p,x2i,x3p,x3i,x4,x5,xx,One=1,Zero=0,P=0.01,I=0.001;
signed int x1,y;
unsigned int x6,x7;

int main( void )
{
    sei();
    CLKSYS_Enable( OSC_RC32MEN_bm );
    CLKSYS_Prescalers_Config( CLK_PSADIV_1_gc, CLK_PSBODIV_1_1_gc );
    do {} while ( CLKSYS_IsReady( OSC_RC32MRDY_bm ) == 0 );
    CLKSYS_PLL_Config( OSC_PLLSRC_RC32M_gc, 22 );
    CLKSYS_Enable( OSC_PLEN_bm );
    CLKSYS_Prescalers_Config( CLK_PSADIV_4_gc, CLK_PSBODIV_1_1_gc );
    do {} while ( CLKSYS_IsReady( OSC_PLLRDY_bm ) == 0 );
    CLKSYS_Main_ClockSource_Select( CLK_SCLKSEL_PLL_gc );
    CLKSYS_Disable( OSC_XOSCEN_bm );
    ADCA_CTRLA=0b00000001;
    ADCA_CTRLB=0b00010000;
    ADCA_REFCTRL=0b00110000;
    DACB_CTRLA=0b00000101;
    DACB_CTRLB=0b00000000;
    DACB_CTRLC=0b00011000;
    PORTA.DIR=0b00000000;
    PORTB.DIR=0b11111110;
    PORTC.DIR=0b11111111;
    PORTE.DIR=0b00000000;
    TCC0.PER = 1;
    TCC0.CTRLA = 0x01;
    TCC0.INTCTRLA = 0x03;
    PMIC.CTRL = 0x04;
    PMIC.STATUS=0x04;
    while(1) {
        }
    }
}
```

```
ISR(TCC0_OVF_vect, ISR_NOBLOCK)
{
    PORTC.OUT=0b00000001;
    if (PORTE.IN==0b11111111)
    {
        ADCA_CH0_CTRL=0b10000001;
        y=ADCA_CHORES;
        x1=1000-y;
        x2i= fma    (    (float)x1,
                       One,
                       x0
                    );
        x3p= fma    (    (float)x1,
                       P,
                       Zero
                    );
        x3i= fma    (    x2i,
                       I,
                       Zero
                    );

        x4= fma    (    x3p,
                       One,
                       x3i
                    );
        x5= fma    (    xx,
                       One,
                       x4
                    );

        if (x5<0){
            x6=0;
        }
        else{
            x6=(unsigned int)x5;
        }
        if (x6>4095){
            x7=4095;
        }
        else{
            x7=x6;
        }

        DACE_CHODATA=(unsigned int)x7;
        x0=x2i;
        xx=(float)x7;
    }
    else
    {
        DACE_CHODATA=0x4C9;
        xx=0x4C9;
        x0=0;
    }
    PORTC.OUT=0b00000000;
}
```